

NASA
Technical
Paper
2180

September 1983

NASA
TP
2180
c.1

TECH LIBRARY KAFB, NM

0068064



Free-Stream Noise and Transition Measurements a Cone in a Mach 3.5 Pi. Low-Disturbance Tunnel

Ivan E. Beckwith,
Theodore R. Creel, Jr.,
Fang-Jenq Chen, and
James M. Kendall

LOAN COPY: RETURN TO
AFWL TECHNICAL LIBRARY
KIRTLAND AFB, N.M. 87117

NASA

25
25th Anniversary
1958-1983

NASA
Technical
Paper
2180

1983

TECH LIBRARY KAFB, NM



0068064

Free-Stream Noise and Transition Measurements on a Cone in a Mach 3.5 Pilot Low-Disturbance Tunnel

Ivan E. Beckwith and
Theodore R. Creel, Jr.
Langley Research Center
Hampton, Virginia

Fang-Jenq Chen
Systems and Applied Sciences Corporation
Hampton, Virginia

James M. Kendall
Jet Propulsion Laboratory
Pasadena, California

NASA
National Aeronautics
and Space Administration

Scientific and Technical
Information Branch

SUMMARY

Boundary-layer transition Reynolds numbers obtained in supersonic wind tunnels are generally lower than those of free flight because the tunnel test environment contains noise radiated from the tunnel-wall turbulent boundary layers. This radiated noise generates disturbances within the test-model boundary layers which are then amplified by instability to a stage of nonlinearity and thence to turbulence.

In the present work a 10×6 in. Mach 3.5 two-dimensional nozzle which differs in design substantially from more conventional ones has been tested in order to demonstrate a reduction in the free-stream disturbance levels and to observe the subsequent effects upon transition on a slender cone. Three notable features of the nozzle design are: first, the use of a rapid-expansion contour wherein the pressure (noise) waves present in the test flow originate far upstream on the nozzle wall where the local Mach number is low and where noise production is inefficient; second, the selection of a wide separation of the two planar sidewalls in order that noise from these cannot reach the test model until far downstream; and third, the provision of boundary-layer bleed slots shortly upstream of the nozzle throat for removal of the turbulent boundary layer on the contraction walls.

For unit Reynolds numbers between 2.5×10^5 and 15×10^5 per inch, the observed root-mean-square values of fluctuating static pressures were found to vary from extremely low values of less than 0.03 percent up to about 0.8 percent of the mean static pressure, depending upon the unit Reynolds number, the axial location in the test rhombus, and the bleed slot flow. The low noise levels corresponded to laminar boundary layers on the nozzle walls, whereas the higher noise levels were caused by eddy Mach wave radiation from transitional or turbulent wall boundary layers.

When the boundary-layer bleed valve was open, the wall boundary layers over upstream regions of the nozzle were laminar at the lower unit Reynolds numbers, and the absence of high-frequency radiated noise then resulted in cone transition Reynolds numbers approaching those reported for free flight. As the unit Reynolds numbers were increased or when the bleed valve was closed, the nozzle-wall boundary layers became transitional and turbulent. The noise then increased to much higher levels, with significant energy up to 150 kHz. The cone transition Reynolds numbers then decreased considerably to values comparable to those measured in conventional wind tunnels.

INTRODUCTION

To advance transition research at supersonic speeds and simulate the low-disturbance environment of high-altitude flight a new type of wind tunnel is required that will eliminate or reduce high intensity noise radiated into the test section from turbulent boundary layers on nozzle walls (refs. 1 to 5). In well-designed conventional wind tunnels the wall boundary layers can be maintained laminar but only at such low Reynolds numbers that transition is not obtained on simple models (ref. 6). Various techniques for maintaining laminar boundary layers on nozzle walls at high Reynolds numbers have been investigated at the Langley Research Center (refs. 7 to 10). These techniques were developed with axisymmetric Mach 5 nozzles and included the use of rapid-expansion contours, highly polished walls, heated walls,

and a boundary-layer bleed slot upstream of the throat. However, recent results (ref. 11) indicated that maximum values of test Reynolds numbers with laminar wall boundary layers in an axisymmetric Mach 5 nozzle which utilized these techniques are not significantly higher than in good conventional nozzles.

A new technique for obtaining large reductions in noise at higher Reynolds numbers where the nozzle-wall boundary layers are turbulent has been developed at the Langley Research Center. (See refs. 12 and 13.) It was shown that by the use of a very short, rapid-expansion nozzle, the Mach number and turbulent boundary-layer thickness at the upstream acoustic origins could be reduced and the radiated noise was thereby diminished by nearly an order of magnitude. These tests were conducted in an axisymmetric Mach 5 nozzle where the quiet test core was too small to be useful. Calculations (ref. 13) for both axisymmetric and two-dimensional nozzles indicated that larger test cores could be obtained at lower Mach numbers. Also, the data of Anders et al. (refs. 12 and 13) showed that the rapid-expansion axisymmetric nozzle was subject to severe centerline nonuniformities in both mean flow and noise because of focusing from axisymmetric machining errors. These aforementioned results led to the present Mach 3.5 two-dimensional nozzle design which utilizes the concepts of both the rapid-expansion contour and a large width-to-height ratio to reduce the intensity of noise radiated into the test region at high Reynolds numbers. Also, boundary-layer removal slots located in the subsonic contraction region of the nozzle are provided to aid in maintaining laminar wall boundary layers over a portion of the supersonic expansion at lower Reynolds numbers.

Preliminary noise data obtained in this nozzle with fluctuating pitot pressure probes have been reported in reference 14. The purposes of the present report are to present new and more extensive root-mean-square noise data, source velocities, and spectral data obtained in this nozzle using hot-wire probes and also to present transition Reynolds numbers on a 5° half-angle sharp tip cone at zero angle of attack as determined from measured equilibrium wall temperatures. A preliminary assessment of the relation between transition Reynolds numbers and noise levels and spectra is also presented.

Use of tradenames or names of manufacturers in this report does not constitute an official endorsement of such products or manufacturers, either expressed or implied, by the National Aeronautics and Space Administration.

SYMBOLS

\tilde{C}_p	fluctuating static pressure coefficient, $\tilde{p}_\infty/\bar{q}_\infty$
D	effective nozzle exit diameter, $2\left[\frac{1}{\pi}(\text{Exit area})\right]^{1/2}$
E	fluctuation energy
e	voltage
F	dimensionless frequency, $2\pi fv/u_\infty^2$
f	frequency
M	Mach number

N exponential factor in amplification ratio e^N from linear stability theory
 Pr Prandtl number
 p static pressure
 q dynamic pressure, $\frac{1}{2} \rho u^2$
 R unit Reynolds number, $\rho u / \mu$
 R_D free-stream Reynolds number based on D (see fig. 11)
 $R_{e,T}$ local transition Reynolds number based on flow distance to transition
 r recovery factor defined by equation (2)
 rms root mean square
 T absolute temperature
 u streamwise velocity
 x axial distance from nozzle throat or from cone apex
 x_c axial distance of cone apex from nozzle throat
 Y vertical distance from nozzle centerline
 Z horizontal distance from nozzle centerline
 $\Delta X, \Delta Y, \Delta Z$ axial, vertical, and horizontal dimensions of quiet test core
 (see fig. 22)
 α angle of attack
 β Mach angle
 θ_c cone half-angle
 μ dynamic viscosity
 ν kinematic viscosity, μ/ρ
 ρ mass density
 ϕ roll angle with respect to vertical of cone thermocouple row as viewed from cone base

Subscripts:

aw adiabatic wall
 e local values at boundary-layer edge
 o stagnation

ref mode plot reference value
s noise source
sw sidewall (see fig. 22)
T transition onset
TE transition end
t pitot
w wall
 ∞ free stream

Superscripts:

\sim root mean square
 $-$ mean value

APPARATUS

Facility

The supersonic pilot low-disturbance tunnel is located in the Gas Dynamics Laboratory at the Langley Research Center. High-pressure air from the 4200-psi tank field is dried to a dew-point temperature of -52°F and is then reduced in pressure by control valves located some distance upstream of the settling chamber. The supply air then passes through a filter that is rated to remove 99 percent of all particles larger than 1 μm in size.

The settling chamber is approximately 21 ft long by 2 ft inside diameter; it contains seven turbulence screens plus several dense porous plates which function as acoustic baffles that attenuate the high level noise from control valves and the piping system from about 0.2 percent of stagnation pressure down to about 0.01 percent (refs. 15 and 16). The screens reduce the normalized rms velocity fluctuations to about 1 percent, as measured outside the wall boundary layer in the settling chamber.

Figure 1 shows the settling chamber, visible on the right side of the figure, and the open jet test-section chamber on the left. The large circular manifold is connected to a 41-ft diameter vacuum sphere which is used to remove the boundary-layer bleed air from the nozzle through 16 1-in-diameter pipes and hoses, some of which can be seen in the center region of figure 1. The nozzle exit is approximately 6 in. high by 10 in. wide and is visible in the upstream end of the test-section chamber, to the left of center in the figure. The tunnel flow exhausts to a 60-ft-diameter sphere which, with the current operating procedures and a fixed-area diffuser, provides about a 7-min run for a stagnation pressure of 75 psia.

Nozzle

A cutaway isometric sketch of the nozzle is shown in figure 2(a). Dimensions of the throat and exit and the length of the nozzle are given in the figure. The inflection point on the rapid-expansion nozzle contour wall is only 0.5 in. downstream of the throat where the maximum wall angle is 28.75° , which is much larger than in conventional Mach 3.5 wind-tunnel nozzles. Isometric sectional views of the boundary-layer bleed slots located upstream of the throat on both the contour wall and sidewall are shown. The boundary-layer bleed or suction plenum is also shown with a portion of 1 of the 16 exhaust pipes indicated. Figure 2(b) is a photograph of the subsonic approach which provides a smooth transition from the circular cross section of the settling chamber to the boundary-layer removal slots and the rectangular throat. An important part of the nozzle design procedure was the performance of a detailed calculation for the flow in the transonic region of the nozzle, including that in the contour wall slots, by a time-split difference scheme programmed by Strikwerda (ref. 17). This numerical solution provided accurate initial conditions for the method of characteristics used to compute the flow and wall streamline in the supersonic part of the nozzle. A correction for the boundary-layer displacement thickness was applied to the inviscid wall streamline.

The boundary-layer bleed flow could be cut off by closing a valve downstream of the bleed manifold. Thus, with this bleed valve closed, the boundary layer in the subsonic approach spilled around the slot leading edges. With this bleed valve open, the entire boundary layers on both the contour walls and sidewalls of the subsonic approach were removed. The bleed mass flow was maintained constant at a given value of p_o by maintaining the suction plenum pressure at less than one-half the value of p_o . This low plenum pressure resulted in sonic flow (except in the very thin subsonic part of the boundary layer) in the minimum area section of the slot channels. This sonic flow minimized the transmission into the nozzle of any acoustic disturbances in the plenum.

The reasons for the generally lower noise levels that have been measured in this nozzle (ref. 14) can best be discussed with reference to figure 3, which shows a scale sketch of the contour wall and sidewall with Mach lines from typical wall noise sources shown in the vertical and horizontal center planes. Corresponding values of local inviscid wall Mach numbers M_w are given on the figure. The sketch depicts the vertical and horizontal half sections of the nozzle folded about the centerline into the same plane. It has been shown (refs. 12 and 13) that if M_w in a rapid-expansion nozzle is approximately 2.8 or less, then the noise levels in the upstream region of the test rhombus are reduced to about 0.2 percent even if the nozzle-wall boundary layers are fully turbulent. Because noise is propagated along Mach lines in supersonic flow, this finding indicates that the quiet-test-core region shown in figure 3 should experience low levels of radiated noise from the contour walls and very little, if any, radiated noise from the sidewalls because the values of M_w are less than 2.8 at the pertinent source locations. In fact, noise radiation from the sidewalls into the center region of the test rhombus should not be significant to $X = 17$ or 18 in. because of the large width-to-height ratio of the nozzle. These low noise expectations were fully realized as shown previously (ref. 14).

Cone Model

The 5° half-angle cone, fabricated of stainless steel, was 15 in. long. It consisted of a 1-in-long replaceable tip (with a nose radius of 0.0025 in.) and a 0.030-in-thick skin extending from the cone tip to the 0.3-in-thick base plate. Two

rows of thermocouples were attached to the skin on opposite sides of the cone, with 53 thermocouples in each row spaced 0.25 in. apart in the axial direction beginning at 1.45 in. from the apex. The thermocouple wires were 0.010 in. in diameter and were soft-soldered into 0.025-in-diameter holes drilled through the skin. The surface finish of the cone was estimated to be 10 to 20 rms μ in.

TESTS AND INSTRUMENTATION

The hot-wire data to be presented were obtained over a range of stagnation pressures from about 25 to 150 psia at stagnation temperatures from about 60°F to 85°F. The cone-transition data were obtained over the same range of pressures but at somewhat higher temperatures of 105°F to 165°F. The corresponding range of free-stream unit Reynolds number extended from approximately 2.5×10^5 per inch to 1.5×10^6 per inch.

The hot-wire data were taken with constant-current anemometers, automatic overheat switching circuits, and a Flow Corporation model 1900-3 compensating amplifier. The hot-wire probes were strung with 0.1-mil-diameter tungsten wire which was welded to needles spaced to provide a length-to-diameter ratio of 200. Most of the data used in this report were obtained with a Flow Corporation model 1900-1 anemometer and an automatic heating circuit developed by Anders. (See ref. 9.) To provide an independent check of these results, many runs were repeated with a new automated anemometer and heating circuit (model KST-100, developed by Kendall, one of the four authors of the present report) which prevents overload currents in the wire during rapid mean flow changes such as flow start-up or break-down conditions. The usual test procedure at each pressure consisted of first obtaining one mode diagram at a reference location in the nozzle by standard techniques (refs. 18 and 19) wherein the hot-wire data were recorded for several overheats at nominally constant tunnel conditions. In unheated supersonic tunnels for $M > 2.5$, most experiments have shown the dominant free-stream disturbance mode to be the acoustic pressure fluctuations caused by eddy Mach wave radiation from the nozzle-wall turbulent boundary layers. For these conditions the mode diagram is linear, and both the rms pressure fluctuation level and mean source velocity are obtained directly from an analysis of the mode diagram (ref. 1). Then, for the same tunnel conditions and during the same run, the axial distributions of \tilde{e}_m , the hot-wire rms voltage intensities at the highest overheat, were obtained as the hot-wire probe was moved with a survey mechanism. Because the mode diagram also showed that for a constant value of M_∞ , $\tilde{p}_\infty/\bar{p}_\infty$ was nearly proportional to \tilde{e}_m , the local normalized rms pressures were computed from the relation

$$\frac{\tilde{p}_\infty}{\bar{p}_\infty} = \frac{\tilde{e}_m}{\tilde{e}_{m,ref}} \left(\frac{\tilde{p}_\infty}{\bar{p}_\infty} \right)_{ref} \left(\frac{p_0}{p_{0,ref}} \right)^{-n} \quad (1)$$

where $\tilde{e}_{m,ref}$ is the rms voltage intensity at the highest overheat from the mode diagram data at the reference location. (These rms values have been corrected for instrument noise by subtracting the square of the noise from the square of the total signal.) The value of n in equation (1) was taken as 1/4, based on typical trends in the present mode plot data near the nozzle exit when the boundary layers on the

nozzle walls at the upstream acoustic origins were turbulent. When the acoustic origin boundary layers were laminar, the hot-wire signal was usually obscured by the instrument noise so that consistent trends with p_o could not be determined. Nevertheless, because the value of p_o was maintained constant to within 10 percent or better during any axial survey, the value $n = 1/4$ has been applied to all data as a first-order correction for small changes in stagnation pressure that occurred while data for the reference mode diagram and corresponding survey were being recorded.

RESULTS AND DISCUSSION

Comparison of Root-Mean-Square Pitot Pressure and Hot-Wire Data

Figure 4 compares typical variations of \tilde{p}_t/\bar{p}_t as measured previously using pitot pressure probes (ref. 14) with values of $\tilde{p}_\infty/\bar{p}_\infty$ from the present hot-wire data for the three lowest values of unit Reynolds number and with bleed valve open and closed. The trends shown by the two sets of data are in good agreement, but there are differences in the values ranging from a few percent to considerably more for some of the low level data. These differences may be accounted for in part by the different quantities measured. An estimate of this difference may be obtained from an equation given in reference 18 relating $\tilde{p}_\infty/\bar{p}_\infty$ to \tilde{p}_t/\bar{p}_t . For $M_\infty = 3.5$, this equation gives

$$\frac{\tilde{p}_\infty}{\bar{p}_\infty} \approx 1.08 \frac{\tilde{p}_t}{\bar{p}_t}$$

where $u_s/\bar{u}_\infty = 0.45$ was used, corresponding to turbulent boundary layers on the nozzle wall. Thus, the hot-wire data are usually higher than the pitot data for fully turbulent wall boundary layers as observed, for example, in figure 4(a) with bleed valve closed and $X > 11$ in. and in figure 4(c) with bleed valve open and $X > 10$ in.

The rms pitot data for turbulent wall boundary layers might be expected to be lower than the hot-wire data for another reason. This is due to the poor high-frequency response of the pitot probes because of their much larger size than the wires. Thus, acoustic disturbances with energy above frequencies of 40 to 50 kHz cannot be resolved by the larger pitot probes, and that portion of the signal is not sensed by the pitot pressure transducer. On the other hand, the fully turbulent data in figure 4(b) (bleed valve closed, $X > 11.5$ in.) show fair agreement between the pitot and hot-wire data. However, the inherent accuracy of the two methods and other uncontrolled variables such as nozzle-wall deposits and the location of transition also affect the data such that consistent agreement cannot be expected.

When the nozzle-wall boundary layers are laminar, the values of \tilde{p}/\bar{p} are usually less than 0.05 percent as shown in figures 4(a) and 4(b) for bleed valve open and $X < 13$ in. and $X < 11$ in., respectively. Note that values of hot-wire data are about three times larger than values of the pitot data in these regions. For these conditions, the hot-wire signal was usually too close to the instrument noise to provide reliable results, whereas the pitot pressure transducers (ref. 14) pro-

vided better signal-to-noise ratios. Thus, for laminar wall boundary layers when there is no high-frequency noise, the rms pitot-probe data are believed to be more reliable than the hot-wire data.

The high level peaks in the pitot noise data which always occurred in the upstream regions of the test rhombus with the bleed valve closed at the two lowest values of $R_\infty \approx 2.5 \times 10^5$ and 5.1×10^5 per inch are verified by the present hot-wire data. These peaks are believed to be caused by transitional wall boundary-layer structures which apparently radiate higher intensity noise than the fully turbulent boundary layers farther downstream.

Comparisons between the mean pitot pressure data for bleed valve open and closed (shown as the small symbols in the upper part of fig. 4) indicate that the Mach numbers are generally lower when the bleed valve is closed. (The mean pitot pressure ratio and corresponding isentropic Mach number scales are located in the upper left parts of these figures.) This result shows that the boundary layers on the contour walls are thicker when the valve is closed. At $R_\infty \approx 8.0 \times 10^5$ per inch (fig. 4(c)), these thicker boundary layers are fully turbulent. Therefore, the noise levels are lower than with the bleed valve open in the region of 10 inches $< X < 14$ inches where transitional wall boundary-layer effects cause the higher noise levels.

Axial Surveys of Root-Mean-Square Static Pressures

Figures 5, 6, and 7 show typical hot-wire data for the normalized rms static pressure $\tilde{p}_\omega/\tilde{p}_\infty$ plotted against X for $Y = 0$ with $Z = 0$, $Z = -2$ in., and $Z = -4$ in., respectively, for bleed valve open and closed over the test range of unit Reynolds number from approximately 2.5×10^5 per inch to 16×10^5 per inch. Figures 8 and 9 show similar types of data in the vertical center plane ($Z = 0$) at $Y = -0.5$ in. and $Y = 1.5$ in., respectively, also over the test range of unit Reynolds number. The small data points in all these figures are taken directly from the mode plots; all of the other data points were obtained during the axial surveys with the use of equation (1).

To illustrate the dependence of cone transition on the physical noise distributions in the nozzle, the upper parts of figures 5(a) to 5(d) show a sketch of the nozzle contour and test rhombus outline with the cone superimposed in the two test positions used. Because the cone was always located on the nozzle centerline, only the cone and nozzle half sections above the centerline are shown in the sketches. The data points plotted on the cone surfaces represent the measured locations of transition on the cone at approximately the same unit Reynolds number as denoted by the corresponding symbol used for the noise data in the lower part of each figure. The dependence of transition on the noise field characteristics is apparent from these figures; however, further discussion of this dependence will be delayed until the detailed transition data are presented in a subsequent section of this paper.

Returning to the extensive set of noise data in figures 5 to 9, the following principal characteristics of the noise field are apparent:

- (1) With the bleed valve open and for any given value of R_∞ , the level of the noise varies by more than an order of magnitude at different locations within the test rhombus from low "laminar" values of less than 0.1 percent in the upstream regions on the centerline to higher "turbulent" values from about 0.3 to 0.8 percent in the downstream regions and off the centerline close to the sidewall ($Z = 4$ in.).

(2) For $R_\infty > 7.6 \times 10^5$ per inch, the noise levels are generally lower with the bleed valve closed than with the bleed valve open, particularly for $8 \text{ in.} < X < 15 \text{ in.}$. However, at the two lowest values of $R_\infty \approx 2.5 \times 10^5$ per inch and $R_\infty \approx 5 \times 10^5$ per inch, the opposite effect of the bleed valve is noted, and large peaks in noise occur with the valve closed at $X \approx 11 \text{ in.}$ and $X \approx 7 \text{ in.}$, respectively, across the entire horizontal center plane. These peaks are possibly caused by transitional flow on the contour walls as already noted in the discussion of figure 4.

(3) Changes in noise levels at various locations within the test rhombus for a given set of flow conditions can be traced upstream along Mach lines to the "acoustic origin" on the nozzle wall, as illustrated for a hypothetical quiet test core in figure 3. Thus, the approximate location of transition in the boundary layer on the contour walls can be determined for a given value of R_∞ . The corresponding Mach lines are the downstream boundaries of the laminar quiet test core at that value of R_∞ . In the same way, the downstream boundaries of the turbulent quiet test core can be determined in both the vertical and horizontal center planes of the nozzle from the regions along the contour walls or sidewalls, respectively, where the radiated noise begins to increase significantly.

The first two characteristics mentioned above can be verified by a cursory examination of the figures. The third characteristic requires further explanation which will be presented in the following paragraphs.

Consider first the propagation of noise in the vertical center plane from the transitional region of the boundary layers on the contour walls. The following table lists, for the bleed-valve-open (hot-wire) data, the centerline locations X (in inches) where the noise first increases from the low laminar levels to 0.1 percent and the corresponding locations X_w (in inches) of the acoustic origins on the contour wall:

Nominal R_∞^{-1} , in	$Y = 0$				$Y = -0.5 \text{ in.}$		$Y = 1.5 \text{ in.}$	
	Fig. 4		Fig. 5(a)		Fig. 8(a)		Fig. 9(a)	
	X	X_w	X	X_w	X	X_w	X	X_w
2.5×10^5	14.2	5.5	14.8	6.0	14.2	6.5	9.7	5.7
5.0	11.3	3.7	11.0	3.5	10.2	4.0		

For a given value of R_∞ , it is apparent that there is reasonable agreement in the values of X_w (underlined for emphasis) even when the corresponding X -locations from the off-centerline surveys are much different than the centerline values. For example, at $R_\infty \approx 2.5 \times 10^5$ per inch, the locations of transition by this criterion varied from only about 5.5 in. to 6.5 in. Because these data are taken from different runs made over a period of several months, the variations in X_w are believed to be caused by inadvertent variations in nozzle-wall deposits of dust and lint.

The propagation of noise from sidewall sources in the horizontal center plane is demonstrated in a similar manner by the data for $R_\infty \approx 2.5 \times 10^5$ per inch. For this value of R_∞ , values of X and X_w (in inches) are again listed in the following table:

Z , in.	Source figure	X	X_w
-4	7(a)	4.5	1.6
-2	6(a)	11.0	1.6

The increase in noise at these X -locations for the surveys at $Z = -4$ and -2 in. is caused by the increasing level of noise radiation from the sidewall turbulent boundary layer at $X_w \approx 1.6$ in. where the local Mach number is about 2.4. The Mach line from this wall point is slightly upstream of the one shown in figure 3 starting at the sidewall point for $M_w = 2.69$. The former line intersects the centerline ($Z = 0$) at $X \approx 18$ in. The data in figure 5(a) at this unit Reynolds number show an appreciable increase in noise level in the vicinity of $X = 18$ in. Hence, it may be concluded that this increase in centerline noise is caused by the increasing noise radiation from the two sidewalls as the acoustic origin Mach number along the wall increases to about 2.4. This increasing noise radiation from the sidewalls is also apparent for $R_\infty > 7.6 \times 10^5$ per inch with bleed valve closed in figures 5(d) and 6(d), starting at $X \approx 15$ to 16 in. The concept of using the wide nozzle to eliminate radiation from the sidewalls is therefore validated by these data.

The axial length of the laminar quiet test core with bleed valve open depends on the unit Reynolds number as shown by the data in figures 4 and 5. From figures 5(a) and 5(b) and by using $X = 5$ in. as the upstream tip of the test rhombus, the axial lengths ΔX along the centerline of the laminar test core are as follows:

Nominal R_∞^{-1} in	ΔX , in.
2.5×10^5	9.8
5.0	6.0
7.6	5.0
10.0	2.4

The length of a "turbulent quiet test core" ($\tilde{p}_\infty/\bar{p}_\infty < 0.2$ percent) with bleed valve closed for $R_\infty > 7.6 \times 10^5$ per inch is about 9.5 in. according to the data in figure 5(d).

One additional peculiarity of the noise data that should be noted is the gradual increase to a noticeable peak in noise levels that occurs with increasing values of X in the region of 8 in. $< X <$ 14 in. (for $Y = 0$) with bleed valve open for $R_\infty > 7.6 \times 10^5$ per inch. It was thought previously (ref. 14) that this peak might have been caused by shimmering Mach wave noise from waviness defects on the contour wall; however, it is now believed that the effect is caused primarily by transitional

boundary-layer flow along the contour walls between $X_w \approx 2$ in. and $X_w \approx 7$ in. Thus, in figures 5(b) and 6(b), the peak region seems to move upstream with increasing values of R_∞ . At the higher values of R_∞ , it appears that the development of this transitional flow is delayed or suppressed by the large axial pressure gradients along the contour walls. At $Y = -0.5$ in. (fig. 8(a)), the peak region is extended in the axial direction and the rise starts farther upstream because of the asymmetrical radiation from the top and bottom contour walls. Gortler vortices are probably involved in these transition processes (as in ref. 11); however, further investigation will be required to determine whether the vortices or their associated structures (ref. 20) contribute to the radiated noise.

Source Velocities

Figure 10 shows typical mode diagram data (basic methods and equations given in refs. 1 and 19) on the centerline at or near the nozzle exit for the variation with unit Reynolds number of the normalized source velocity u_s/\bar{u}_e and the normalized rms static pressure, $\tilde{p}_\infty/\bar{p}_\infty$ for bleed valve open and closed. Data from two different anemometers and heating circuits, identified by the notation "KST" and "FC" (model KST-100 and Flow Corporation model 1900-1, respectively), are shown in figure 10 to indicate the generally acceptable agreement that was obtained by use of the two systems. The source velocity varies from about 0.2 to 0.4 of the local free-stream velocity for bleed valve both open and closed and appears to decrease slightly with increasing values of R_∞ . The rather large scatter in these data is caused by instrument noise problems. Nevertheless, the agreement of the higher values with Laufer's data (in ref. 21, the measured value at $M = 3.5$ was $u_s/\bar{u}_\infty \approx 0.45$) indicates that the disturbances are due to eddy Mach wave radiation.

With bleed valve open (fig. 10(a)), the noise levels first increase to a peak due to the influence, even at this station of $X = 15.5$ in., of the laminar and transitional nozzle-wall boundary layers at the far upstream acoustic origins. For $R_\infty > 7.6 \times 10^5$ per inch, the decreasing trend of $\tilde{p}_\infty/\bar{p}_\infty$ with unit Reynolds number is typical of radiated noise from fully turbulent boundary layers. This decreasing trend is evident at $X = 13.5$ in. (fig. 10(b)) over the entire range of R_∞ with bleed valve closed.

Comparison of Noise Levels With Previous Data

Typical noise levels expressed as the rms pressure coefficient C_p^\sim for both laminar and turbulent signals from the present centerline data of figures 4, 5, and 10 are plotted in figure 11 against R_D , the free-stream Reynolds number based on the effective exit diameter of the nozzle. The pressure-coefficient parameter is used here for comparisons with other data because of its generally smaller variation with Mach number than $\tilde{p}_\infty/\bar{p}_\infty$. For comparison with these results, data from four different wind tunnels (refs. 21 to 23) obtained by both hot-wire and pitot pressure probes (solid and open symbols, respectively) are also plotted in figure 11. For the present data, the X-locations and type of signal (laminar or turbulent) are indicated in the figure. As mentioned previously, the present turbulent pitot-pressure data are lower than the corresponding hot-wire data because the pitot probes were too large to respond to the high-frequency portion of the signal for $f > 40$ to 50 kHz. This discrepancy between the two techniques appears to increase with increasing Reynolds number, as might be expected. All of the pitot-pressure data for the present nozzle have been reported previously (ref. 14) except for one additional point at

the highest value of R_D . The relatively large uncertainty in the present laminar hot-wire data is indicated by the vertical scatter bars for these data points.

The present laminar fluctuation amplitudes are between one and two orders of magnitude lower than data for $R_D > 10^6$ in conventional tunnels, which have turbulent wall boundary layers at these Reynolds numbers. Laminar wall boundary layers have been obtained in the Jet Propulsion Laboratory (JPL) 20-Inch Supersonic Wind Tunnel at generally lower Reynolds numbers as follows:

M_∞	Nominal R_D
2.4	3.7×10^5
3.7	4.6×10^5
4.5	1.1×10^6

Hot-wire measurements in the JPL tunnel for the above condition at $M_\infty = 4.5$ resulted in normalized values of the rms fluctuating mass flow and the total temperature of 0.037 percent and 0.001 percent, respectively. Because the mode diagram was a straight line, it may be assumed that the dominant disturbance mode was acoustic (presumably due to shimmering Mach waves from fixed sources such as wall roughness or waviness) and the resulting value of the fluctuating pressure coefficient C_p^\sim was 0.0036 percent. This value is plotted in figure 11 and is seen to be in good agreement with the present laminar data.

At $R_D \approx 10^7$, the levels of the present turbulent data are about 0.03 percent compared to levels ranging from 0.05 percent for the large AEDC/VKF Tunnel A (ref. 22) to 0.08 percent for the JPL 20-Inch Tunnel (ref. 21). (The trend of decreasing noise with increasing Reynolds number is apparent in most of the turbulent hot-wire data except AEDC/VKF Tunnel B (ref. 22) at $M_\infty = 6$.) The concept of the turbulent quiet test core (refs. 12 and 13) which depends primarily on the use of a very short rapid-expansion nozzle contour is therefore confirmed by the present data.

Power Spectra

It has been shown (refs. 6, 24, and 25) that the spectra of free-stream disturbances may have significant effects on transition when test conditions favor amplification of Tollmien-Schlichting (TS) waves at critical frequencies that are present in the external disturbances. These conditions are exemplified by two-dimensional boundary layers on smooth surfaces and by the boundary layer on the present sharp apex cone at zero angle of attack. The most amplified TS frequencies that, according to linear stability theory, would be present in the laminar boundary layer preceding transition have been calculated by Malik¹ for the present test conditions ($\theta_c = 5^\circ$;

¹Malik, M. R.: Instability and Transition in Supersonic Boundary Layers. To be presented at the ASME Symposium on Turbulent and Laminar Boundary Layers - Their Control and Flow Over Compliant and Other Surfaces (New Orleans, La.), Feb. 1984.

$M_\infty = 3.50$; $M_e = 3.36$; $T_w = T_{aw}$). These frequencies are approximately 55 kHz and 75 kHz for $R_{e,T} = 6.8 \times 10^6$ and 8.2×10^6 at $R_e = 5 \times 10^5$ and 7.6×10^5 per inch, respectively.

Transition data from the present tests (presented in the next section of this report) show that for $R_\infty \approx 5 \times 10^5$ to 8×10^5 per inch, the highest values of $R_{e,T}$ occurred when the bleed valve was open and the lowest values occurred when the bleed valve was closed. Therefore, while hot-wire spectral data have been recorded for the entire range of test conditions and at 1-in. intervals in X throughout the test rhombus, the spectral data presented in this report are limited to the above noted conditions since the effects of different spectra should be the most pronounced at these conditions.

Figures 12 to 15 show the power spectra of the hot-wire signal at several locations along the centerline with bleed valve open and closed for $R_\infty = 5.3$ and 7.9×10^5 per inch. Parts (a) of figures 12 to 15 show the original unsmoothed spectra with both the signal and instrument noise plotted to the same scale in volts squared per hertz against frequency in kilohertz. These figures are included to illustrate the proximity of the signal to the instrument noise that occurred in the upstream regions of the test rhombus, especially with the bleed valve open (figs. 12 and 13). At $f > 80$ or 100 kHz, depending on the value of R_∞ , the amplitude of the signal and noise are within the same decade of the log scale. Therefore, at frequencies above these values, the spectral data in parts (a) of figures 12 to 15 are plotted against staggered scales (which are shown on the right side of these figures) to improve the clarity of the high-frequency data. Thus, it is apparent that at these high frequencies, the signal and noise are nearly coincident for $X \leq 11.5$ in. with the bleed valve open (figs. 12 and 13). However, with the bleed valve closed (figs. 14 and 15) there is significant energy at high frequencies above the instrument noise that occurs for $X \geq 5.5$ in. These high-frequency data also show that in all cases for $X \geq 18.5$ in. there is measurable energy above instrument noise out to 200 kHz.

Parts (b) of figures 12 to 15 show the more conventional log-log plots of smoothed spectra where the ordinate is the free-stream noise in terms of $(\tilde{p}_\infty/\bar{p}_\infty)^2/\text{Hz}$. (The square of the instrument noise has been subtracted from the square of the signal at each of the 250 points used across the frequency bandwidth of the digital spectrum analyzer.) These plots are convenient to demonstrate any trends in the true physical spectra and to facilitate comparisons with other data. Thus, a feature of these spectra which differs from those in conventional tunnels is the rather prominent peak that was observed in the range of $f \approx 10$ to 40 kHz for $X \geq 12.5$ in. with the bleed valve open (figs. 12(b) and 13(b)) and for $X \leq 7.5$ in. with the bleed valve closed (fig. 14(b)). At the larger unit Reynolds number of $R_\infty = 7.9 \times 10^5$ per inch with bleed valve closed (fig. 15(b)), the spectral curves are more nearly flat for $X \leq 12.5$ in. out to frequencies of 40 to 80 kHz. The prominent high-frequency peaks in the present spectra appear to be characteristic of small rapid-expansion nozzles since this type of spectrum was also obtained in a Mach 5 rapid-expansion nozzle (ref. 13) when the wall boundary layer at the acoustic origin sources was turbulent. In the nozzles of both the present and previous investigations (ref. 13), the turbulent boundary layer at the acoustic origins was very thin and had developed with strong favorable pressure gradients. These factors presumably reduce the eddy sizes and increase the high-frequency radiation in accordance with Strouhal scaling parameters.

Free-stream spectra obtained in more conventional nozzles exhibit a rather characteristic form, examples of which are to be found in figure 8 of reference 21 for

Mach numbers of 2.0 and 4.5. For the present nozzle, it may be expected that the effect of the rapid expansion near the throat would fade with increasing values of X and that the spectra presented here would progressively assume the form prevailing in conventional tunnels. Figure 13(c), in which the spectra of figure 13(b) have been rescaled to facilitate comparison with other results, tests this expectation. The frequency scale has been converted to dimensionless form, $F = 2\pi fv/u_\infty^2$, and the ordinate values have also been scaled. In particular, for the final station only ($X = 24.5$ in.), the energy was normalized to produce an integral value of unity, whereas the energy for the stations forward of this was scaled such as to maintain the values in correct proportion. Thus, the relative growth of energy with increasing values of X is unaffected by the scaling. Also shown in figure 13(c) are previously unpublished spectra obtained in the JPL 20-Inch Tunnel at Mach 3.3 for three values of unit Reynolds number. Each of these has been scaled in the manner of the 24.5-in. spectrum, rendering direct intercomparison of the four spectra appropriate. It may be seen that, as expected, spectra obtained well downstream in the present nozzle resemble those from a conventional nozzle, except that the spectra for the two highest unit Reynolds numbers in the JPL tunnel do not have a well-defined peak as do the present spectra.

One further aspect of the spectra to be mentioned concerns the value of the frequency which is most amplified by a test-model boundary layer at the station near the onset of transition. For a flat-plate model, the stability theory shows that there exists at any specified value of Reynolds number, Mach number, etc., one particular frequency which has been amplified more than all others (refs. 6 and 24). For a cone, the analysis is rendered difficult because the geometrical effect causes oblique waves to become more two-dimensional during streamwise propagation. As previously mentioned, Malik² has calculated these frequencies for the present test conditions. For the conditions of figure 13(c), transition was observed on the cone at $R_{e,T} \approx 8.2 \times 10^6$, which corresponds to an amplification factor of $N \approx 10.5$. However, since the variation of N with F shows a rather broad peak, a band of frequencies is probably involved. Such a band is shown on the figure corresponding to a range in amplification factors from $N = 10$ to 10.5. The corresponding values of F indicate in a general way where the most "dangerous" frequencies lie with respect to the bulk of the fluctuation energy. In the present tunnel, some of the peculiar unit Reynolds number trends in the transition data, presented in the next section, may be related to the unusual spectral energy distributions seen in figures 12 to 15 as well as to the unique spatial distributions of tunnel noise (figs. 5 to 9).

Cone Transition Studies

Schlieren photographs.— Schlieren photographs of the flow over downstream portions of the cone in its two test positions in the nozzle are shown in figure 16. When the cone apex was positioned 5 in. downstream of the nozzle throat (fig. 16(a)), the 15-in-long cone was entirely within the test rhombus. The dark band on the left side of the photographs is due to the schlieren window frame. The nozzle exit is not visible but is 4.5 in. upstream of the cone base. The cone was then relocated 3 in. farther downstream, as shown in figures 16(b) and 16(c), to determine whether the generally larger noise levels farther downstream would reduce transition Reynolds numbers. However, the expansion waves from the nozzle exit then intersected the cone

²See footnote 1, p. 12.

about 1.8 in. upstream of the base or at 13.2 in. from the apex. Thus, the equilibrium temperature data may not be valid for $X > 13$ in. from the apex when the cone was in this location and when the thermocouple rows were at $\phi = 0^\circ$ and 180° .

Figure 16(c) pertains to $R_\infty \approx 3.8 \times 10^5$ per inch for which the boundary layer over the entire cone appears to be laminar as indicated by the sharply defined edge of the boundary layer visible in the upper part of the photograph. Apparently, for this condition, the expansion waves from the nozzle exit did not cause transition in the cone boundary layer. This result may be compared with figure 16(b) at $R_\infty \approx 5 \times 10^5$ per inch for which the boundary layer over most of this downstream portion of the cone appears to be turbulent. However, at this same value of R_∞ , but with the cone apex at 5 in. from the throat (fig. 16(a)), the boundary layer again appears to remain laminar to the cone base.

Equilibrium recovery factors.- Figures 17 and 18 show typical variations of the recovery factor r defined as

$$r = \frac{T_{aw} - T_e}{T_o - T_e} \quad (2)$$

plotted against the axial distance along the cone for bleed valve open and closed and for the two locations of the cone apex, $X_c = 5$ and 8 in. from the nozzle throat. Each part of figures 17 and 18 shows the data from a single run obtained over the range of R_∞ by starting at the lowest value of p_o and by then increasing p_o incrementally to the highest value. This operational sequence in stagnation pressure was followed for each run in the entire test series. The values of T_{aw} , the measured cone skin temperatures, were obtained after constant flow conditions were established, which resulted in nearly constant temperatures and avoided large heat conduction effects. The dashed lines are drawn at the theoretical laminar recovery factor of

$$r_L = \sqrt{Pr} \approx 0.843$$

The solid lines are for the turbulent recovery factor taken as

$$r_{Tu} = (Pr)^{1/3} \approx 0.892$$

The values of r were computed from equation (2) using the measured temperatures and were then displayed on the Hewlett-Packard 9845 CRT during the runs. After the values and trends of r remained essentially constant for about 1 min and agreed well with the theoretical value of r_L in the region ahead of transition, the data were then recorded and the final plots made.

The onset of transition was determined as the intersection of two straight lines faired through the laminar and transitional data as indicated in the figures. The slight increase in the measured values of r immediately upstream of transition is probably due to heat conduction effects in the 0.030-in-thick stainless steel skin. Nevertheless, the location of transition and the effects upon this in response to changes in noise levels with bleed valve open or closed and different axial

locations of the cone within the nozzle flow are clearly evident. Thus, comparison of figures 17(a) and 17(c) shows that closing the bleed valve caused transition to occur much farther forward than with the bleed valve open, especially for $R_e < 7.9 \times 10^5$ per inch, in accordance with the corresponding noise changes shown in figures 4 and 5. Similarly, from figures 17 and 18, it is clear that moving the cone downstream 3 in., which placed the apex 8 in. from the nozzle throat, again moved transition forward compared to the values for the upstream location at the same bleed valve setting and R_e . This change in transition location is due to the increases in the radiated noise incident on the cone. The run conditions, the distances to the onset and end of transition (taken as the peak location in r), and local transition Reynolds numbers for all the data used in this report are listed in table I.

The problem of heat conduction along the model skin must always be considered when measuring recovery temperatures. In the present model, there were significant heat conduction effects on the skin temperatures close to the cone base. Thus, since the cone base was 0.3 in. thick, it did not reach equilibrium temperature as quickly as the 0.030-in-thick skin. Because the entire cone was at room temperature before the runs started and, for a given run, if the cone surface recovery temperatures were below room temperature, the cone base was then too hot during the early part of the run when the temperature data for the lowest pressures were being recorded. Examples of this "hot base" effect are apparent at the two lowest pressures for the runs of figures 17(a) and 18(a) from the small increases in r for the three or four thermocouples nearest the cone base. The laminar recovery temperatures for these two runs at the lowest pressures were 53°F (fig. 17(a)) and 44°F (fig. 18(a)). Hence, until the thick base cooled to these lower temperatures, some of the cone thermocouples near the base indicated temperatures that were too high, resulting in a possible false indication of transition onset. The simplest check on this heat conduction effect was to increase the stagnation temperature sufficiently so that the laminar recovery temperature was at or slightly above room temperature. The results for two runs made at higher values of T_o are shown in figures 17(b) and 18(b) for direct comparison with the data of figures 17(a) and 18(a), respectively. The constant values of r seen for all thermocouples in the former runs at the two lowest values of p_o show clearly that transition occurred downstream of the last thermocouple ($X = 14.5$ in. from cone tip) at the two lowest unit Reynolds numbers. (The data at the highest unit Reynolds numbers were always obtained later in the runs, and the temperature of the base plate was then approximately the same as the cone recovery temperature.) Consequently, all data which showed a constant laminar value of r up to the three or four thermocouples nearest the base, where a slight increase in r was noted, were corrected to show that transition occurred downstream of the last thermocouple, $X = 14.5$ in. These corrected data are included in tables I(a) and I(b).

From this consideration of heat conduction effects, we may assume that upstream of the base, only one or two thermocouples ahead of the "true" location of transition were affected by heat conduction. This method of using the intersection point of the two straight line fairings of the data to determine the transition onset location is therefore believed to be reliable.

One final comment on the effect of mean flow disturbances from the nozzle exit on the cone boundary-layer flow can be made, based on the axial variations of recovery temperature along the cone. This mean flow disturbance is visible in the schlieren photographs of figure 16. With the cone apex at 8 in. from the nozzle throat, this disturbance intersects the cone at $X \approx 13$ in. However, the data of figure 18(b) ($X_c = 8$ in; $\phi = 180^\circ$) shows there was no adverse effect of the

flow disturbances since transition did not move ahead of the last thermocouple ($X = 14.5$ in.) at the two lowest values of R_∞ .

Effect of free-stream noise on X_T/X_{TE} . - From the recovery factor plots, it is apparent that the axial length of the transition region may vary considerably with free-stream noise. For example, figure 17(a), which is for bleed valve open and with the cone apex at 5 in. from the throat corresponding to the lowest average noise levels (recall figs. 5(a) and 5(b)), shows rather abrupt increases from laminar to turbulent values of r . In contrast with this result, figure 18(c), which corresponds to the highest average rms noise levels (at high frequencies) incident upon the cone figs. 5(c), 5(d), 14, and 15), shows much more gradual increases from laminar to turbulent recovery factors, especially at the lower values of R_∞ .

To determine whether these apparent differences in the extent or development rate of transition followed consistent trends, the ratios of X_T/X_{TE} were plotted in figure 19 against the local unit Reynolds number for all the transition data from table I. Again, by reference to the noise levels in figure 5 as well as to the spectral data of figures 12 to 15, it is apparent that the extent and level of the noise at the most critical frequencies ($50 \text{ kHz} < f < 80 \text{ kHz}$) tended to increase with increasing values of R_∞ or when the cone was moved downstream to the 8-in. location or, finally, when the bleed valve was closed. Figure 19 shows that the ratio X_T/X_{TE} indeed responded to all these factors and in the order listed. Thus, at the lowest values of R_e (which is about 8 percent larger than R_∞ for the present conditions) and with bleed valve open, the maximum values of the ratio X_T/X_{TE} are about 0.9. This value may be compared with results from the cone flight data of reference 26 (i.e., fig. 16 of ref. 26) where X_T/X_{TE} varied from about 0.84 to 0.92 for $1.6 < M_\infty < 1.9$. Typical wind-tunnel values (ref. 27) for this ratio are included for comparison in the lower right side of figure 19 which shows values ranging from about 0.6 to 0.75. These results obviously have important applications to the calculation of boundary-layer properties required for the design of supersonic vehicles.

Transition Reynolds number. - Before transition data from the present tests are discussed, it is appropriate to review briefly the previous wind-tunnel and flight data to be used for comparisons. Figure 20 shows typical data for $R_{e,T}$ plotted against R_e from four different wind tunnels (refs. 27 to 30) and from five different flight tests (refs. 26 and 31 to 34) of sharp cones at zero or small angle of attack in the range of $1.4 < M < 4.6$. These data are for the onset of transition, either as given in the original references or, when necessary, corrected to represent the onset according to the best information available from each particular reference. All the wind-tunnel data are for adiabatic wall temperatures, but only one set of flight data (ref. 26) is for adiabatic wall temperatures. The other flight data (refs. 31 to 34) are for cold-wall conditions with T_w/T_0 ranging from about 0.3 to 0.8. Four of these data points from references 32 and 33 are in about the same unit Reynolds number and transition Reynolds number ranges as the recent data of Fisher and Dougherty (ref. 26). Thus, the large favorable effect of wall cooling on transition Reynolds numbers as predicted by linear stability theory and confirmed by the flight data of reference 26 was not evident in these earlier cold-wall flight data (refs. 32 and 33). It is therefore likely that these earlier data may have been adversely affected by wall roughness or angle-of-attack effects as indicated by the comparatively low values of $R_{e,T}$.

The wind-tunnel transition Reynolds number data shown in figure 20 generally fall into two distinct groups. The spectra and rms values of the free-stream radiated noise are probably responsible for these two groups or levels in the values of $R_{e,T}$. The higher levels of $R_{e,T}$ from about 4×10^6 to 5.5×10^6 were obtained in

the AEDC 40 × 40-Inch Tunnel A or in other tunnels for $M_e < 1.9$. For M_∞ less than about 2, the intensity of the noise radiated by nozzle-wall turbulent boundary layers is generally much lower than at higher Mach numbers so that values of $R_{e,T}$ are higher. The radiated noise in the large Tunnel A is not only lower in rms levels than other tunnels for the same Mach number range (see fig. 11) but also has somewhat lower energy at the high critical frequencies (fig. 21 in ref. 22) due to the thicker turbulent boundary layers on the nozzle walls and, accordingly, the resulting values of $R_{e,T}$ are higher. On the other hand, all the wind-tunnel data in the lower levels of $R_{e,T}$ from about 2×10^6 to 3.5×10^6 are from smaller tunnels and for $2.5 < M_e < 4.4$. Thus, the tunnel size and Mach number range for these lower data levels more closely resemble the conditions of the present tests.

The present transition data are shown in figure 21 where $R_{e,T}$ is plotted against R_e for bleed valve open and closed and with the cone apex at 5 and 8 in. from the nozzle throat. The shaded bands represent the data from figure 20. Run conditions and other pertinent information for the present data are listed in table I where the run numbers are also included for easy cross reference. All the points plotted on the 45° lines in figures 21(a) and 21(b) represent conditions where transition was not observed on the cone (i.e., $X_T > 14.5$ in.). Thus, these 45° lines represent the cone-length Reynolds number for $X = 14.5$ in. The four parts of figure 21 (figs. 21(a) to 21(d)) are arranged in the order of generally increasing rms noise levels over the cone and/or increasing energy in the critical frequency range from $f = 50$ to 80 kHz. Thus, figure 21(a) is for $X_c = 5$ in. and for bleed valve open. According to figures 5(a), 5(b), 12, and 13, there is no measurable noise at the critical frequencies for stations up to 5.5 in. and 4.5 in. from the cone apex at $R_\infty \approx 5.3 \times 10^5$ per inch and $R_\infty \approx 7.9 \times 10^5$ per inch, respectively. This absence of noise at the critical frequencies over the upstream portion of the cone has the effect of delaying the onset of transition to the extent that the resulting values of $R_{e,T}$ are in the range of flight data. However, as R_e is increased, the noise levels and the high-frequency energy (spectra at the highest values of R_∞ are not shown) increase and the values of $R_{e,T}$ decrease toward the low level of the wind-tunnel data. It should be noted that this trend of decreasing transition Reynolds number with increasing unit Reynolds number is in opposition to the unit Reynolds effect usually observed in conventional wind tunnels as apparent, for example, in the data of figure 20.

Figure 21(b) is for the same conditions as figure 21(a) except that the cone was moved downstream by 3 in. which then subjected the cone boundary layer to higher average noise intensities and higher frequencies. The resulting values of $R_{e,T}$ at $R_e \approx 5.3 \times 10^5$ and 7.9×10^5 per inch were then reduced to the higher levels of the wind-tunnel data. However, for $R_e > 7.9 \times 10^5$ per inch, the values of $R_{e,T}$ are again in agreement with the lower range of wind-tunnel data.

The transition data, together with the free-stream noise levels and spectra provide indirect but significant information on the amplification of boundary-layer fluctuations in the region preceding transition. By the action of relocating the cone longitudinally within the test section, the noise incident upon these upstream regions of the laminar boundary layer on the cone was caused to vary from the very low levels originating from the laminar wall layers far upstream to those levels which correspond to transitional or turbulent wall layers. Figures 5(a) and 5(b) for the unit Reynolds numbers of 5.3×10^5 and 7.9×10^5 per inch, respectively, show that the location of transition on the model tended to remain at a fixed spatial location with respect to the nozzle. An inference to be drawn from this result is that sound field fluctuation energy was injected into the cone boundary layer at stations well downstream of the apex. It may be pointed out that the forcing theory

of Mack (refs. 24 and 25) describes a mechanism by which energy is transferred to the layer for stations ahead of the first neutral point, which lies approximately 1 in. from the cone apex in the present case; however, the forcing theory is not applicable to energy transfer downstream of this station. Thus, theoretical studies on the forcing and receptivity problem for downstream stations will be needed for clarification of the present results and of supersonic wind-tunnel data in general.

Figures 21(c) and 21(d) for $X_C = 5$ in. and 8 in., respectively, show further decreases in values of $R_{e,T}$, but only for $R_e < 7.9 \times 10^5$ per inch. The large decreases in values of $R_{e,T}$ for $R_e < 5.3 \times 10^5$ per inch are due to the high transitional noise levels (and corresponding high-frequency energy) at $X = 7.5$ and 10.5 in. as shown in figures 5(c) and 14. Again, the dependence of transition on the spatial location of an increase in noise within the tunnel, rather than on the total length of exposure on the cone, is shown by the values of X_T plotted on the cone surfaces in figure 5(c) for the two cone test positions. Of course, when the cone is moved downstream 3 in. (fig. 21(d)), the values of $R_{e,T}$ are reduced further, below the lowest levels of wind-tunnel data for 3×10^5 per inch $< R_e < 6 \times 10^5$ per inch. However, when $R_e > 7.9 \times 10^5$ per inch, the values of $R_{e,T}$ are about the same, regardless of the cone location since the rms noise field is then more nearly constant over the upstream regions of the cone and the spectra always contain high-frequency energy as shown by figure 15.

PROJECTIONS OF PILOT-TUNNEL PERFORMANCE

Figure 22 illustrates how the nozzle flow determines the shape and location of the quiet test core and how its vertical and horizontal dimensions are related to the longitudinal dimension. To determine whether any benefits might be gained from a larger nozzle and facility, consider the projected performance of a nozzle which would be three times larger than the present pilot nozzle.

For a laminar quiet test core the dimensions ΔX for the pilot nozzle given on page 10 would be increased by three times; but in order for transition to occur on the nozzle wall at geometrically similar locations, the values of the Reynolds number based on ΔX , $R_{\Delta X}$, would have to be the same and all disturbance wavelengths or roughnesses would have to be scaled in proportion to the boundary-layer thicknesses. Hence, the stagnation pressure would be reduced by one-third, but the thickness of the laminar boundary layer on the nozzle wall or on models at geometrically similar locations would be three times larger. Thus, not only would the laminar boundary layers be easier to probe, but the effects of roughness on transition for both the nozzle-wall and model boundary layers would be reduced because wall roughness and dust deposits tend to remain at the same absolute dimensions; therefore, even longer runs of laminar flow might occur. However, the main benefit that would be obtained from a nozzle scaled up by a factor of three is that the values of R_e in figure 21(a), for example, would be reduced by one-third but the values $R_{e,T}$ would presumably be about the same since there would be no tunnel noise present over the nozzle boundary layer or the upstream portions of the laminar boundary layer on a model. That is, the largest values of $R_{e,T}$ on a cone model are expected to be in the same range of 7×10^6 to 8.5×10^6 (or higher) but to occur at one-third the unit Reynolds number. Thus, from figure 20, the resulting transition data would lie in the same unit Reynolds number and transition Reynolds number ranges as the recent adiabatic wall flight data (ref. 26).

For a turbulent quiet test core, the values of R_{AX} would be three times larger at the same values of p_0 . Since R_D would then be three times larger, the noise levels would be lower than in the pilot nozzle, as indicated by extrapolations of the present turbulent data in figure 11. However, the most important benefit of the larger facility is that the nozzle-wall turbulent boundary layer would be about 2.5 times thicker (assuming that the turbulent boundary-layer thickness is approximately proportional to $X(R_{e,X})^{-0.2}$). Since the frequency content of the radiated noise varies approximately inversely as the turbulent boundary-layer thickness, the frequencies should be reduced considerably. Then, because at the same unit Reynolds numbers the critical frequencies for amplification of instability waves would be the same as in the pilot tunnel, these critical frequencies might not be present or their energy might be much reduced. Consequently, the values of $R_{e,T}$ on a model under these conditions at high unit Reynolds numbers might also be in the range of flight data.

CONCLUSIONS

Measurements of the free-stream fluctuating pressures have been obtained by hot-wire anemometry in a Mach 3.5 pilot quiet nozzle over a unit Reynolds number range from 2.5×10^5 to 16×10^5 per inch. Also, transition Reynolds numbers on a sharp tip 5° half-angle cone at zero angle of attack were determined over the same range of unit Reynolds numbers from equilibrium temperature measurements on the cone. The following conclusions concerning the characteristics of the noise field in the nozzle and the effects of this noise on transition are based on the data and comparisons with previous results as presented in this report:

Noise Field

1. Large axial variations in the noise levels and spectra were measured within the test rhombus.
2. The magnitude and spatial locations of these changes in noise levels depended on the unit Reynolds number and on whether the boundary-layer bleed valve was open or closed.
3. In all cases, the noise levels at the upstream end of the test rhombus were an order of magnitude, or more, below the levels at the mid and aft sections.
4. When the nozzle-wall boundary layers at the acoustic origins were fully turbulent, the noise levels at the midsection of the test rhombus were from 30 to 60 percent of the levels reported for other supersonic tunnels of comparable Mach number.
5. When the nozzle-wall boundary layers were laminar at the acoustic origins, the noise levels were nearly two orders of magnitude below those of other tunnels and there was no measurable disturbance energy above the instrument noise at the high critical frequencies corresponding to Tollmien-Schlichting wave amplification in supersonic laminar boundary layers on cones.

Transition

1. The Reynolds numbers for the onset of transition varied from approximately 2.0×10^6 up to 8.5×10^6 . A qualitative dependence of transition Reynolds number on the level and spectra of the noise incident upon the cone in the regions upstream of the transition location was noted.

2. When the bleed valve was open and the cone apex was at the upstream end of the test rhombus, the noise levels incident upon the upstream regions of the cone boundary layer were very low and there was no measurable noise energy above instrument noise at high frequencies. Both the values of transition Reynolds numbers and the extent of the transition region then agreed with flight data for unit Reynolds numbers of 7.9×10^5 per inch, or less.

3. As the unit Reynolds numbers were increased above 7.9×10^5 per inch, the transition Reynolds numbers decreased rapidly into the lower range of wind-tunnel values because of the increase in both noise levels and energy at high frequencies.

4. When the cone was moved 3 in. downstream and the bleed valve was open, the transition Reynolds numbers, for unit Reynolds numbers of 7.9×10^5 per inch or less, decreased into the upper range of wind-tunnel levels due to the increasing root-mean-square noise intensity and increasing noise energy at high frequencies.

5. When the bleed valve was closed, the root-mean-square intensities decreased but the noise energy at high frequencies increased and transition Reynolds numbers then decreased further to values somewhat above or below the lower levels of previous wind-tunnel data, depending on the cone location.

Langley Research Center
National Aeronautics and Space Administration
Hampton, VA 23665
July 6, 1983

REFERENCES

1. Laufer, John: Aerodynamic Noise in Supersonic Wind Tunnels. *J. Aerosp. Sci.*, vol. 28, no. 9, Sept. 1961, pp. 685-692.
2. Pate, S. R.; and Schueler, C. J.: Radiated Aerodynamic Noise Effects on Boundary-Layer Transition in Supersonic and Hypersonic Wind Tunnels. *AIAA J.*, vol. 7, no. 3, Mar. 1969, pp. 450-457.
3. Stainback, P. Calvin: Hypersonic Boundary-Layer Transition in the Presence of Wind-Tunnel Noise. *AIAA J.*, vol. 9, no. 12, Dec. 1971, pp. 2475-2476.
4. Dougherty, N. S., Jr.; and Fisher, D. F.: Boundary-Layer Transition on a 10-Deg Cone: Wind Tunnel/Flight Correlation. *AIAA-80-0154*, Jan. 1980.
5. Beckwith, I. E.: Development of a High Reynolds Number Quiet Tunnel for Transition Research. *AIAA J.*, vol. 13, no. 3, Mar. 1975, pp. 300-306.
6. Kendall, J. M.: Wind Tunnel Experiments Relating to Supersonic and Hypersonic Boundary-Layer Transition. *AIAA J.*, vol. 13, no. 3, Mar. 1975, pp. 290-299.
7. Beckwith, Ivan E.; Harvey, William D.; Harris, Julius E.; and Holley, Barbara B.: Control of Supersonic Wind-Tunnel Noise by Laminarization of Nozzle-Wall Boundary Layers. *NASA TM X-2879*, 1973.
8. Harvey, W. D.; Stainback, P. C.; Anders, J. B.; and Cary, A. M.: Nozzle Wall Boundary-Layer Transition and Freestream Disturbances at Mach 5. *AIAA J.*, vol. 13, no. 3, Mar. 1975, pp. 307-314.
9. Anders, J. B.; Stainback, P. C.; Keefe, L. R.; and Beckwith, I. E.: Fluctuating Disturbances in a Mach 5 Wind Tunnel. *AIAA J.*, vol. 15, no. 8, Aug. 1977, pp. 1123-1129.
10. Beckwith, I. E.; Anders, J. B.; Stainback, P. C.; Harvey, W. D.; and Srokowski, A. J.: Progress in the Development of a Mach 5 Quiet Tunnel. *Laminar-Turbulent Transition*, AGARD-CPP-224, May 1977, pp. 28-1 - 28-14.
11. Beckwith, Ivan E.; and Holley, Barbara B.: Gortler Vortices and Transition in Wall Boundary Layers of Two Mach 5 Nozzles. *NASA TP-1869*, 1981.
12. Anders, J. B.; Stainback, P. C.; and Beckwith, I. E.: New Technique for Reducing Test Section Noise in Supersonic Wind Tunnels. *AIAA J.*, vol. 18, no. 1, Jan. 1980, pp. 5-6.
13. Anders, J. B.; Stainback, P. C.; and Beckwith, I. E.: A New Technique for Reducing Test Section Noise in Supersonic Wind Tunnels, A Collection of Technical Papers - AIAA 10th Aerodynamic Testing Conference, Apr. 1978, pp. 354-364. (Available as AIAA Paper 78-817.)
14. Beckwith, Ivan E.; and Moore, William O., III: Mean Flow and Noise Measurements in a Mach 3.5 Pilot Quiet Tunnel. A Collection of Technical Papers - AIAA 12th Aerodynamic Testing Conference, Mar. 1982, pp. 48-70. (Available as AIAA-82-0569.)

15. Piatt, Michael J.: An Experimental Investigation of a Large ΔP Settling Chamber for a Supersonic Pilot Quiet Tunnel. NASA CR-3436, 1981.
16. Beckwith, I. E.: Comments on Settling Chamber Design for Quiet, Blowdown Wind Tunnels. NASA TM-81948, 1981.
17. Strikwerda, John C.: A Time-Split Difference Scheme for the Compressible Navier-Stokes Equations With Applications to Flows in Slotted Nozzles. Parallel Computations, Garry Rodrigue, ed., Academic Press, Inc., 1982, pp. 251-267.
18. Anders, J. B.; Stainback, P. C.; Keefe, L. R.; and Beckwith, I. E.: Sound and Fluctuating Disturbance Measurements in the Settling Chamber and Test Section of a Small, Mach 5 Wind Tunnel. ICIASF '75 Record, IEEE Publ. 75 CHO 993-6 AES, pp. 329-340.
19. Morkovin, Mark V.: Fluctuations and Hot-Wire Anemometry in Compressible Flows. AGARDograph 24, Nov. 1956.
20. Sonoda, T.; and Aihara, Y.: Effects of Pressure Gradient on the Secondary Instability of Gortler Vortices. AIAA-81-0197, Jan. 1981.
21. Laufer, John: Some Statistical Properties of the Pressure Field Radiated by a Turbulent Boundary Layer. Phys. Fluids, vol. 7, no. 8, Aug. 1964, pp. 1191-1197.
22. Strike, W. T., Jr.; Donaldson, J. C.; and Beale, D. K.: Test Section Turbulence in the AEDC/VKF Supersonic/Hypersonic Wind Tunnels. AEDC-TR-81-5, U.S. Air Force, July 1981. (Available from DTIC as AD A102 615.)
23. Pate, Samuel R.: Effects of Wind Tunnel Disturbances on Boundary-Layer Transition With Emphasis on Radiated Noise: A Review. AIAA-80-0431, Mar. 1980.
24. Mack, Leslie M.: Linear Stability Theory and the Problem of Supersonic Boundary-Layer Transition. AIAA J., vol. 13, no. 3, Mar. 1975, pp. 278-289.
25. Mack, Leslie M.: A Numerical Method for the Prediction of High-Speed Boundary-Layer Transition Using Linear Theory. Aerodynamic Analyses Requiring Advanced Computers - Part I, NASA SP-347, 1975, pp. 101-120.
26. Fisher, David F.; and Dougherty, N. Sam, Jr.: In-Flight Transition Measurement on a 10° Cone at Mach Numbers From 0.5 to 2.0. NASA TP-1971, 1982.
27. Van Driest, E. R.; and McCauley, W. D.: The Effect of Controlled Three-Dimensional Roughness on Boundary-Layer Transition at Supersonic Speeds. J. Aero/Space Sci., Apr. 1960, pp. 261-271, 303.
28. Pate, Samuel R.: Dominance of Radiated Aerodynamic Noise on Boundary-Layer Transition in Supersonic-Hypersonic Wind Tunnels - Theory and Application. AEDC-TR-77-107, U.S. Air Force, Mar. 1978. (Available from DTIC as AD A052 621.)
29. Laufer, John: Factors Affecting Transition Reynolds Numbers on Models in Supersonic Wind Tunnels. J. Aeronaut. Sci., vol. 21, no. 7, July 1954, pp. 497-498.

30. Laufer, John; and Marte, Jack E.: Results and a Critical Discussion of Transition-Reynolds-Number Measurements on Insulated Cones and Flat Plates in Supersonic Wind Tunnels. Rep. No. 20-96 (Contract No. DA-04-495-Ord 18), Jet Propul. Lab., California Inst. Technol., Nov. 30, 1955.
31. Rumsey, Charles B.; and Lee, Dorothy B.: Measurements of Aerodynamic Heat Transfer and Boundary-Layer Transition on a 15° Cone in Free Flight at Supersonic Mach Numbers Up to 5.2. NASA TN D-888, 1961.
32. Rabb, Leonard; and Simpkinson, Scott H.: Free-Flight Heat-Transfer Measurements on Two 20°-Cone-Cylinders at Mach Numbers From 1.3 to 4.9. NACA RM E55F27, 1955.
33. Merlet, Charles F.; and Rumsey, Charles B.: Supersonic Free-Flight Measurement of Heat Transfer and Transition on a 10° Cone Having a Low Temperature Ratio. NASA TN D-951, 1961. (Supersedes NACA RM L56L10.)
34. Rumsey, Charles B.; and Lee, Dorothy B.: Measurements of Aerodynamic Heat Transfer and Boundary-Layer Transition on a 10° Cone in Free Flight at Supersonic Mach Numbers Up to 5.9. NASA TN D-745, 1961. (Supersedes NACA RM L56B07.)

TABLE I.- RUN CONDITIONS, TRANSITION DISTANCES, AND TRANSITION REYNOLDS NUMBERS FOR ALL DATA USED IN FIGURE 21

(a) Figure 21(a); bleed valve open; $X_C = 5$ in.

Run	P_O' , psia	T_O' , $^{\circ}F$	$\times 10^{-5}$, in. ⁻¹	$\times 10^{-7}$, m ⁻¹	$\times 10^{-5}$, in. ⁻¹	x_T' , in.	$R_{e,T}$, $\times 10^{-6}$	$\frac{x_T}{x_{TE}}$	Main row deg
3	151.5	111.6	13.92	5.48	14.97	2.2	3.31	.55	1 180
	125.4	113.5	11.50	4.53	12.37	3.3	4.10	.67	
	100.3	115.8	9.08	3.58	9.77	4.9	4.81	.77	
	79.2	111.9	7.28	2.86	7.82	10.6	8.33	.91	
	54.9	113.1	5.03	1.98	5.40	12.8	6.94	.91	
	27.2	114.0	2.48	.98	2.67	>14.5	>3.89	—	
5	149.7	110.0	13.83	5.45	14.88	3.1	4.63	.66	1 180
	123.1	115.8	11.17	4.40	12.01	4.6	5.55	.75	
	96.1	117.3	8.67	3.41	9.32	4.7	4.40	.64	
	76.2	114.5	6.96	2.74	7.48	10.9	8.19	.91	
	52.0	117.2	4.71	1.85	5.06	13.4	6.81	—	
	24.7	117.0	2.24	.88	2.41	>14.5	>3.51	—	
23	152.1	99.7	14.42	5.68	15.50	1.8	2.80	.69	2 0
	120.8	100.0	11.50	4.53	12.36	3.7	4.59	.76	
	98.0	99.2	9.33	3.67	10.03	5.1	5.14	.76	
	74.8	104.2	7.02	2.76	7.55	8.3	7.04	.89	
	51.8	109.5	4.79	1.89	5.15	13.3	6.88	.90	
	30.6	105.3	2.87	1.13	3.08	>14.5	>4.49	—	
34	148.0	93.0	14.33	5.64	15.41	1.9	2.94	.51	1 180
	123.0	84.1	12.17	4.79	13.08	2.3	3.02	.52	
	96.3	84.7	9.58	3.77	10.30	4.0	4.14	.66	
	78.0	83.1	7.77	3.06	8.35	8.6	7.21	.86	
	51.9	83.3	5.17	2.03	5.55	12.6	7.02	.91	
	28.9	86.6	2.85	1.12	3.06	>14.5	>4.46	—	
35	148.2	102.3	14.00	5.51	15.05	2.2	3.32	.55	1 180
	124.6	105.5	11.67	4.59	12.55	2.9	3.65	.58	
	102.6	105.7	9.58	3.77	10.31	4.7	4.86	.71	
	76.4	101.6	7.22	2.84	7.76	10.5	8.18	.91	
	53.8	104.9	5.04	1.98	5.42	12.8	6.97	.90	
	29.5	104.9	2.77	1.09	2.98	>14.5	>4.33	—	
38	152.7	110.7	14.08	5.54	15.15	2.2	3.34	.63	2 0
	123.5	106.9	11.50	4.53	12.37	3.2	3.97	.71	
	108.5	112.3	9.75	3.84	10.49	4.8	5.05	.79	
	80.4	115.5	7.32	2.88	7.87	10.9	8.61	.92	
	51.7	114.6	4.72	1.86	5.07	>14.5	>7.38	—	
	43.7	116.6	3.97	1.56	4.27	>14.5	>6.21	—	
39	154.7	105.1	14.50	5.71	15.59	2.0	3.13	.67	2 90
	127.6	105.9	11.92	4.68	12.81	2.8	3.60	.72	
	103.4	108.8	9.58	3.77	10.31	4.3	4.45	.78	
	76.0	111.3	7.00	2.76	7.53	9.7	7.33	.87	
	52.7	114.9	4.80	1.89	5.16	>14.5	>7.51	—	
	41.2	109.9	3.81	1.50	4.10	>14.5	>5.96	—	
40	152.7	109.1	14.17	5.58	15.24	2.4	3.67	.60	1 270
	126.9	104.8	11.92	4.69	12.81	3.5	4.50	.73	
	94.8	105.6	8.83	3.48	9.50	5.9	5.63	.81	
	77.6	104.8	7.27	2.86	7.81	9.5	7.45	.83	
	50.6	108.4	4.69	1.85	5.05	>14.5	>7.34	—	
	41.9	106.8	3.90	1.54	4.19	>14.5	>6.10	—	
41	158.0	147.1	12.67	4.99	13.64	2.9	3.97	.66	1 270
	125.0	146.3	10.50	4.13	11.30	4.1	4.65	.75	
	99.6	152.6	8.23	3.24	8.86	6.8	6.05	.85	
	76.0	156.9	6.22	2.45	6.69	11.9	8.00	.89	
	69.1	159.2	5.63	2.21	6.06	>14.5	>8.82	—	
	44.3	163.5	3.57	1.40	3.84	>14.5	>5.59	—	

TABLE I.- Continued

(b) Figure 21(b); bleed valve open; $X_C = 8$ in.

Run	P_o' , psia	T_o' , $^{\circ}\text{F}$	$\frac{R_{\infty}}{in^{-1}} \times 10^{-5}$	$\frac{R_{\infty}}{m^{-1}} \times 10^{-7}$	$\frac{R_e}{in^{-1}} \times 10^{-5}$	X_T' , in.	$R_{e,T} \times 10^{-6}$	$\frac{X_T}{X_{TE}}$	Main ϕ , row deg
8	151.1	115.4	13.75	5.41	14.79	2.1	3.12	.57	1 180
	123.5	120.2	11.08	4.36	11.92	2.9	3.47	.62	
	102.9	113.7	9.42	3.71	10.13	3.7	3.76	.67	
	76.0	113.5	6.95	2.74	7.48	7.7	5.78	.87	
	51.3	108.5	4.76	1.87	5.12	10.5	5.39	.88	
	27.4	108.2	2.54	1.00	2.73 >14.5	>3.98	—	—	
10	128.0	116.2	11.58	4.56	12.46	2.8	3.50	.74	2 0
	100.4	112.9	9.17	3.61	9.86	3.7	3.66	.76	
	76.0	112.1	7.20	2.83	7.74	6.5	5.05	.82	
	52.8	118.2	4.77	1.88	5.13	10.2	5.25	.88	
	25.0	105.5	2.34	.92	2.52 >14.5	>3.67	—	—	
48	150.3	111.2	13.83	5.45	14.88	2.2	3.29	.67	1 180
	125.5	106.3	11.67	4.59	12.55	2.3	2.90	.59	
	97.9	108.7	9.08	3.58	9.77	3.3	3.24	.67	
	76.0	113.4	7.03	2.77	7.56	8.0	6.07	.88	
	51.5	110.6	4.75	1.87	5.11	10.2	5.23	.88	
	41.8	107.6	3.90	1.54	4.19	13.3	5.60	—	
	31.7	106.1	2.96	1.16	3.18 >14.5	>4.63	—	—	
50	150.5	150.1	12.50	4.82	13.46	2.5	3.38	.66	1 180
	121.5	146.2	10.17	4.00	10.94	3.0	3.30	.68	
	100.0	147.3	8.42	3.31	9.06	3.9	3.55	.72	
	78.5	150.0	6.53	2.57	7.03	8.3	5.86	.89	
	53.5	154.2	4.41	1.74	4.75	11.3	5.38	.89	
	43.2	165.4	3.46	1.36	3.72 >14.5	>5.42	—	—	
	32.0	164.2	2.58	1.01	2.77 >14.5	>4.04	—	—	
52	149.6	106.5	13.92	5.48	14.97	2.5	3.76	.74	1 270
	124.4	109.9	11.50	4.53	12.37	3.0	3.72	.73	
	98.3	103.6	9.25	3.64	9.95	3.5	3.49	.73	
	76.0	106.1	7.10	2.80	7.64	8.5	6.51	.87	
	51.4	107.5	4.78	1.88	5.14	12.2	6.30	.88	
	41.5	106.5	3.87	1.52	4.16 >14.5	>6.05	—	—	
	31.7	104.4	2.98	1.17	3.20 >14.5	>4.66	—	—	

TABLE I.- Continued

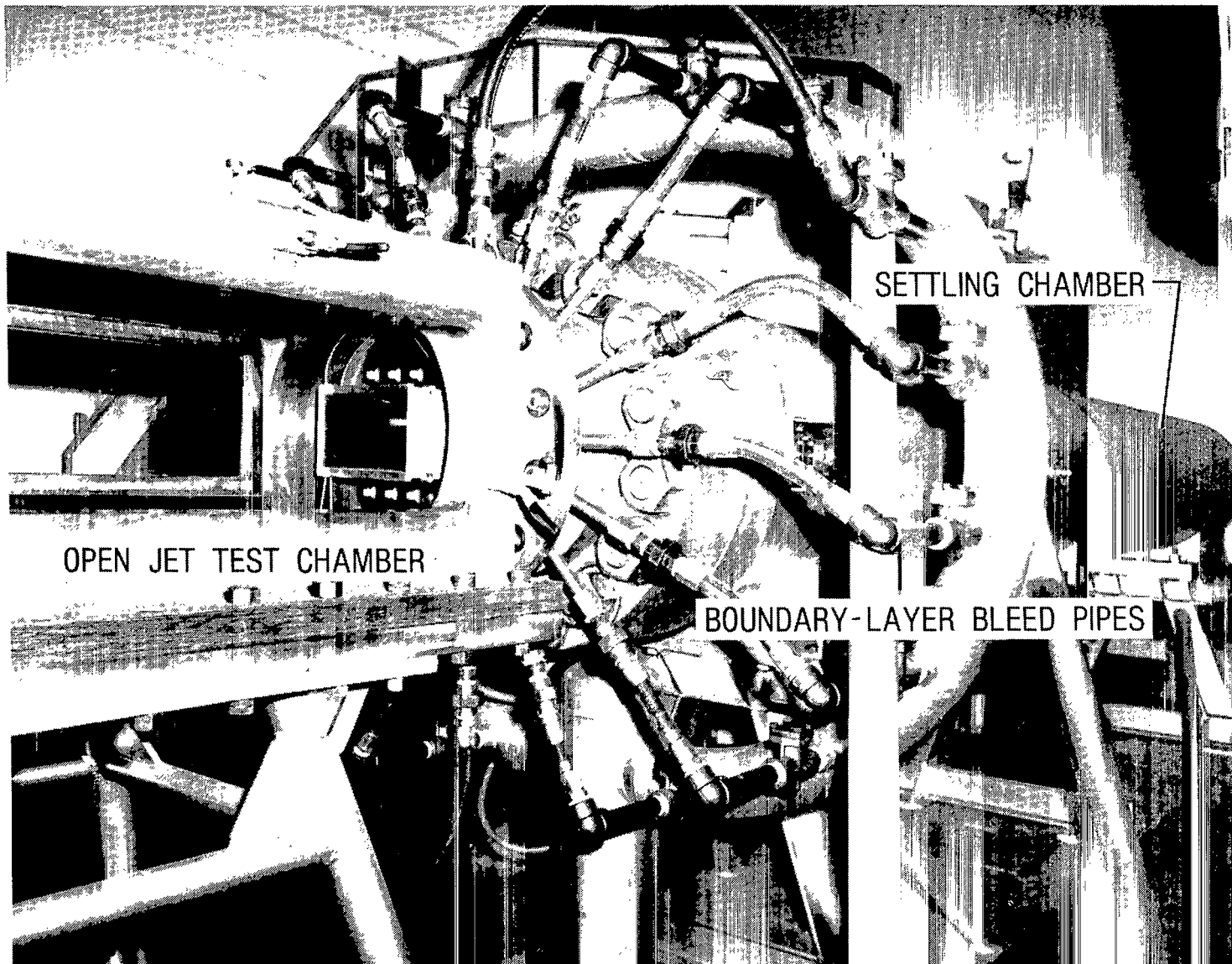
(c) Figure 21(c); bleed valve closed; $X_C = 5$ in.

Run	P_o' , psia	T_o' , $^{\circ}F$	$\frac{R_{\infty}}{10^{-5}}$, in^{-1}	$\frac{R_{\infty}}{10^{-7}}$, m^{-1}	$\frac{R_e}{10^{-5}}$, in^{-1}	X_T' , in.	$R_{e,T}$, $\times 10^{-6}$	$\frac{X_T}{X_{TE}}$	Main ϕ , row deg
4	147.0	114.2	13.42	5.28	14.43	2.5	3.62	.68	1 180
	124.4	116.6	11.25	4.43	12.10	3.7	4.49	.76	
	98.8	115.8	9.00	3.54	9.68	4.6	4.47	.79	
	75.9	123.6	6.76	2.66	7.27	5.7	4.16	.78	
	53.7	127.4	4.73	1.86	5.09	5.5	2.81	.66	
	26.3	115.9	2.39	.94	2.57	13.0	3.36	—	
18	153.0	104.8	14.33	5.64	15.41	2.8	4.33	.70	1 180
	126.4	107.1	11.75	4.63	12.64	3.5	4.44	.74	
	101.6	104.0	9.50	3.74	10.22	4.2	4.31	.76	
	78.9	101.0	7.56	2.98	8.13	5.2	4.24	.79	
	54.6	101.4	5.17	2.03	5.56	5.2	2.90	.68	
	31.6	103.9	2.97	1.17	3.19	12.0	3.84	.86	
19	149.9	99.7	14.25	5.61	15.32	2.3	3.54	.72	2 0
	124.1	99.1	11.83	4.66	12.72	3.2	4.09	.80	
	98.3	99.1	9.33	3.67	10.03	4.1	4.13	.80	
	78.1	99.5	7.52	2.96	8.08	5.2	4.22	.79	
	52.9	106.7	4.93	1.94	5.31	6.0	3.20	.73	
	32.3	108.0	3.00	1.18	3.23	12.4	4.02	.85	
36	151.2	112.6	13.83	5.45	14.88	1.9	2.84	.58	1 180
	123.7	117.5	11.17	4.40	12.01	2.4	2.89	.57	
	99.5	115.4	9.08	3.58	9.77	3.5	3.43	.67	
	75.1	114.0	6.86	2.70	7.38	5.1	3.78	.76	
	57.6	111.8	5.29	2.08	5.69	5.4	3.09	.72	
	43.9	118.2	3.97	1.56	4.27	9.4	4.03	.81	
	27.8	111.9	2.57	1.01	2.76	12.6	3.49	—	
53	148.3	110.7	13.67	5.38	14.70	2.5	3.69	.68	1 180
	123.9	110.2	11.42	4.49	12.28	3.0	3.70	.71	
	99.8	111.2	9.17	3.61	9.86	3.6	3.56	.73	
	75.4	114.1	6.88	2.71	7.40	4.8	3.57	.79	
	53.4	112.4	4.90	1.93	5.27	5.3	2.80	.71	
	40.7	109.4	3.76	1.48	4.04	9.9	4.02	.81	
	31.4	108.1	2.92	1.15	3.14	11.8	3.72	.84	

TABLE I.- Concluded

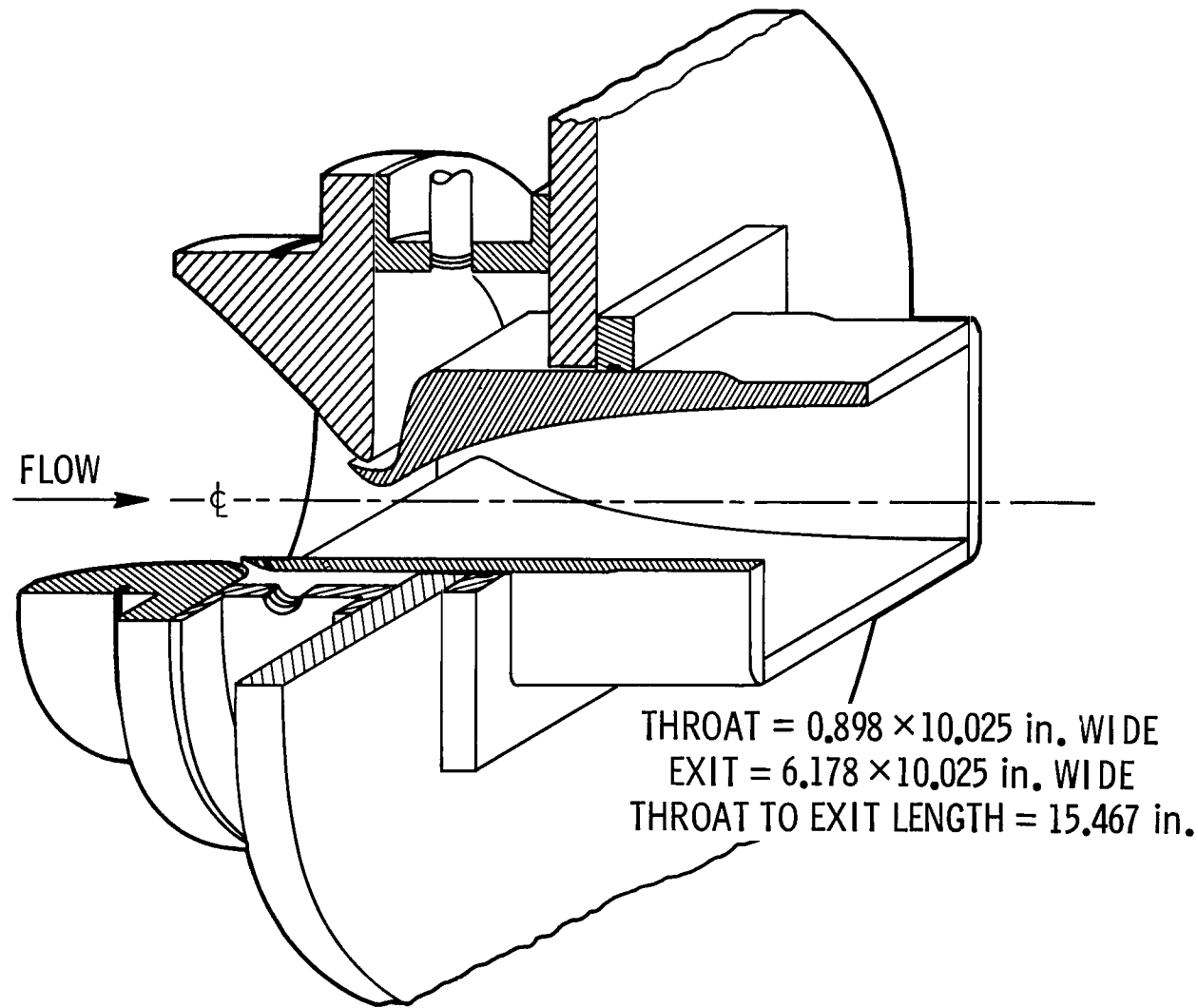
(d) Figure 21(d); bleed valve closed; $X_C = 8$ in.

Run	P_o' , psia	T_o' , $^{\circ}F$	$\frac{R_{\infty}}{10^{-5}}$, in^{-1}	$\frac{R_{\infty}}{10^{-7}}$, m^{-1}	$\frac{R_e}{10^{-5}}$, in^{-1}	X_T' , in.	$R_{e,T}$, $\times 10^{-6}$	$\frac{X_T}{X_{TE}}$	Main ϕ , row deg
9	150.9	120.7	13.50	5.31	14.52	2.7	3.94	.61	1 180
	126.4	123.7	11.25	4.43	12.10	3.1	3.77	.62	
	97.4	125.3	8.67	3.41	9.32	4.2	3.93	.69	
	77.6	116.9	7.03	2.77	7.57	5.4	4.10	.78	
	52.8	121.0	4.73	1.86	5.09	4.1	2.10	.59	
	27.8	114.0	2.54	1.00	2.73	9.4	2.58	.81	
49	150.6	110.1	13.92	5.48	14.87	2.2	3.31	.61	1 180
	122.4	113.7	11.17	4.40	12.01	2.6	3.13	.65	
	96.6	115.0	8.83	3.48	9.50	3.3	3.15	.69	
	75.7	111.1	6.97	2.74	7.49	4.3	3.23	.72	
	47.7	104.5	4.47	1.76	4.80	3.5	1.69	.57	
	43.6	106.0	4.07	1.60	4.37	5.4	2.37	.70	
	31.3	107.2	2.92	1.15	3.14	7.3	2.30	.77	
51	149.8	111.6	13.75	5.41	14.79	2.5	3.71	.74	1 270
	122.0	109.4	11.25	4.43	12.10	2.9	3.52	.74	
	98.3	111.2	9.08	3.58	9.77	3.5	3.43	.78	
	77.0	112.4	7.07	2.78	7.60	4.3	3.28	.78	
	52.5	108.1	4.88	1.92	5.24	4.2	2.21	.68	
	42.0	113.1	3.84	1.51	4.13	5.6	2.32	.73	
	32.1	118.6	2.89	1.14	3.11	7.0	2.19	.70	



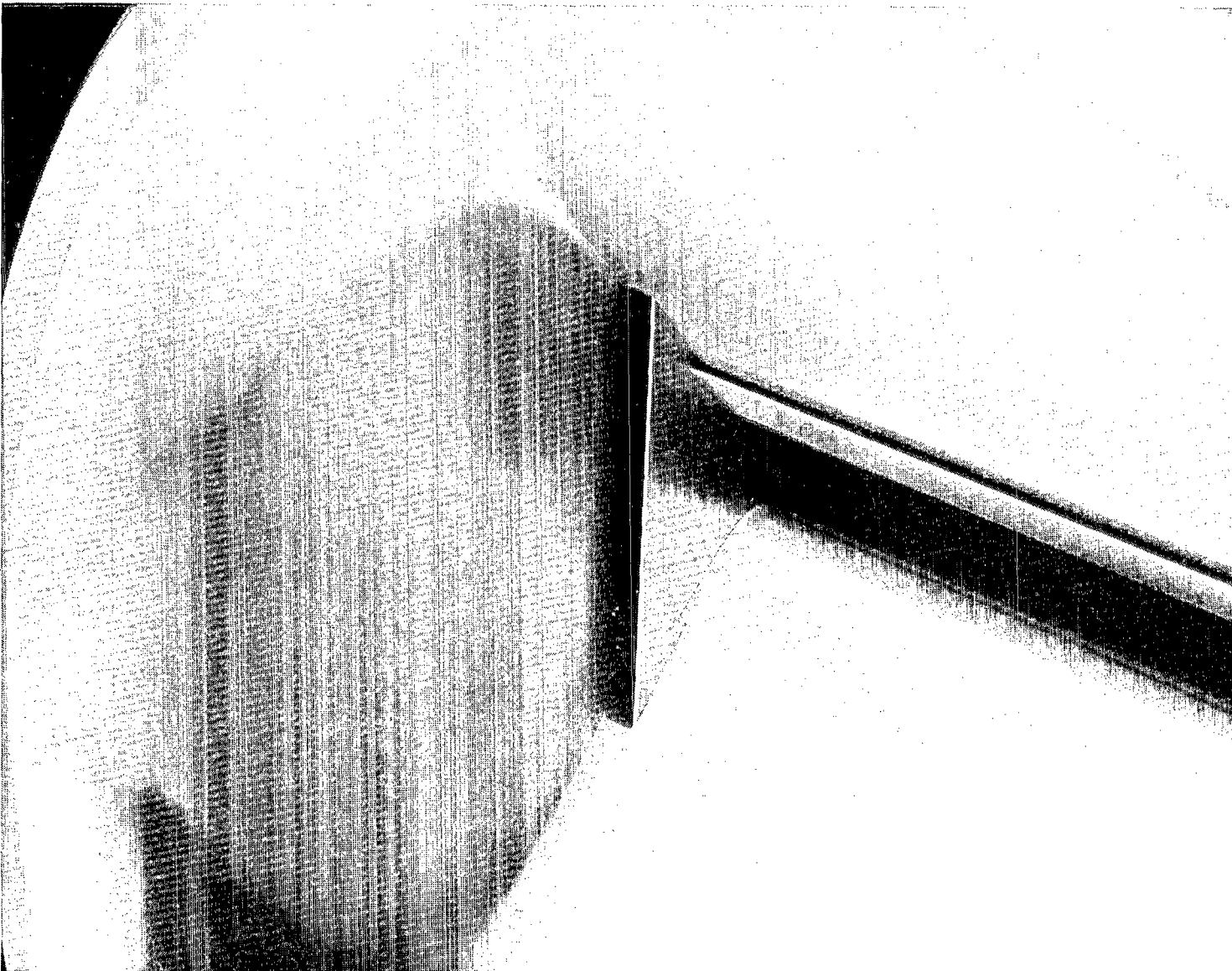
L-83-98

Figure 1.- Pilot low-disturbance tunnel at the Langley Research Center.



(a) Cutaway isometric sketch showing boundary-layer bleed slots in subsonic approach and slot suction plenum.

Figure 2.- Mach 3.5 two-dimensional nozzle.



L-83-99

(b) Photograph of subsonic approach showing details of sidewall and contour wall boundary-layer bleed slots.

Figure 2.- Concluded.

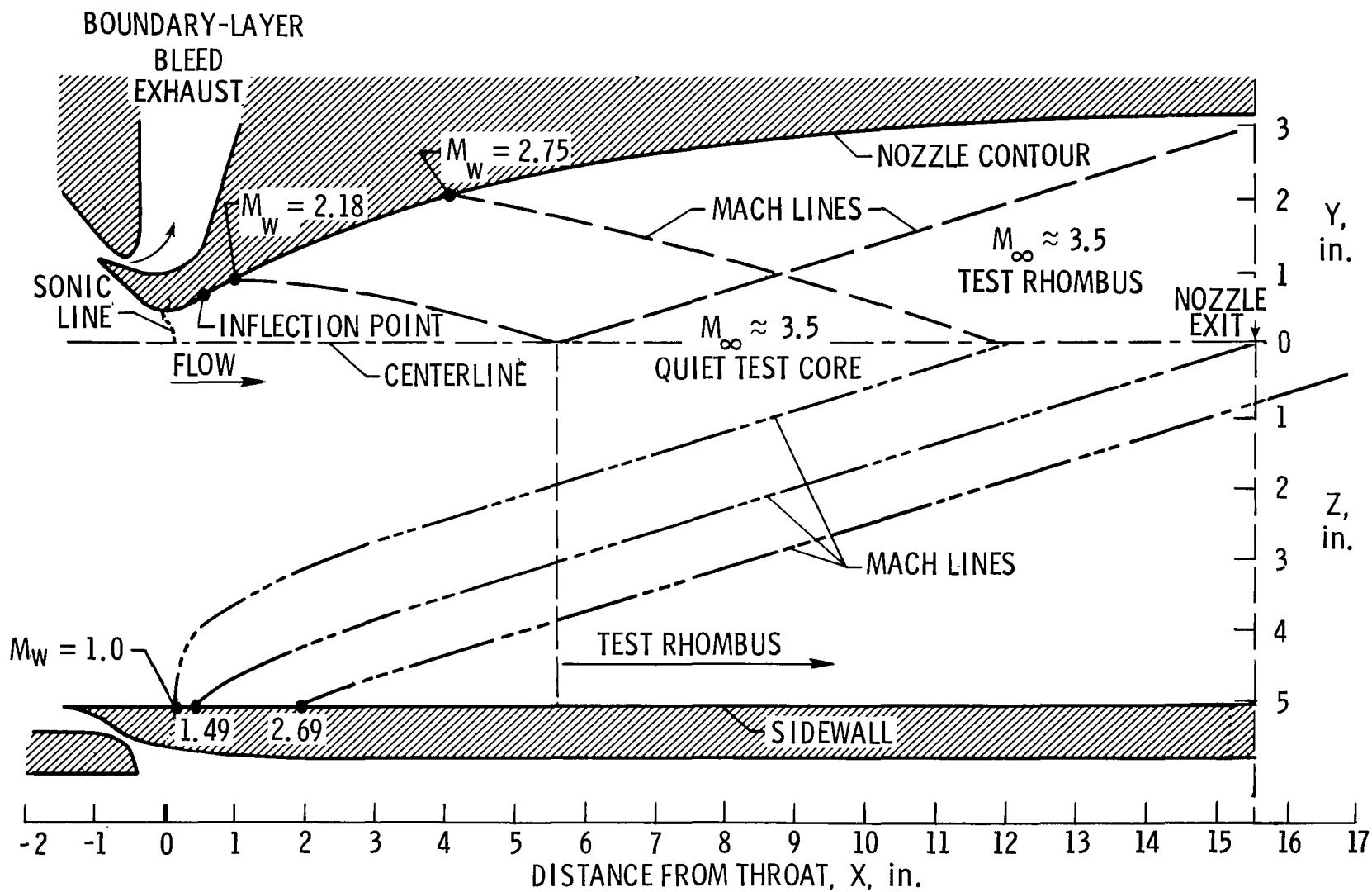
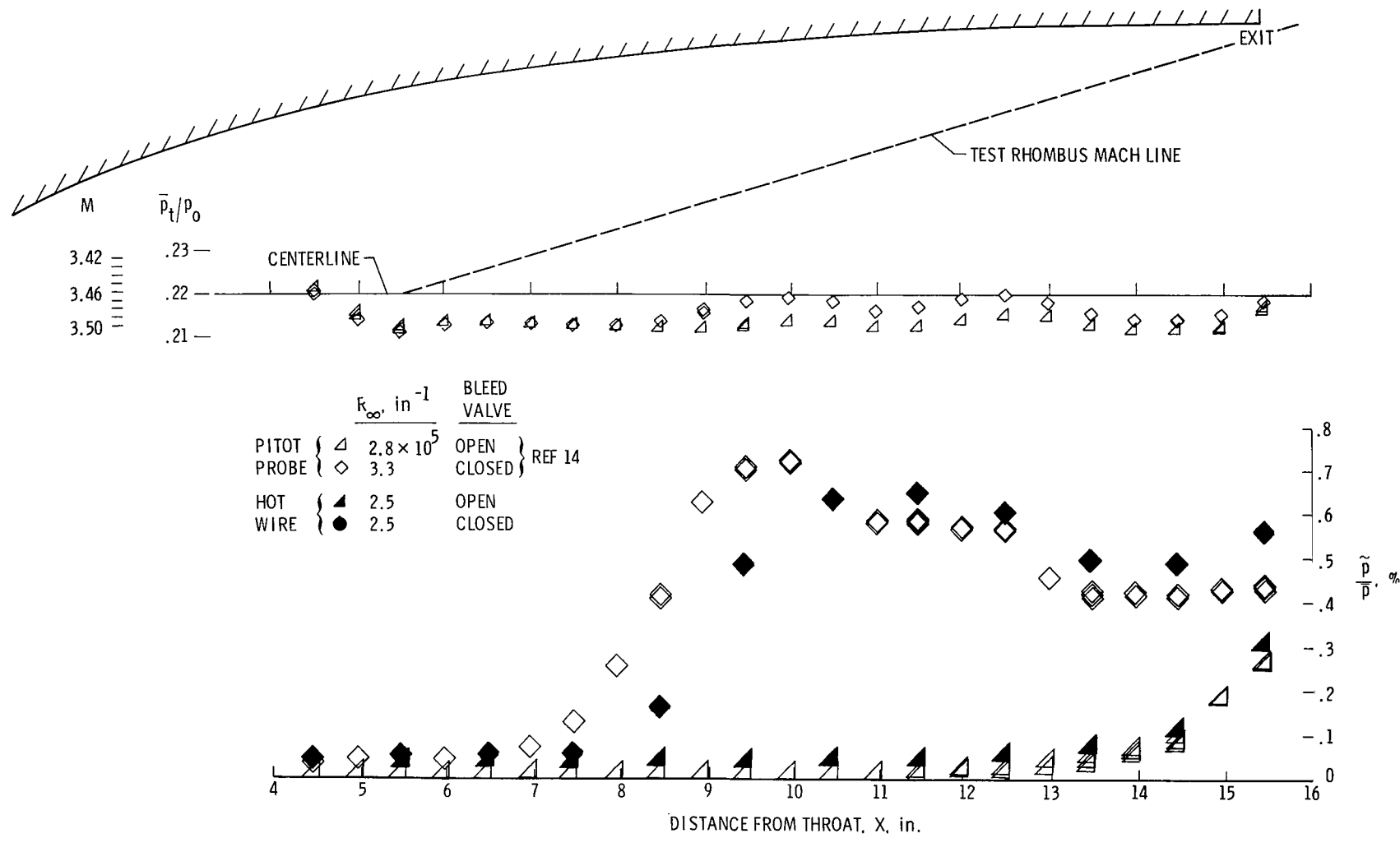
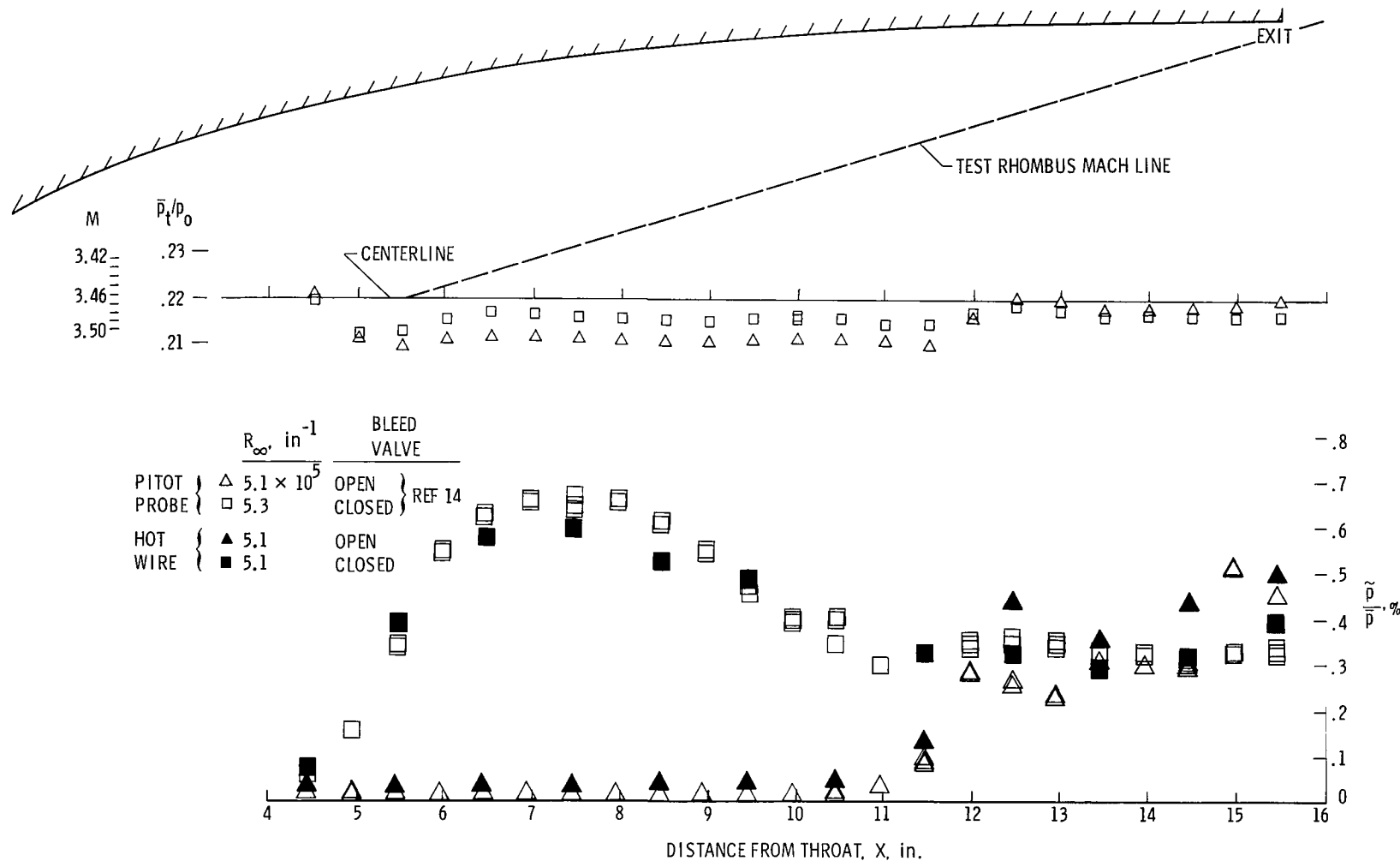


Figure 3.- Nozzle wall cross sections and Mach lines in vertical and horizontal center planes of nozzle.



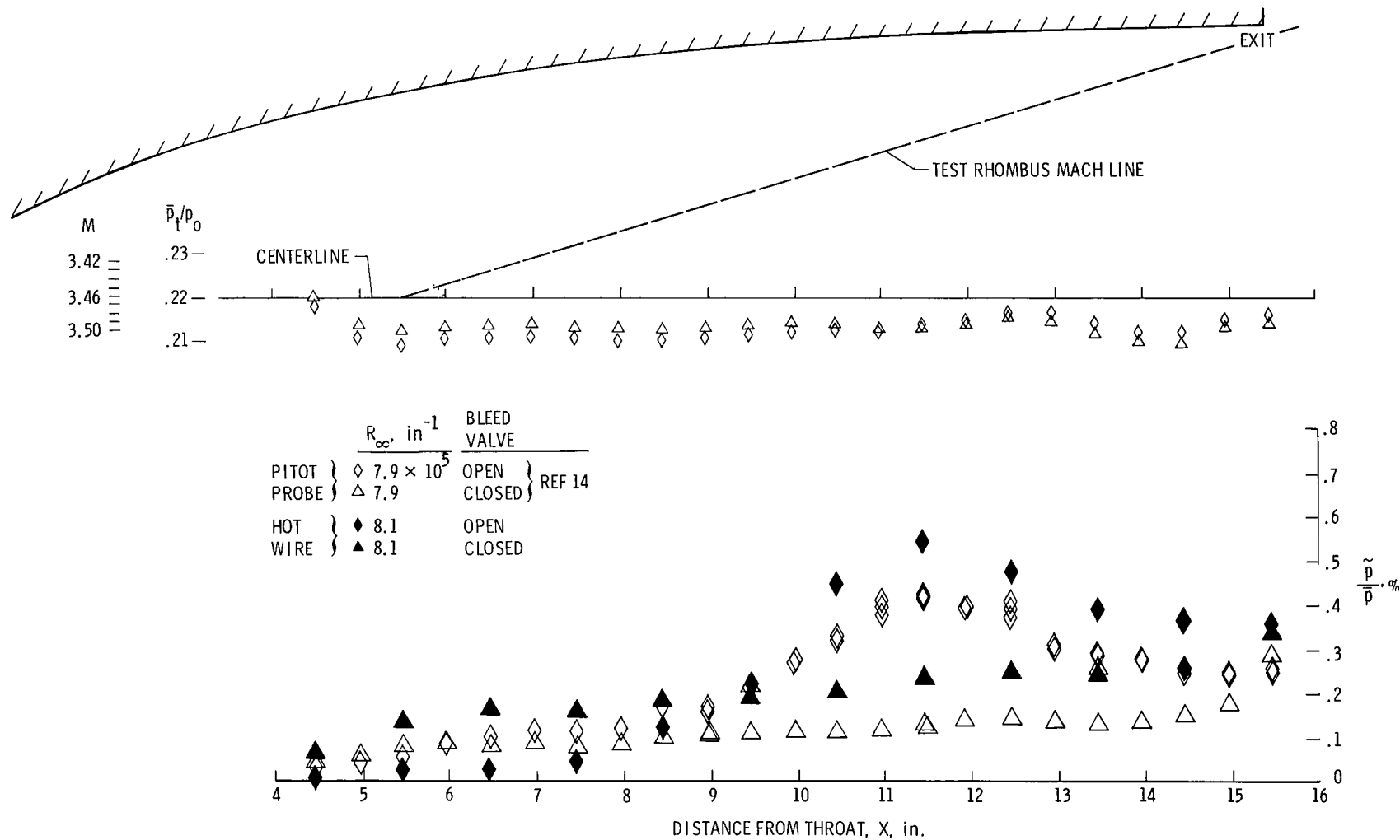
$$(a) \quad R_\infty \approx 2.5 \times 10^5 \text{ per inch.}$$

Figure 4.- Variation along nozzle centerline of normalized mean pitot pressure (small symbols) and rms fluctuating pitot pressure from reference 14 for comparison with present hot-wire measurements of rms static pressure.



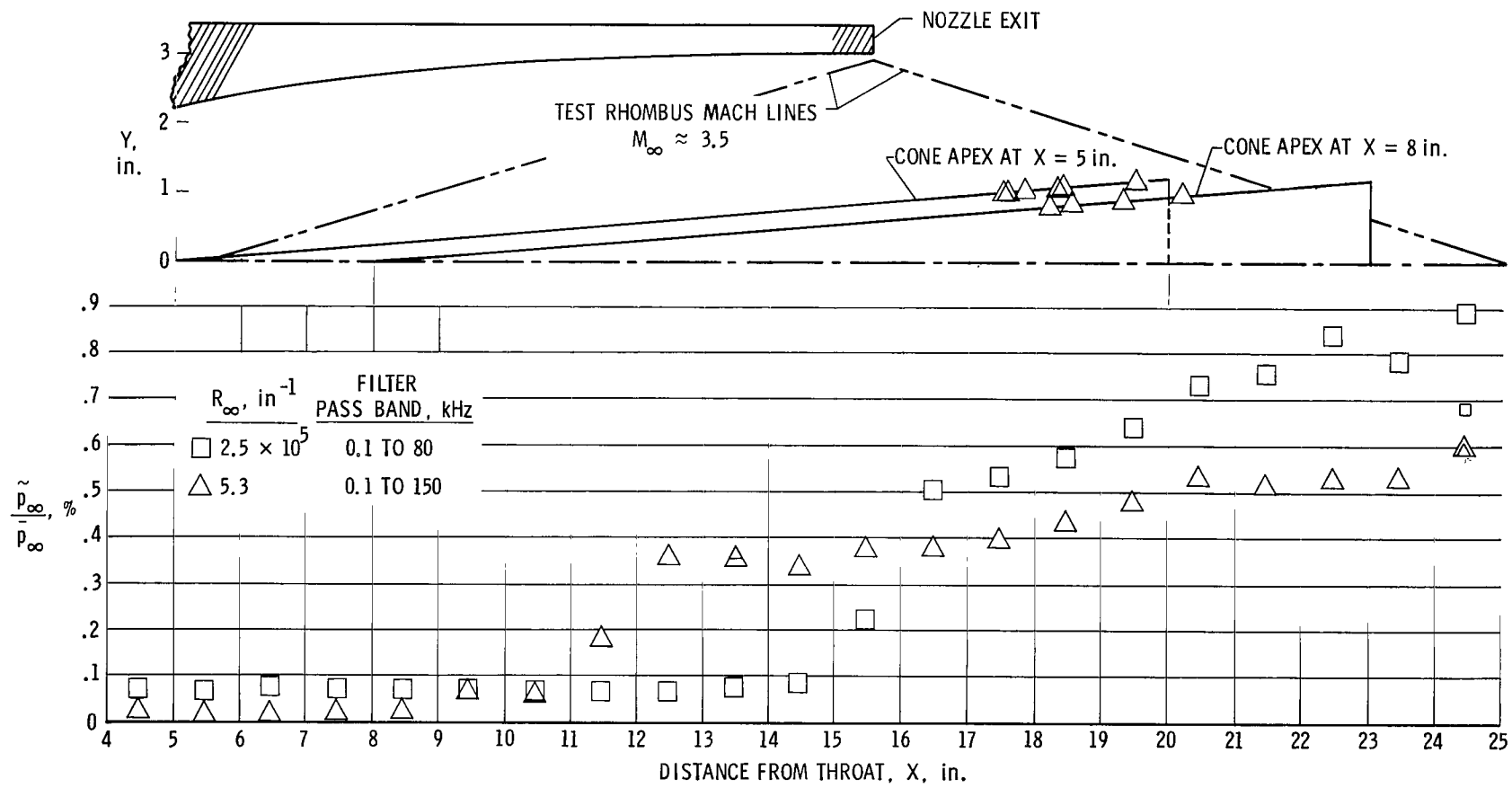
(b) $R_\infty \approx 5.1 \times 10^5$ per inch.

Figure 4.- Continued.



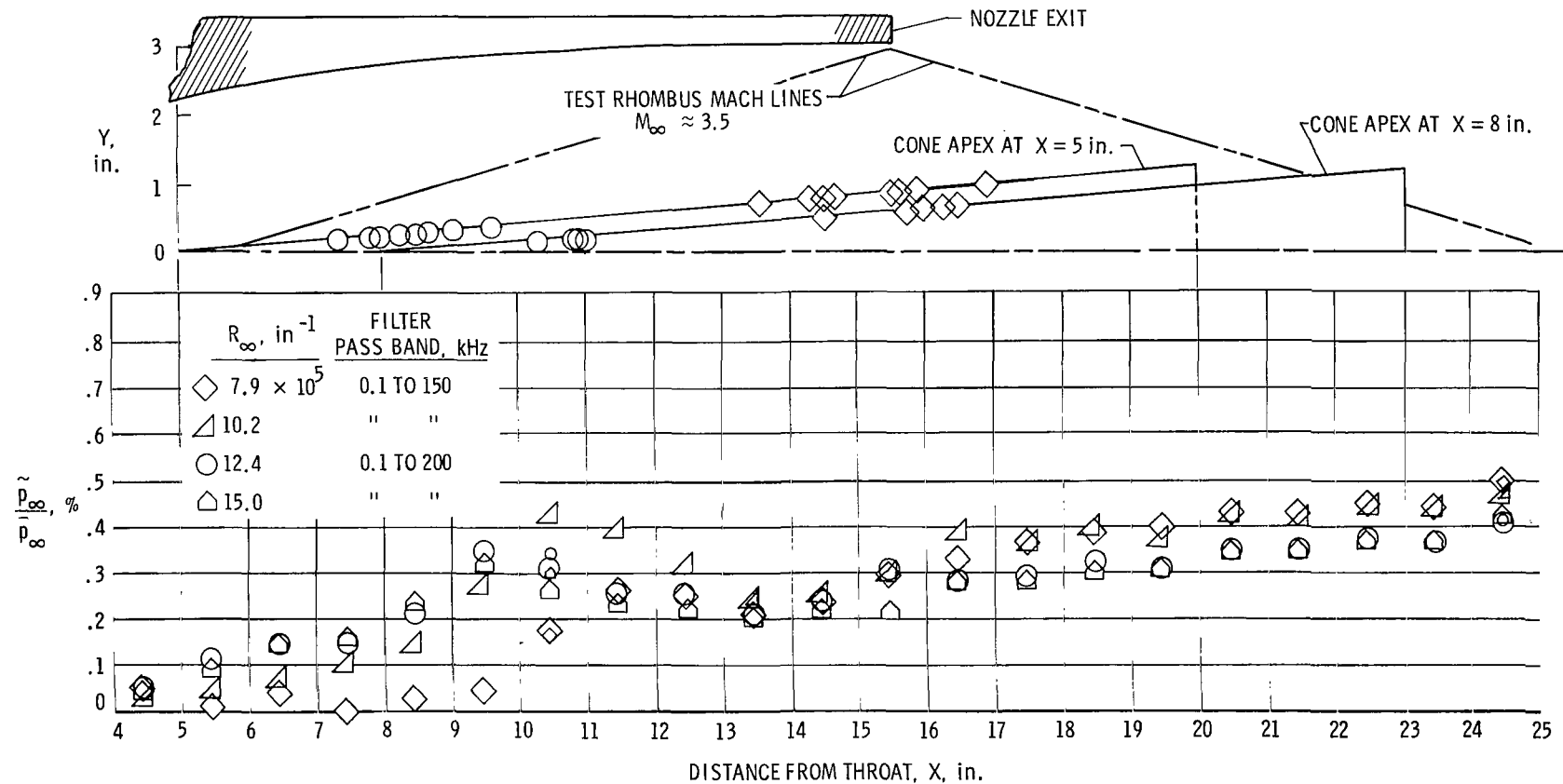
(c) $R_\infty \approx 8.0 \times 10^5$ per inch.

Figure 4.- Concluded.



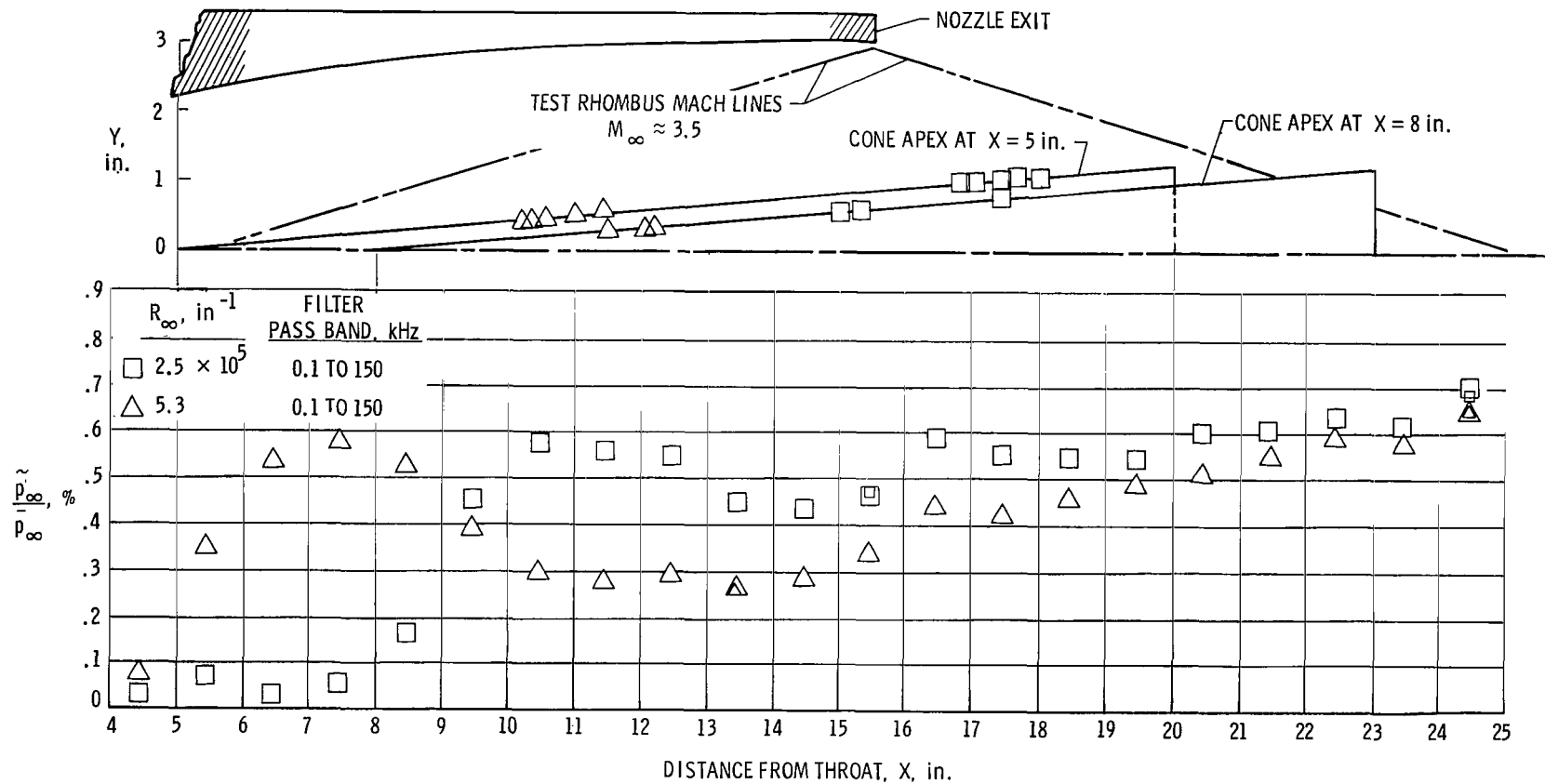
(a) $R_\infty \approx 2.5$ and 5.3×10^5 per inch; bleed valve open.

Figure 5.- Variation along centerline of normalized rms static pressure from hot-wire measurements at $Y = 0$ and $Z = 0$. Upper part of figure shows locations of transition x_T on the cone in its two test positions. Small symbols are for data derived from mode plots.



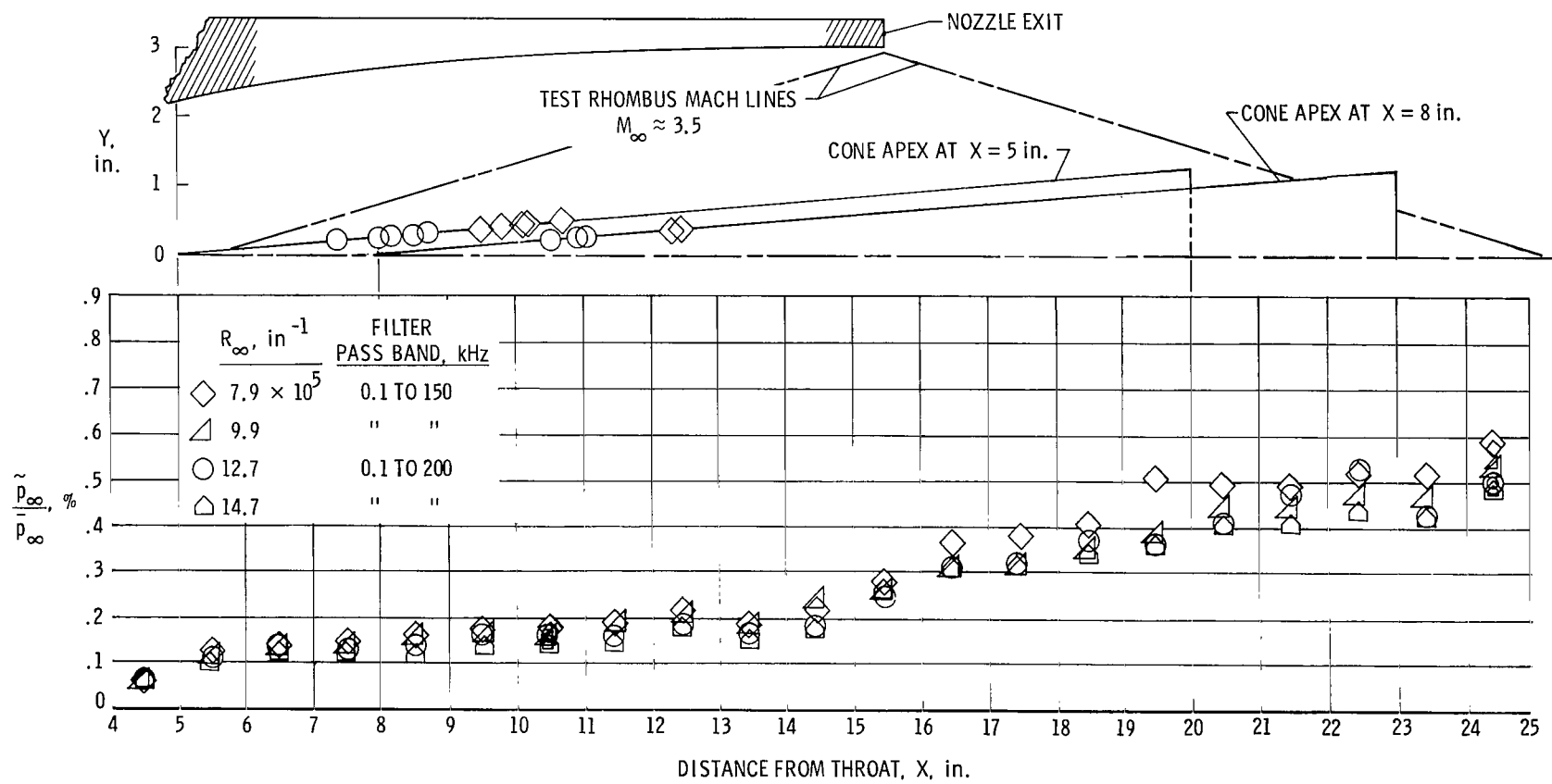
(b) $R_\infty \approx 7.9$ to 15.0×10^5 per inch; bleed valve open.

Figure 5.- Continued.



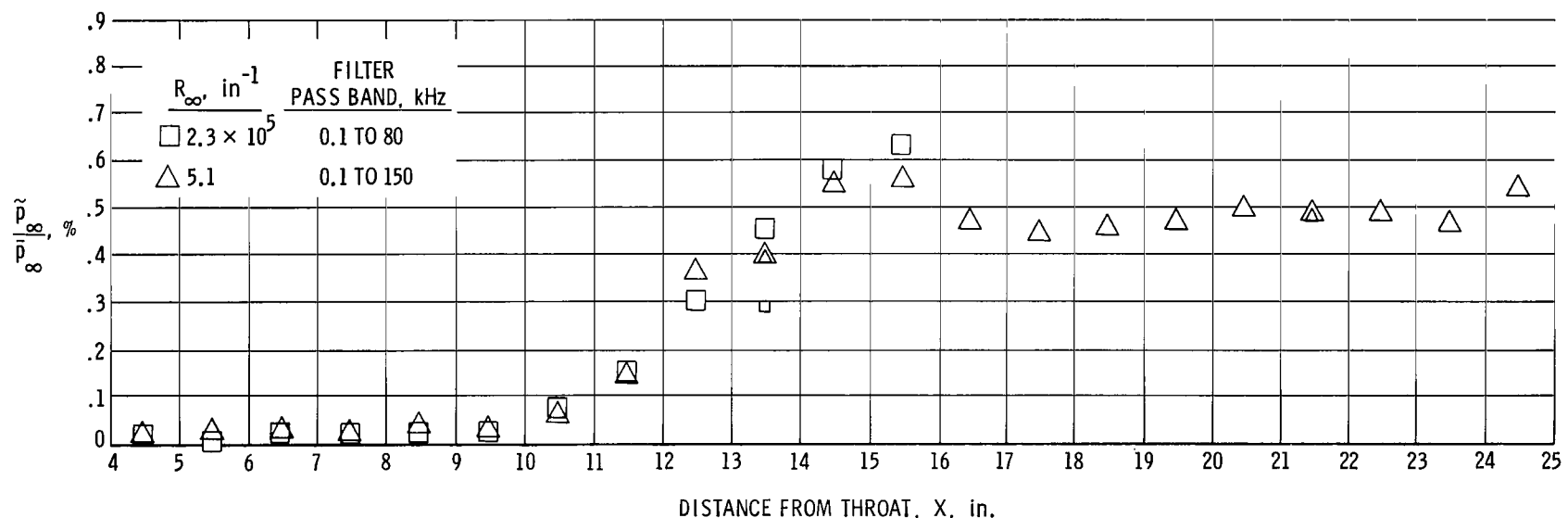
(c) $R_\infty \approx 2.5$ and 5.3×10^5 per inch; bleed valve closed.

Figure 5.- Continued.

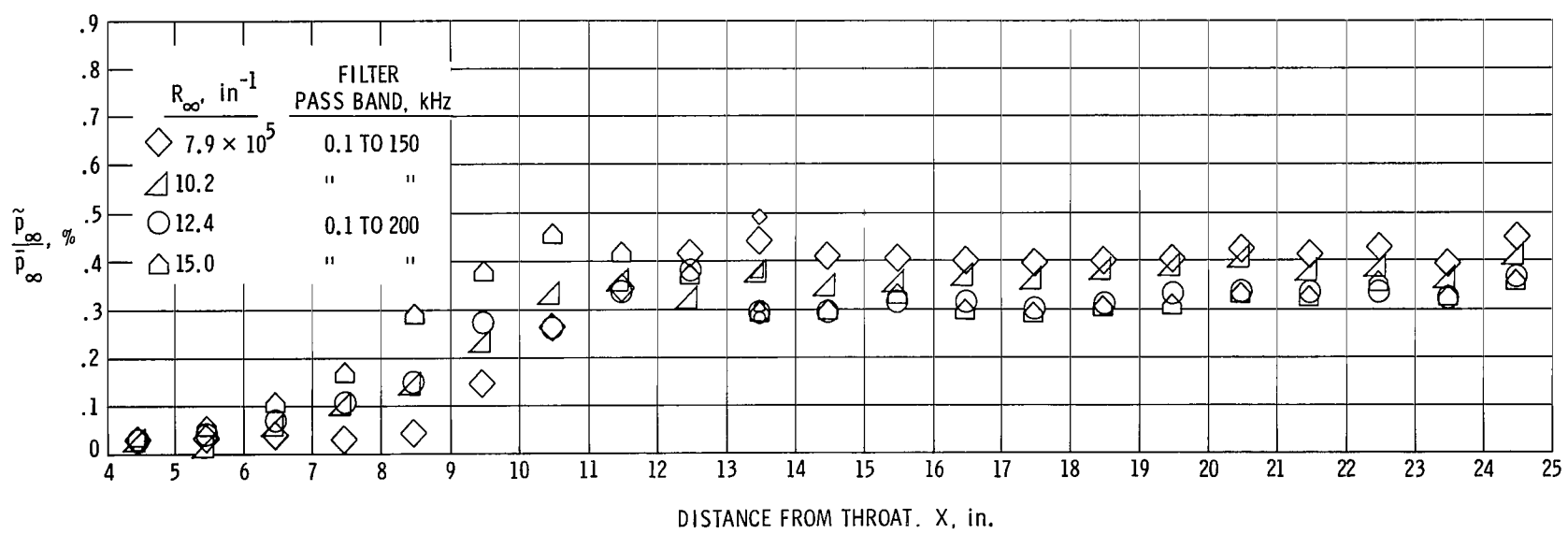


(d) $R_\infty \approx 7.9$ to 14.7×10^5 per inch; bleed valve closed.

Figure 5.- Concluded.



(a) $R_\infty \approx 2.3$ and 5.1×10^5 per inch; bleed valve open.



(b) $R_\infty \approx 7.9$ to 15.0×10^5 per inch; bleed valve open.

Figure 6.- Variation of normalized rms static pressure with X at $Y = 0$ and $Z = -2$ in. Small symbols are for data derived from mode plots.

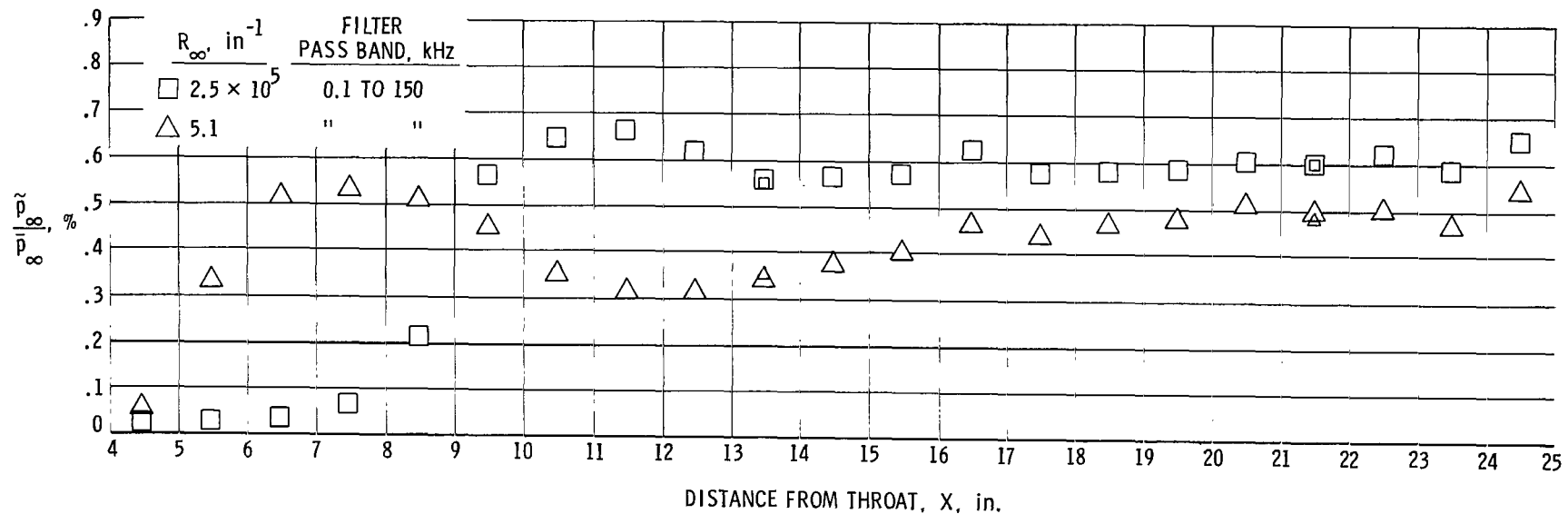
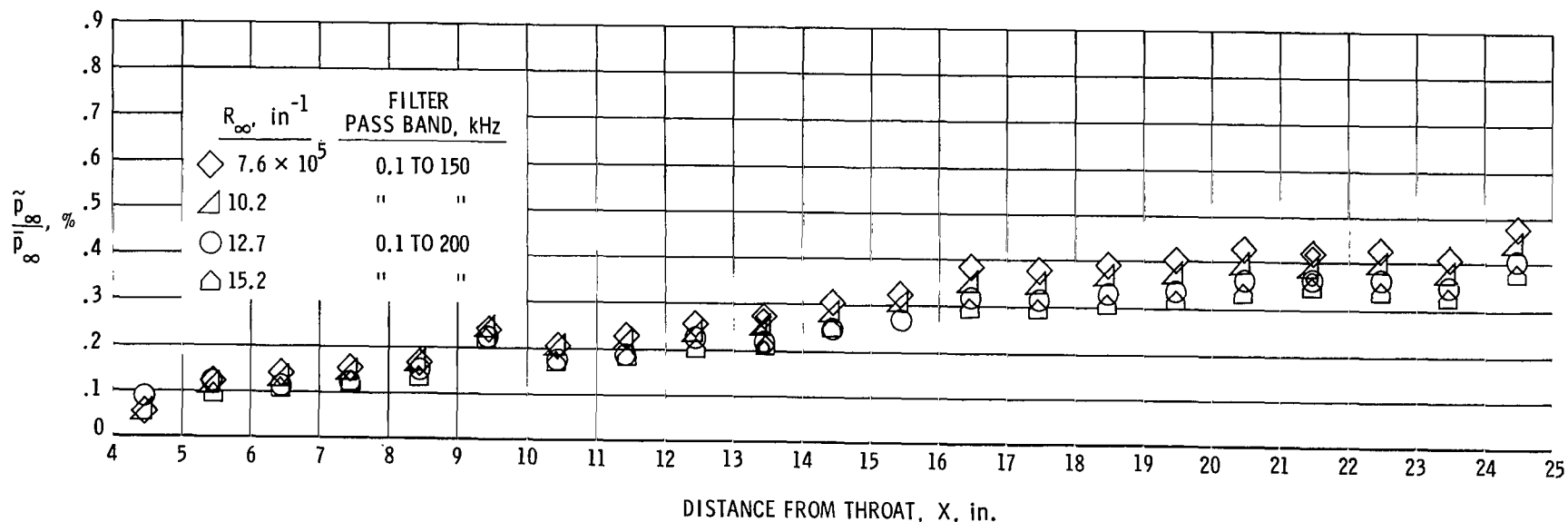
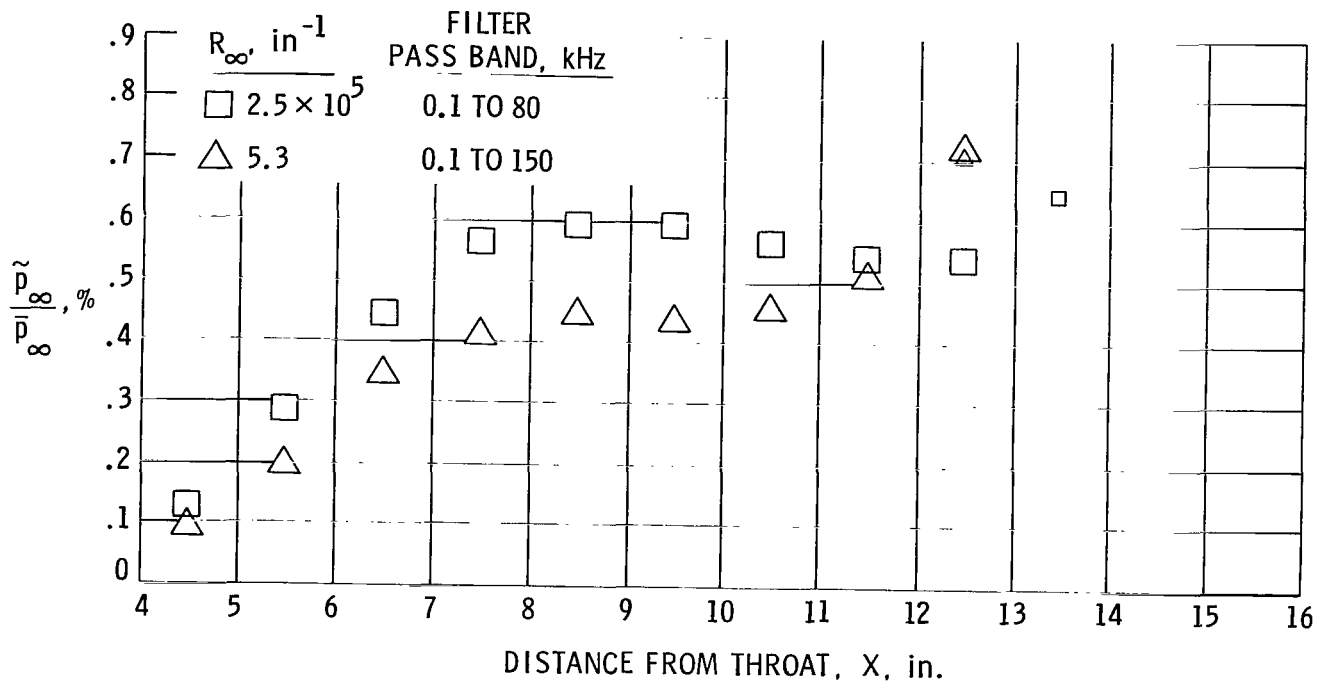
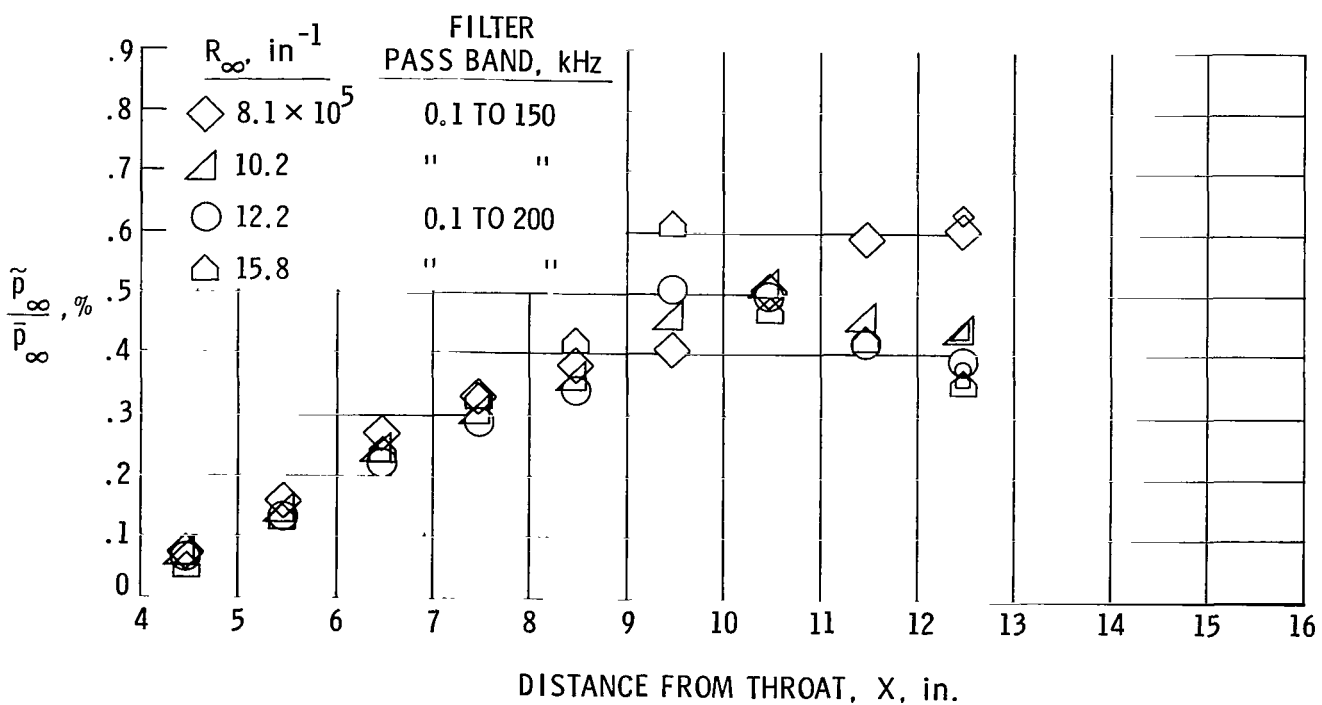
(c) $R_\infty \approx 2.5$ and 5.1×10^5 per inch; bleed valve closed.(d) $R_\infty \approx 7.6$ to 15.2×10^5 per inch; bleed valve closed.

Figure 6.- Concluded.

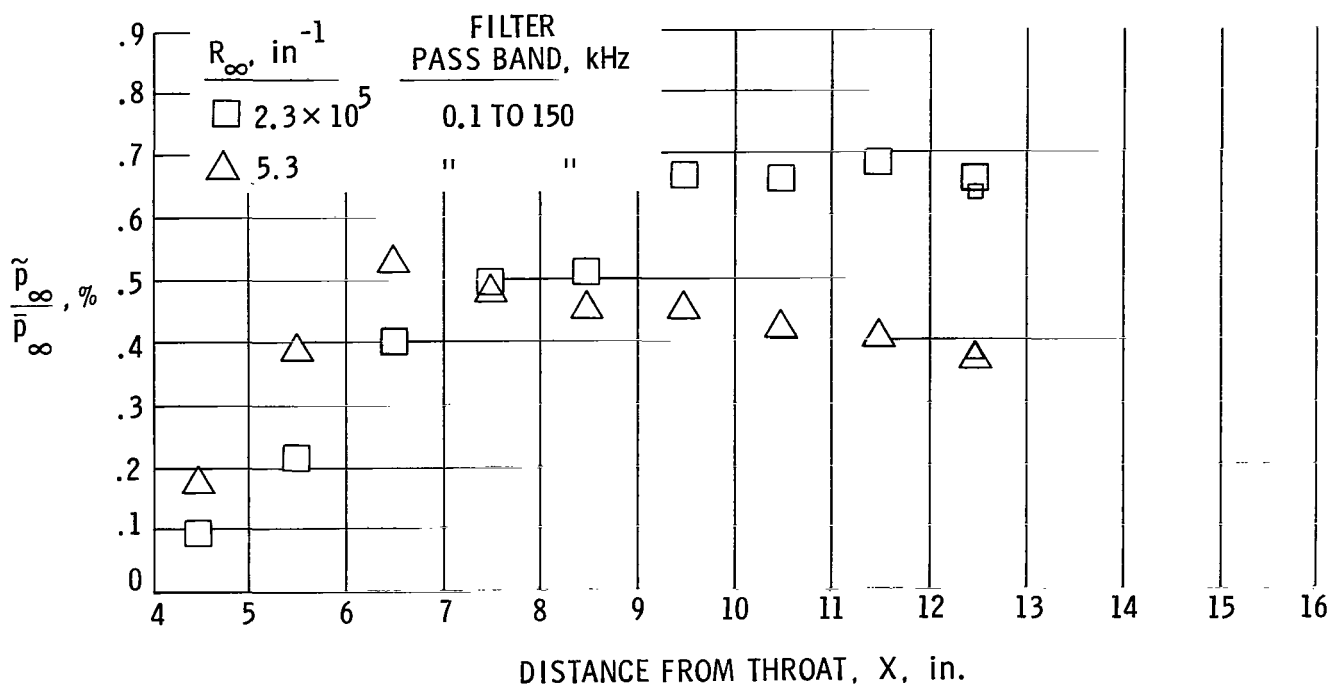


(a) $R_\infty \approx 2.5$ and 5.3×10^5 per inch; bleed valve open.

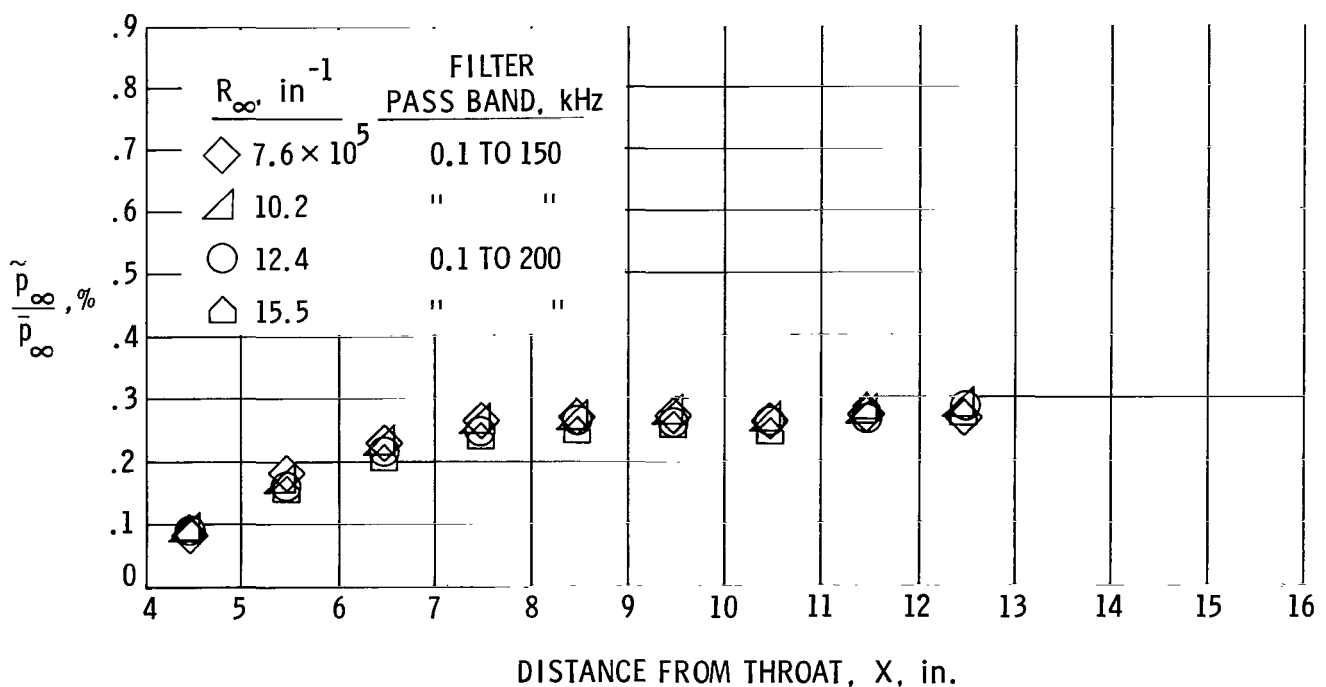


(b) $R_\infty \approx 8.1$ to 15.8×10^5 per inch; bleed valve open.

Figure 7.- Variation of normalized rms static pressure with X at $Y = 0$ and $Z = -4$ in. Small symbols are for data derived from mode plots.

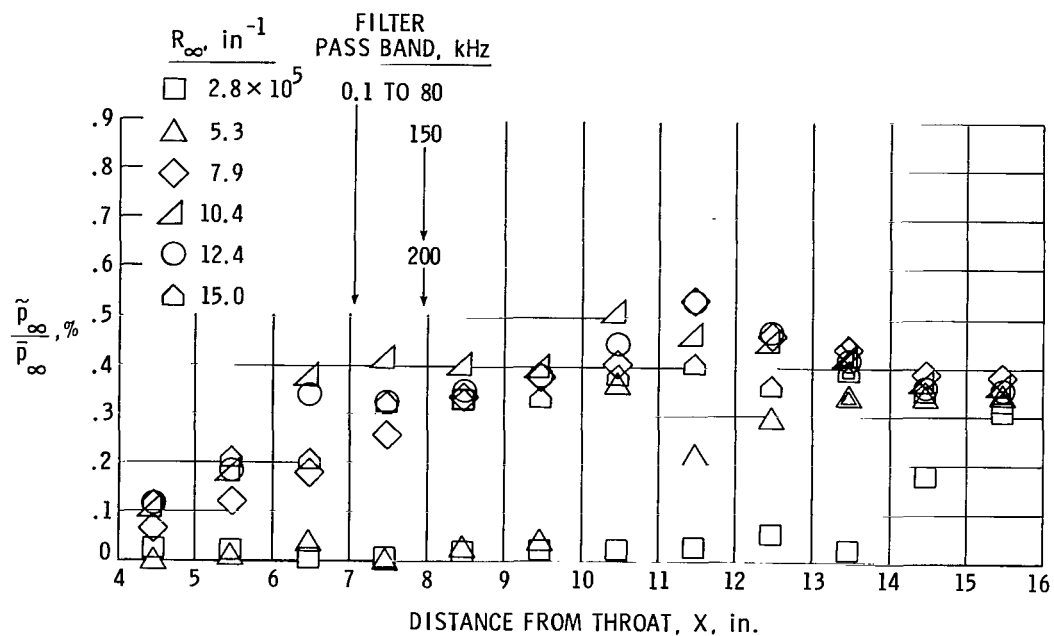


(c) $R_\infty \approx 2.3$ and 5.3×10^5 per inch; bleed valve closed.

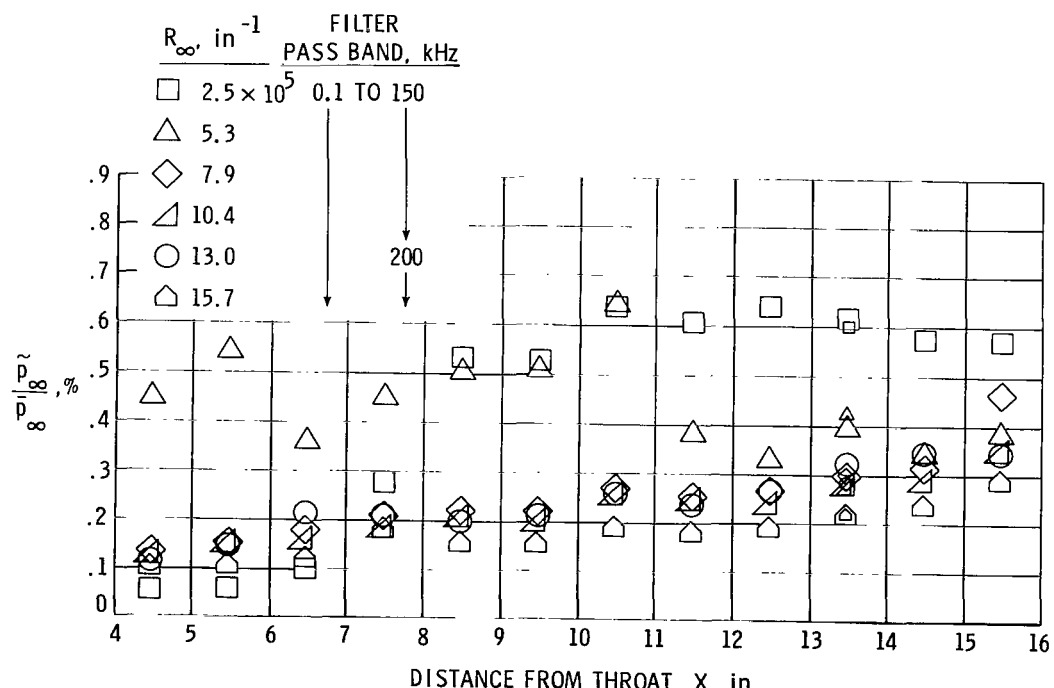


(d) $R_\infty \approx 7.6$ to 15.5×10^5 per inch; bleed valve closed.

Figure 7.- Concluded.

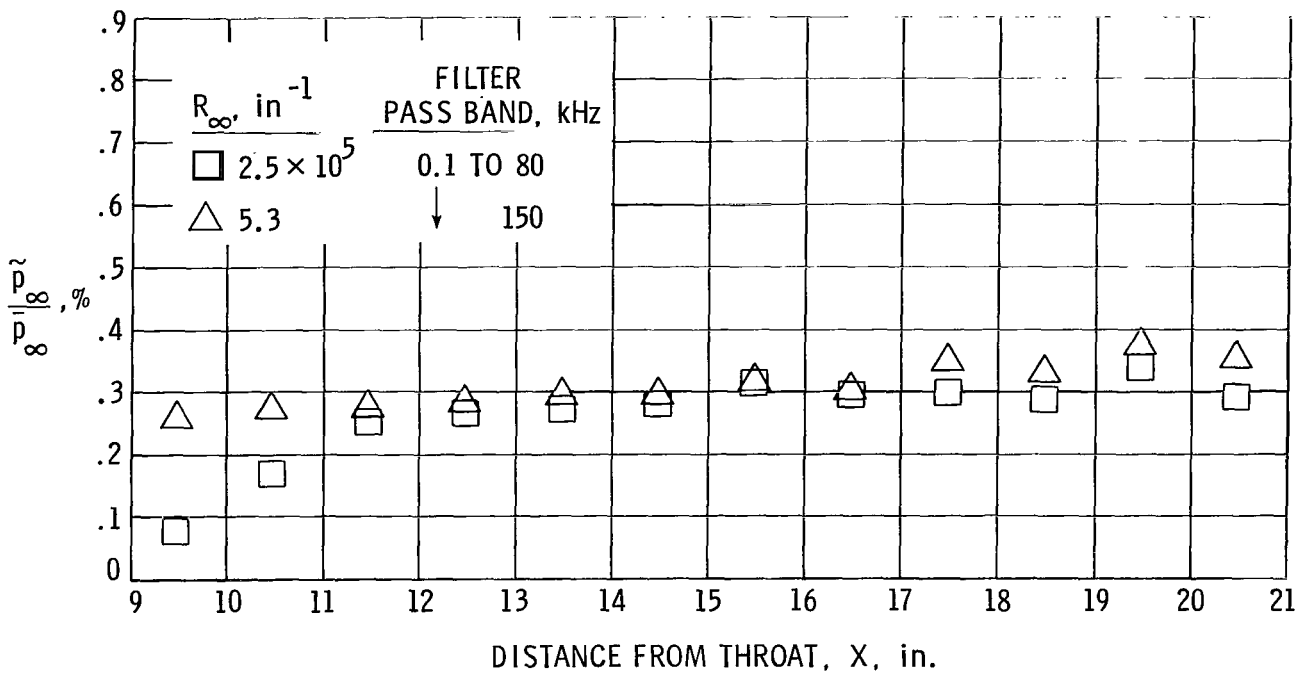


(a) $R_{\infty} \approx 2.8 \text{ to } 15.0 \times 10^5$ per inch; bleed valve open.

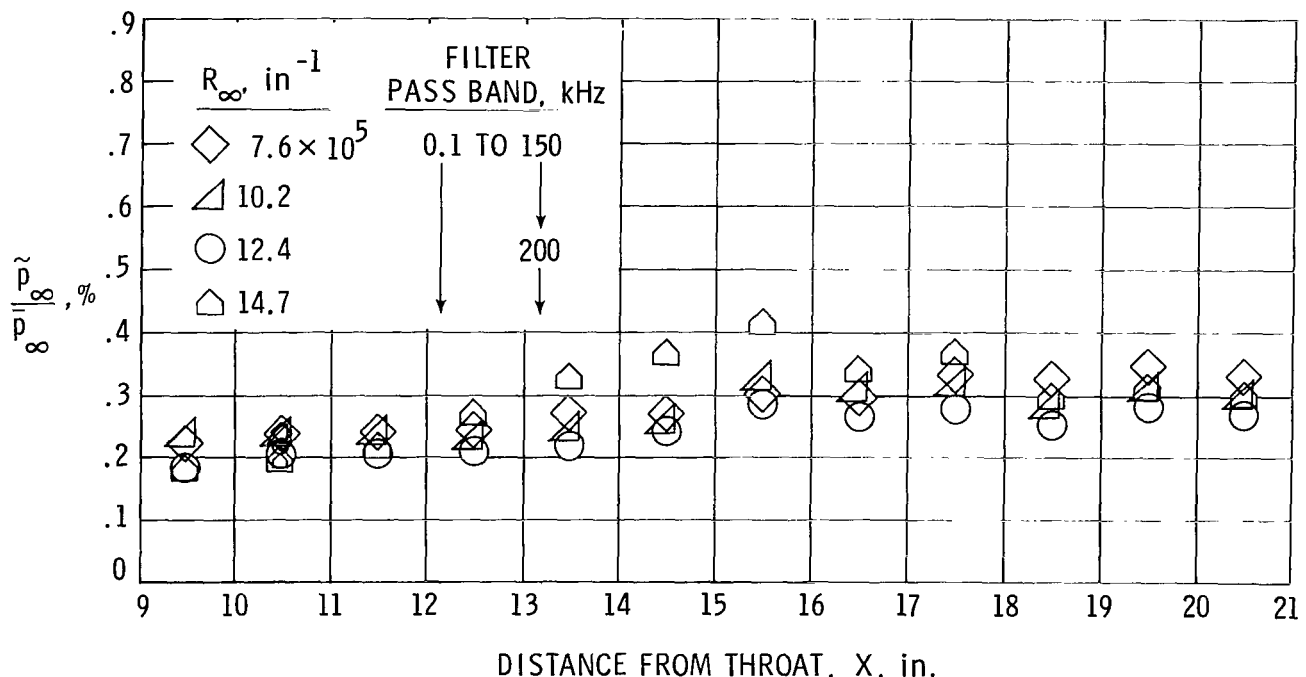


(b) $R_{\infty} \approx 2.5 \text{ to } 15.7 \times 10^5$ per inch; bleed valve closed.

Figure 8.- Variation of normalized rms static pressure with X at $Y = -0.5$ in. and $Z = 0$. Small symbols are for data derived from mode plots.

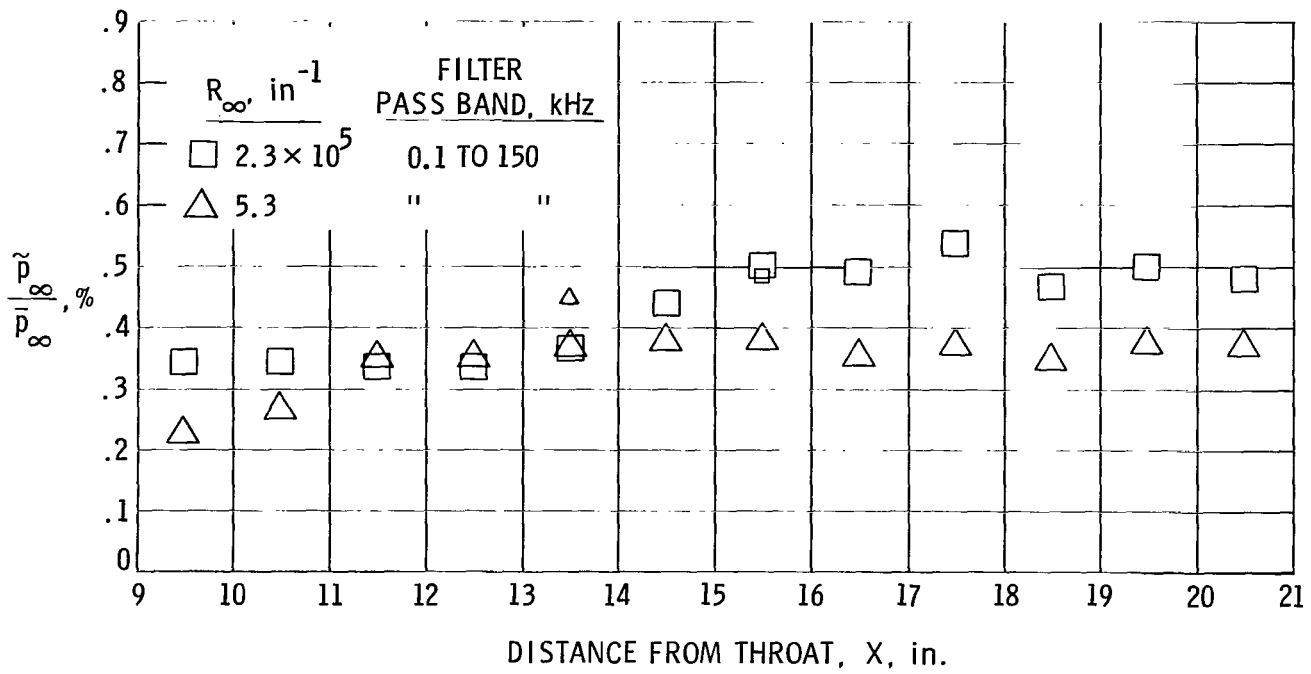


(a) $R_\infty \approx 2.5$ and 5.3×10^5 per inch; bleed valve open.

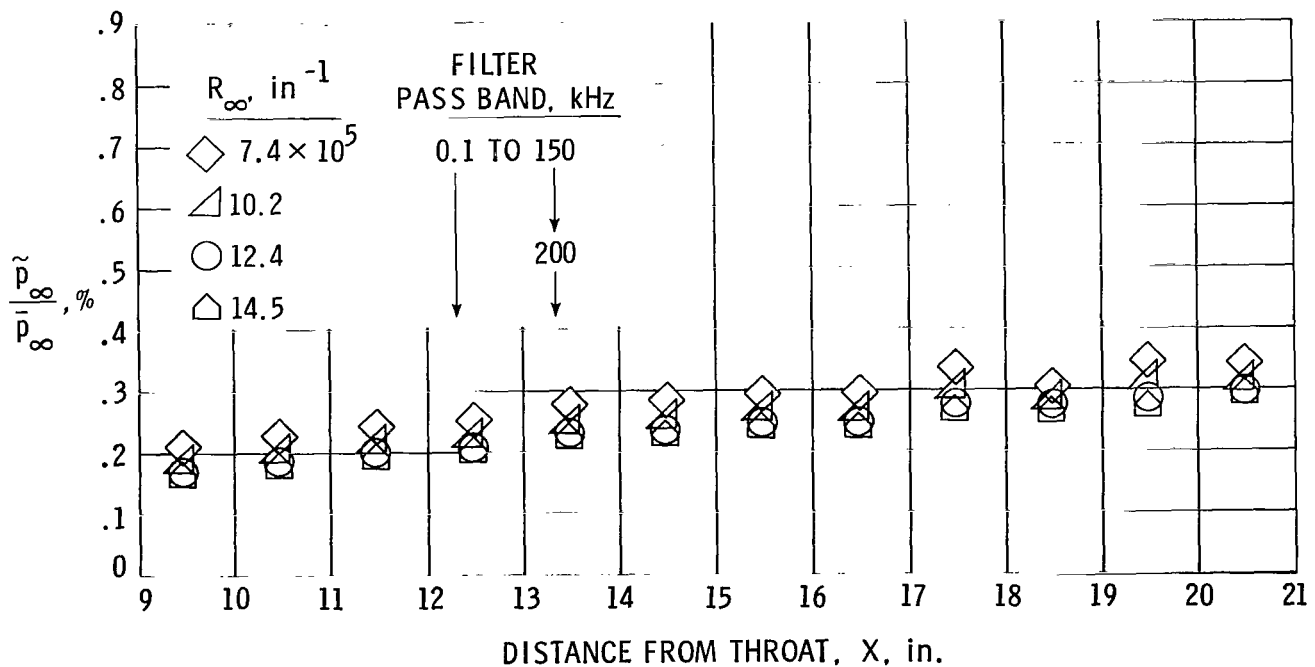


(b) $R_\infty \approx 7.6$ to 14.7×10^5 per inch; bleed valve open.

Figure 9.- Variation of normalized rms static pressure with X at $Y = 1.5$ in. and $Z = 0$. Small symbols are for data derived from mode plots.

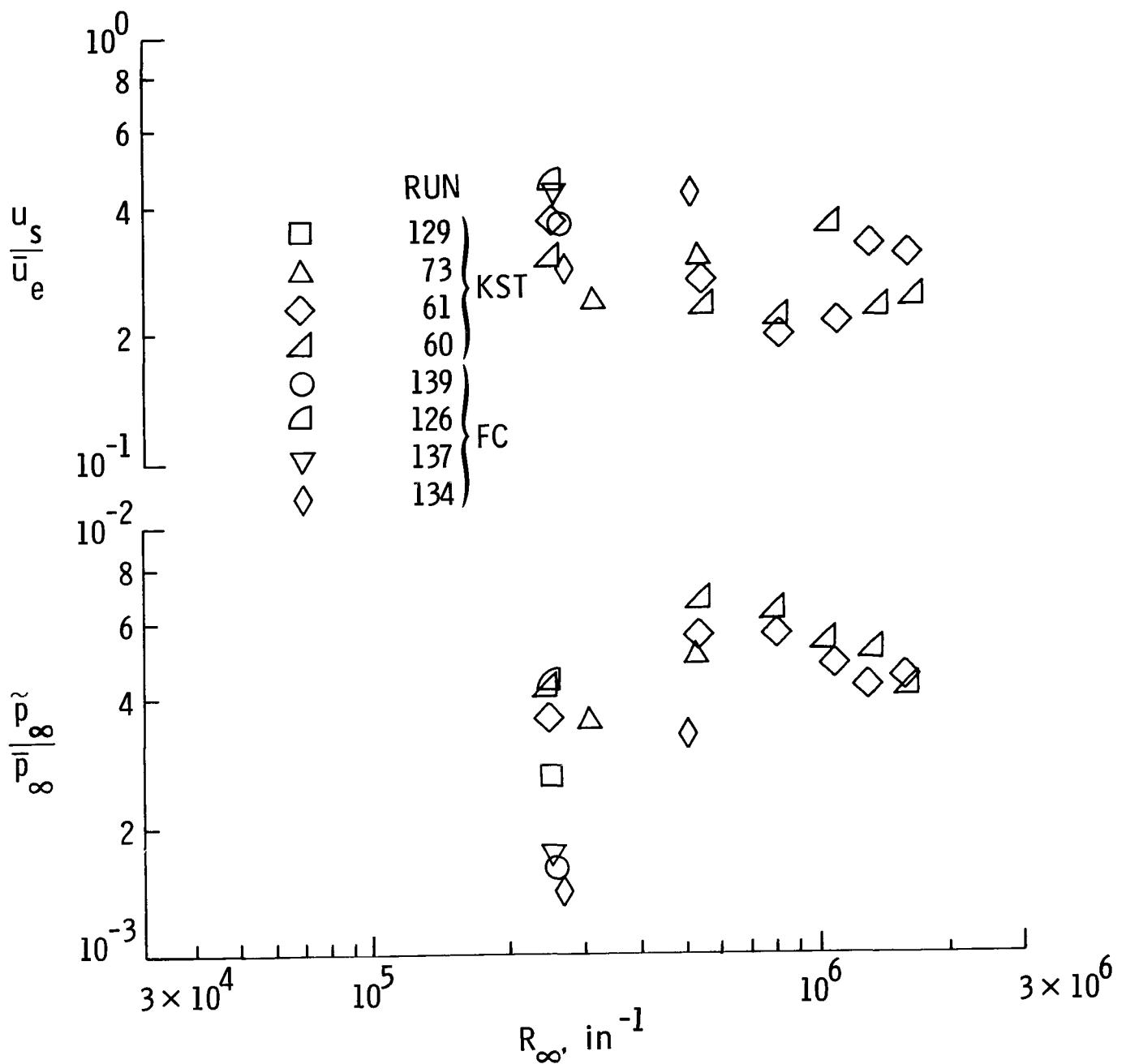


(c) $R_\infty \approx 2.3$ and 5.3×10^5 per inch; bleed valve closed.



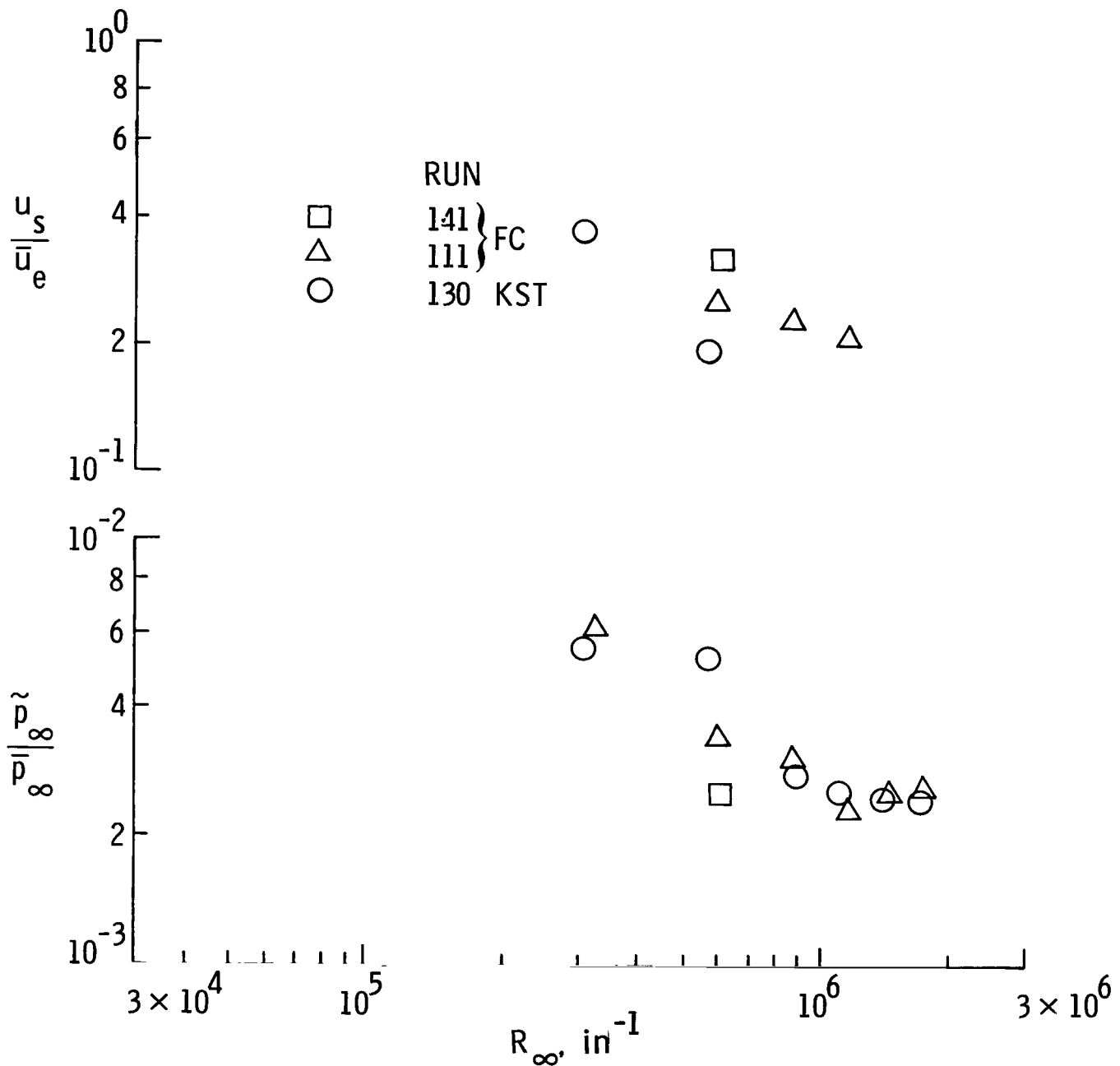
(d) $R_\infty \approx 7.4$ to 14.5×10^5 per inch; bleed valve closed.

Figure 9.- Concluded.



(a) Bleed valve open; $X = 15.5$ in.; $Y = 0$; $Z = 0$.

Figure 10.- Variation of normalized source velocity and rms pressure fluctuations with unit Reynolds number from mode-plot data on the centerline.



(b) Bleed valve closed; $x = 13.5$ in.; $y = 0$; $z = 0$.

Figure 10.- Concluded.

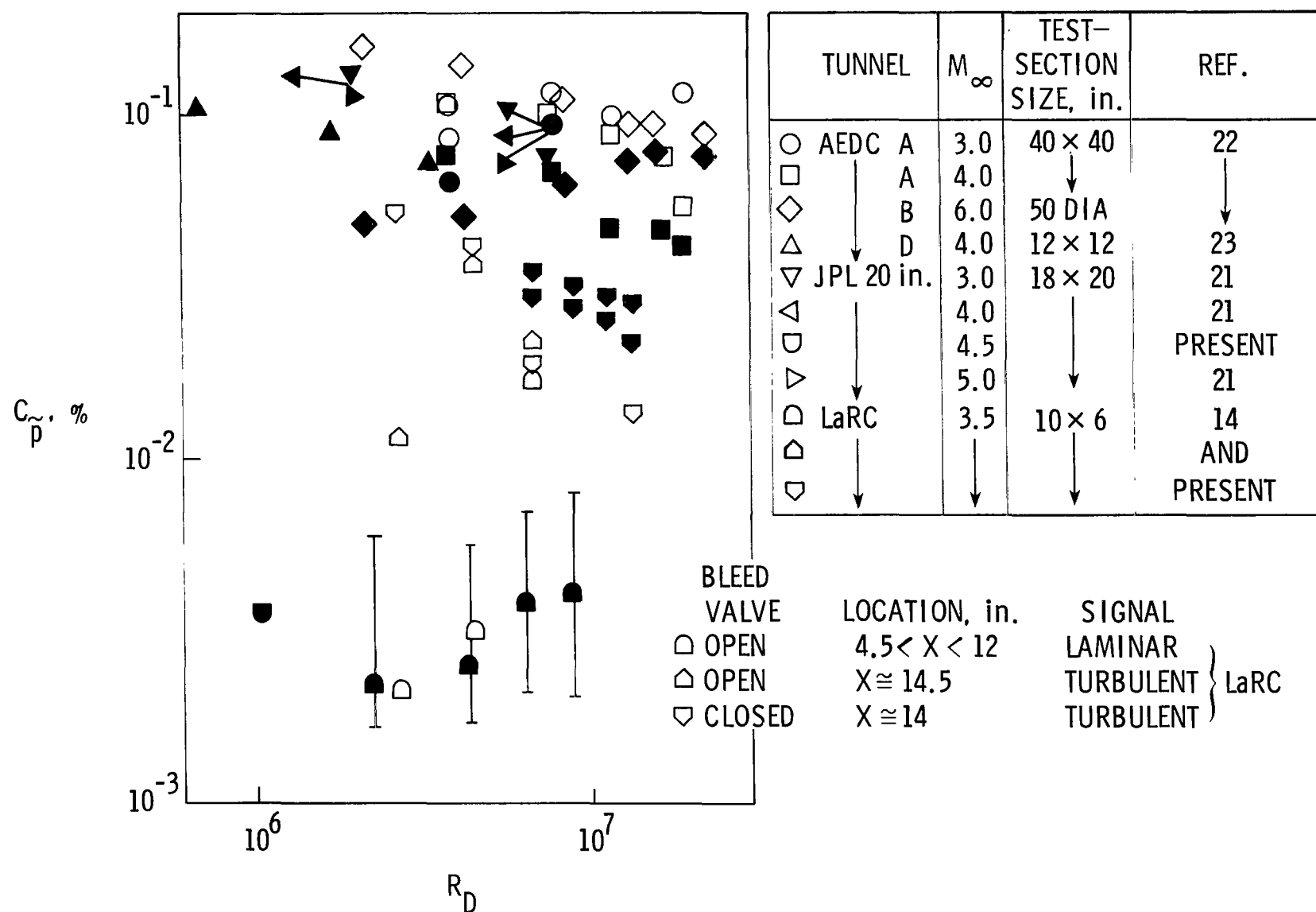
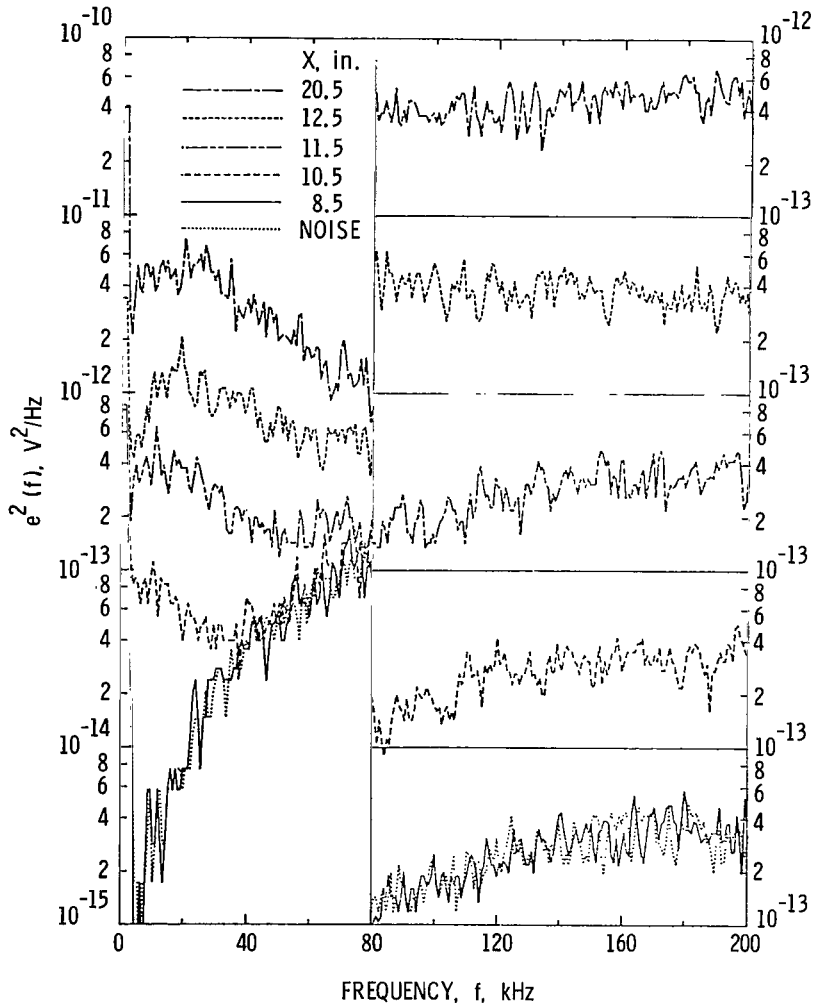
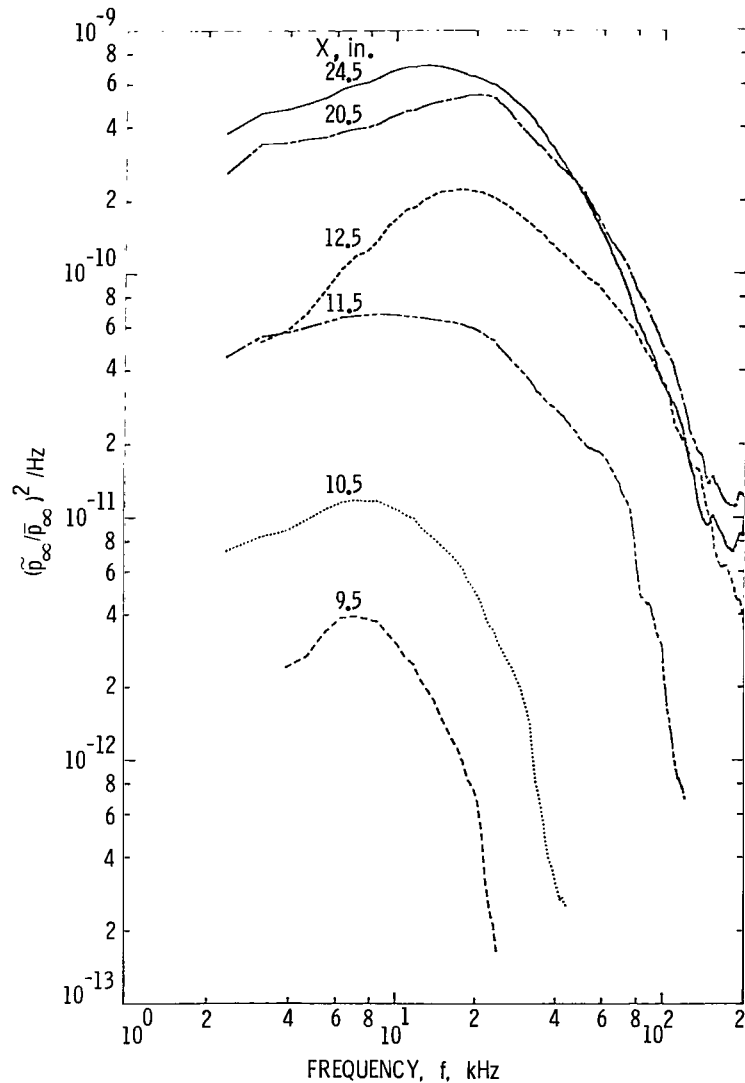


Figure 11.- Comparison of rms pressure coefficients in Mach 3.5 nozzle (pilot low-disturbance tunnel at the Langley Research Center) with those in conventional wind tunnels. Open symbols indicate pitot pressure transducers, and solid symbols indicate hot-wire data.

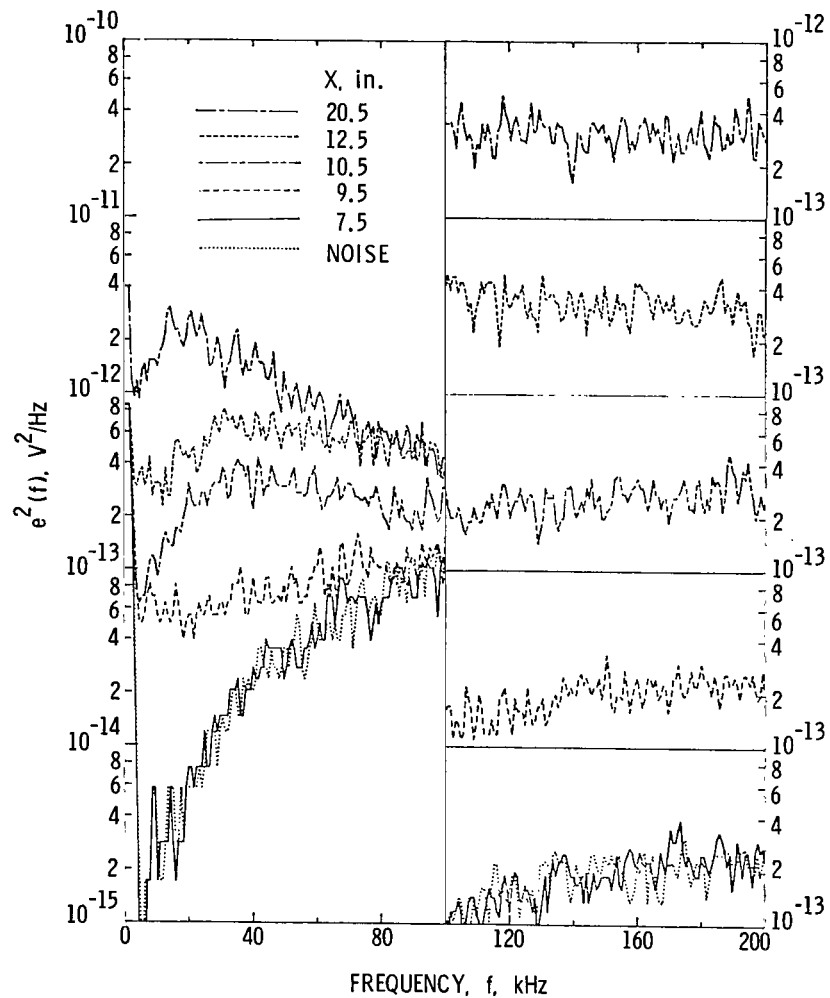


(a) Spectra of total signal and instrument noise.

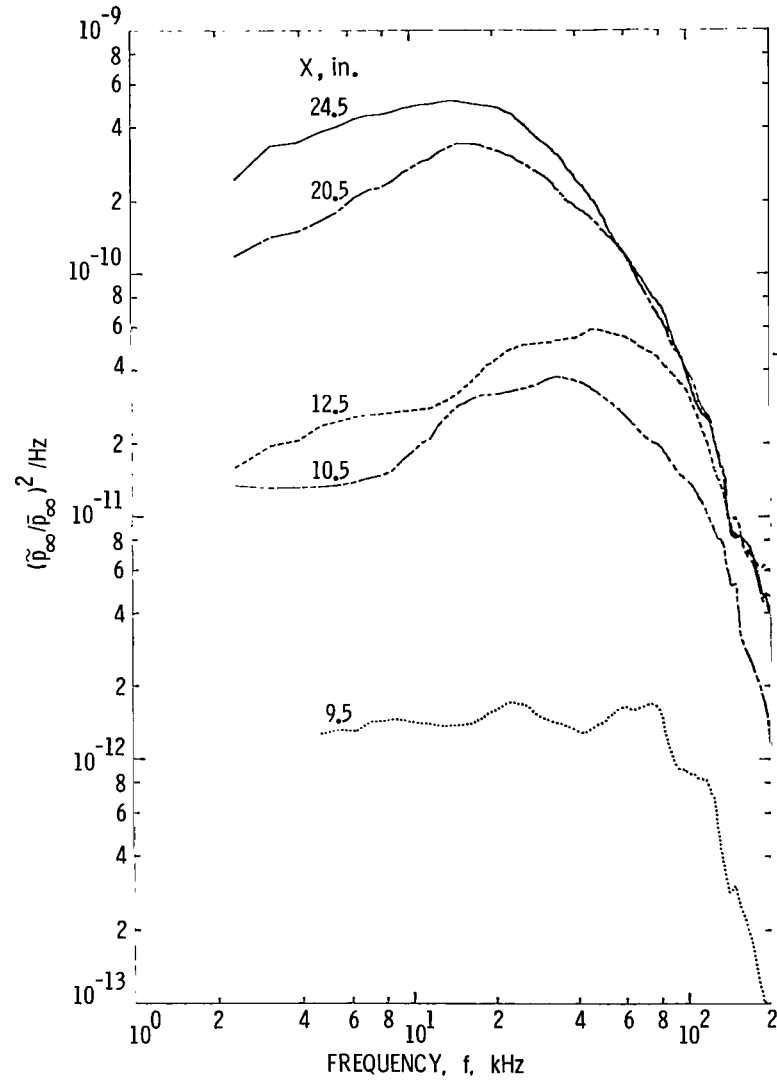


(b) Smoothed spectra with instrument noise removed.

Figure 12.- Hot-wire power spectra at various locations of X on centerline ($Y = 0$, $Z = 0$) for $R_\infty \approx 5.3 \times 10^5$ per inch with bleed valve open.

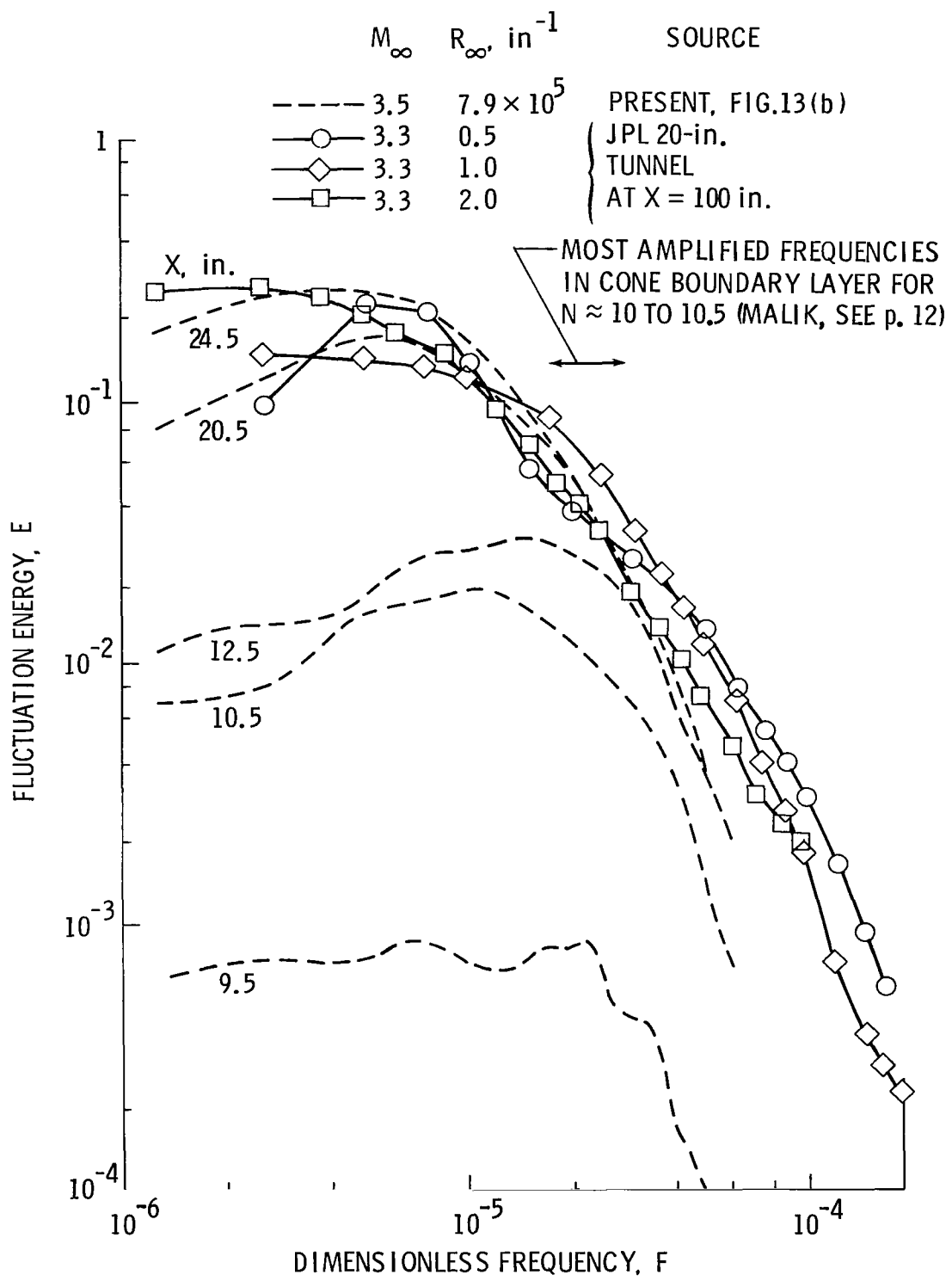


(a) Spectra of total signal and instrument noise.



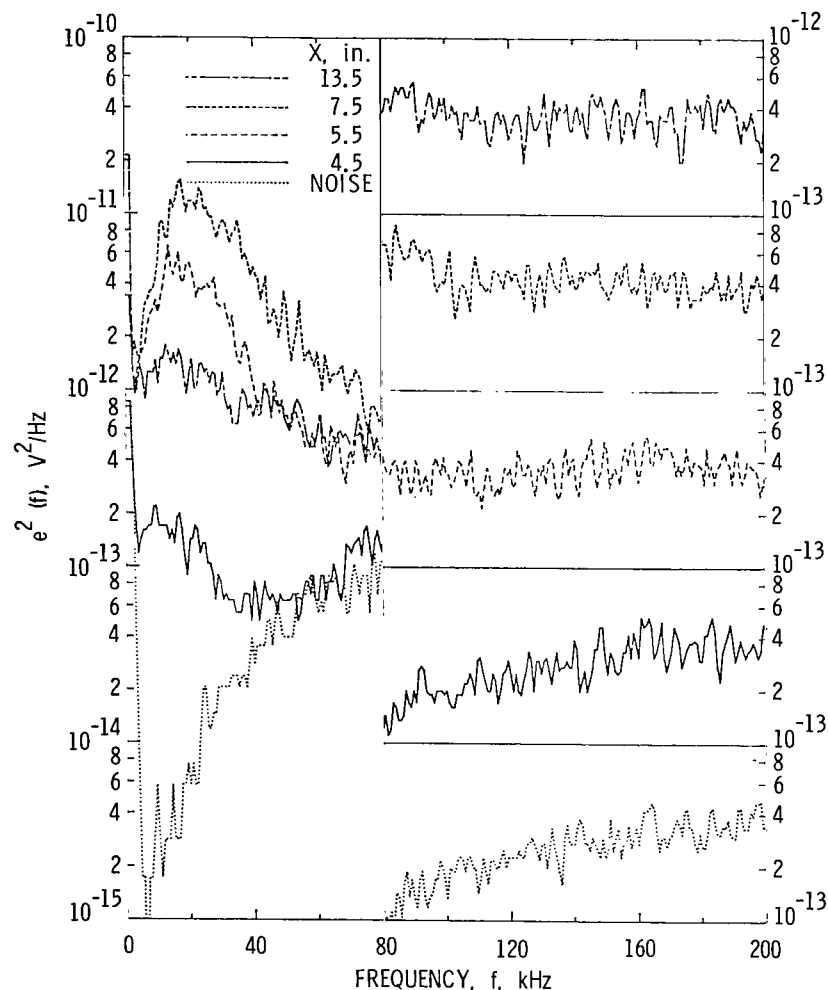
(b) Smoothed spectra with instrument noise removed.

Figure 13.- Spectra at several locations along centerline for $R_\infty \approx 7.9 \times 10^5$ per inch with bleed valve open.

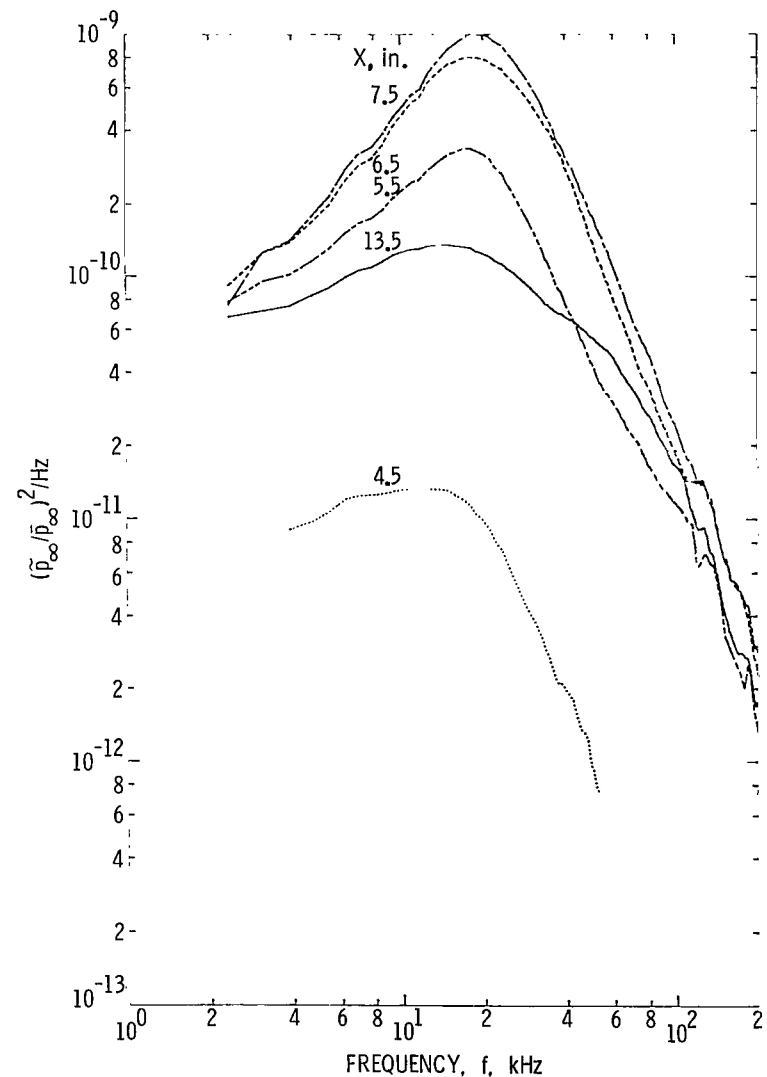


(c) Comparisons of normalized spectra.

Figure 13.- Concluded.

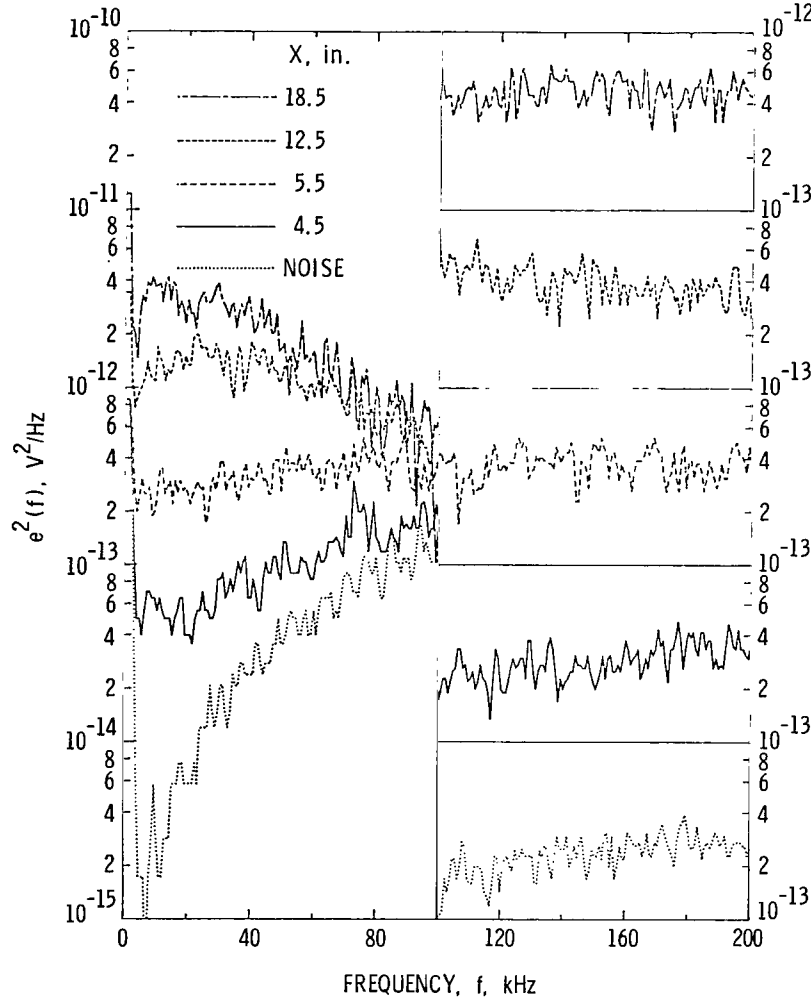


(a) Spectra of total signal and instrument noise.

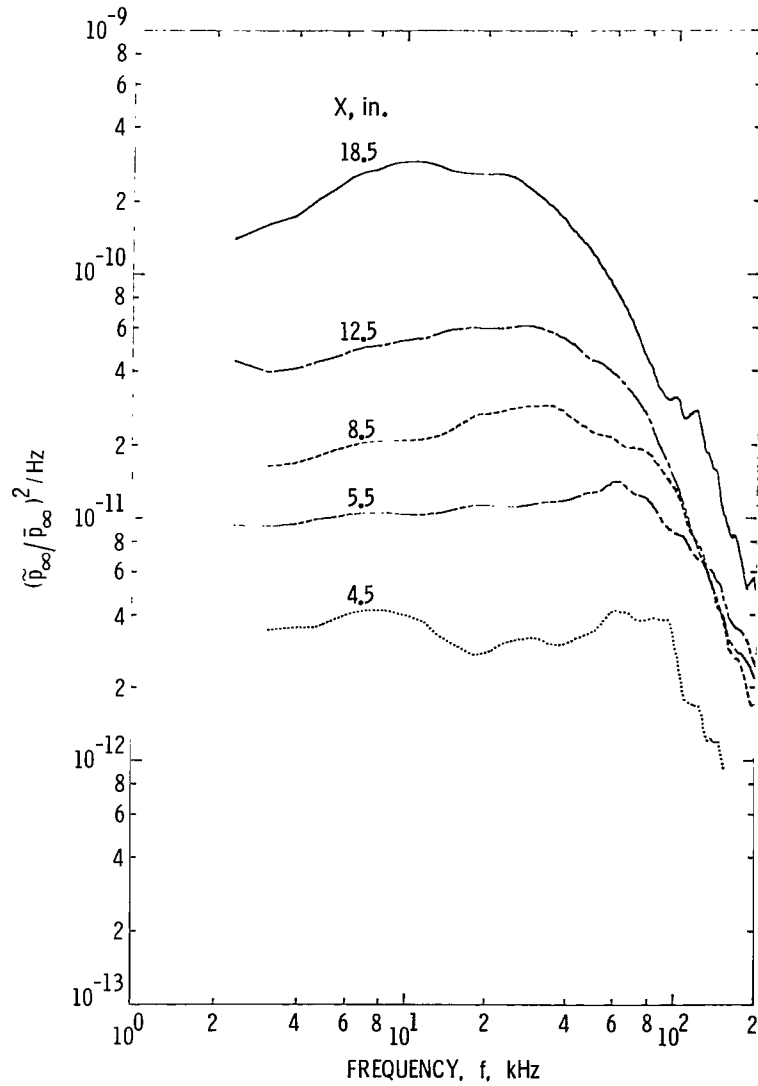


(b) Smoothed spectra with instrument noise removed.

Figure 14.- Spectra at several locations along centerline for $R_\infty \approx 5.3 \times 10^5$ per inch with bleed valve closed.



(a) Spectra of total signal and instrument noise.

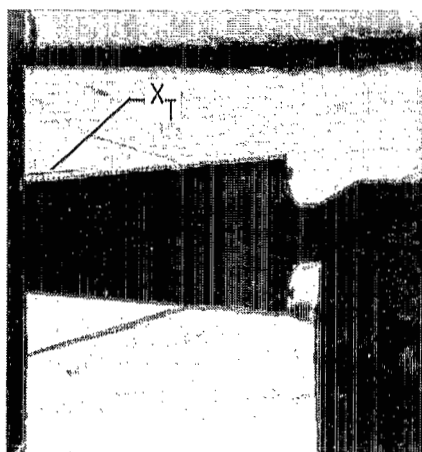


(b) Smoothed spectra with instrument noise removed.

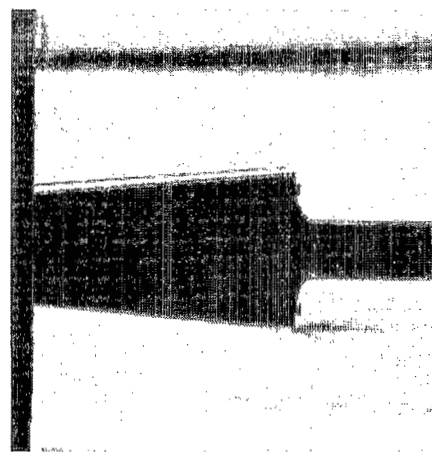
Figure 15.- Spectra at several locations along centerline for $R_\infty \approx 7.9 \times 10^5$ per inch with bleed valve closed.



(a) Cone apex at $X = 5$ in. from nozzle
throat; $R_\infty \approx 5.0 \times 10^5$ per inch.



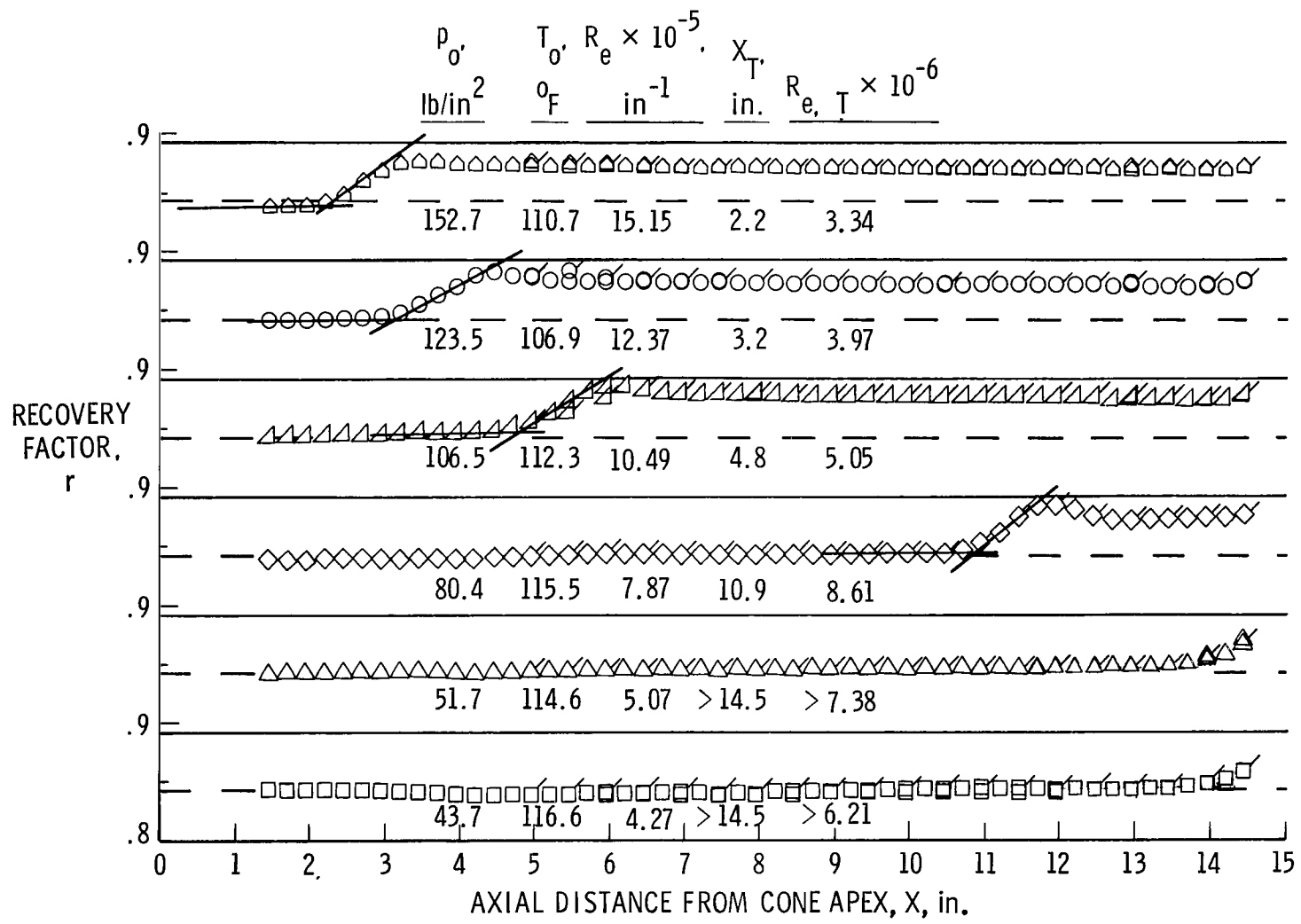
(b) Cone apex at $X = 8$ in. from nozzle
throat; $R_\infty \approx 5.0 \times 10^5$ per inch.



(c) Cone apex at $X = 8$ in. from nozzle
throat; $R_\infty \approx 3.8 \times 10^5$ per inch.

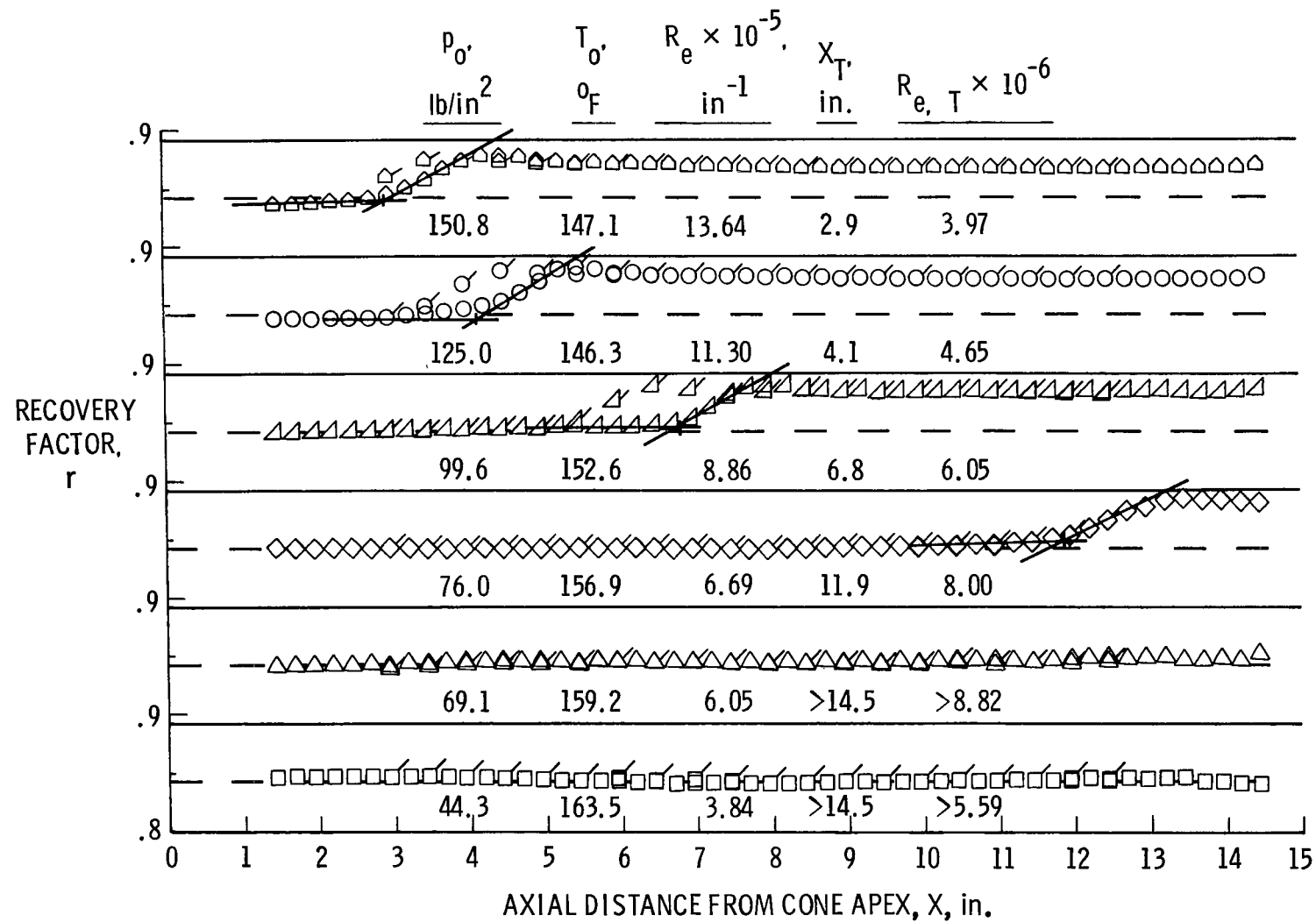
L-83-100

Figure 16.- Schlieren photographs showing downstream regions of flow on the cone
at two test locations in the nozzle with bleed valve open.



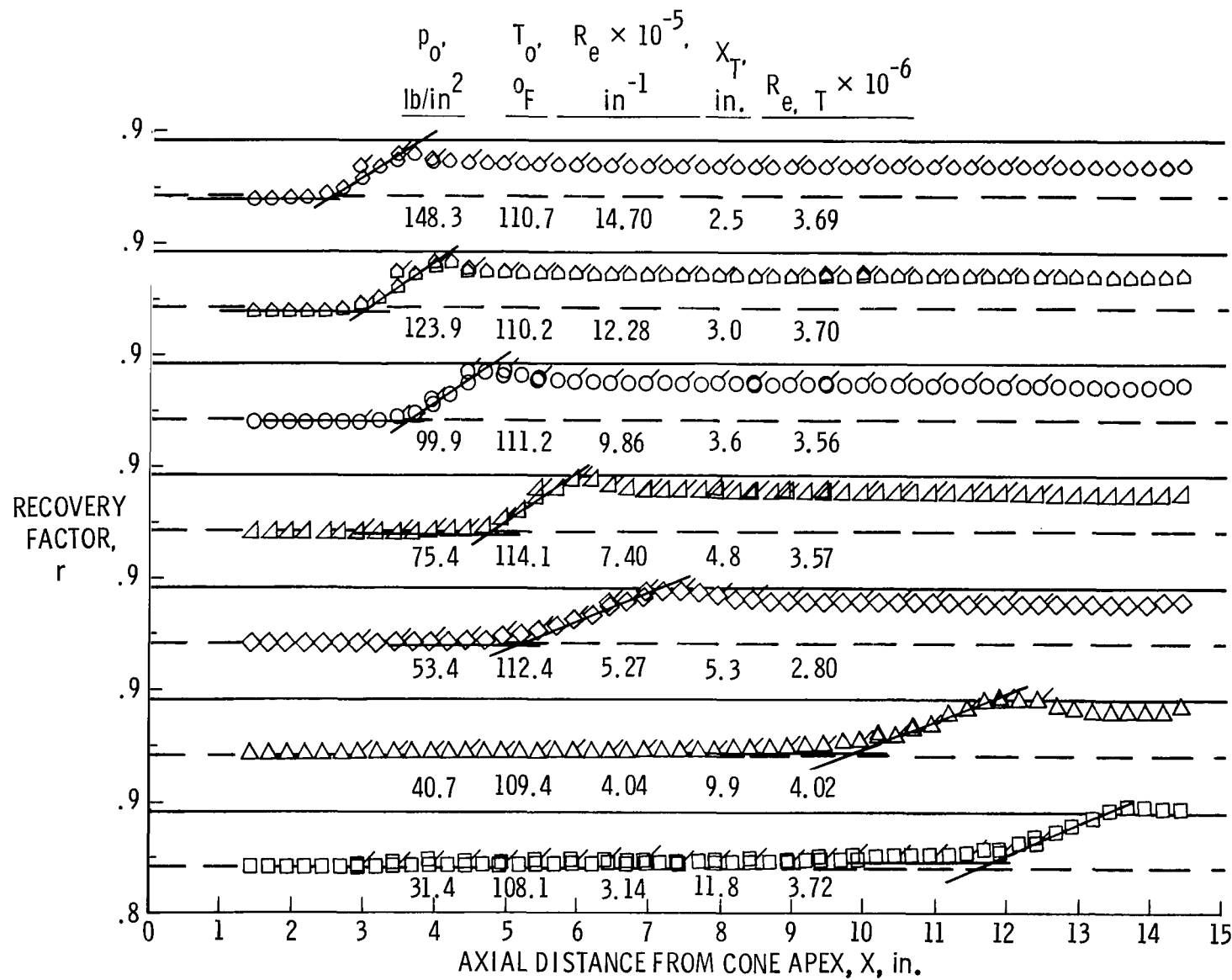
(a) Run 38; bleed valve open; main thermocouple row 2 at $\phi = 0^\circ$.

Figure 17.- Typical variations of measured recovery factor along cone with apex at 5 in. from throat. Flagged symbols are for data on opposite side of cone from main row.



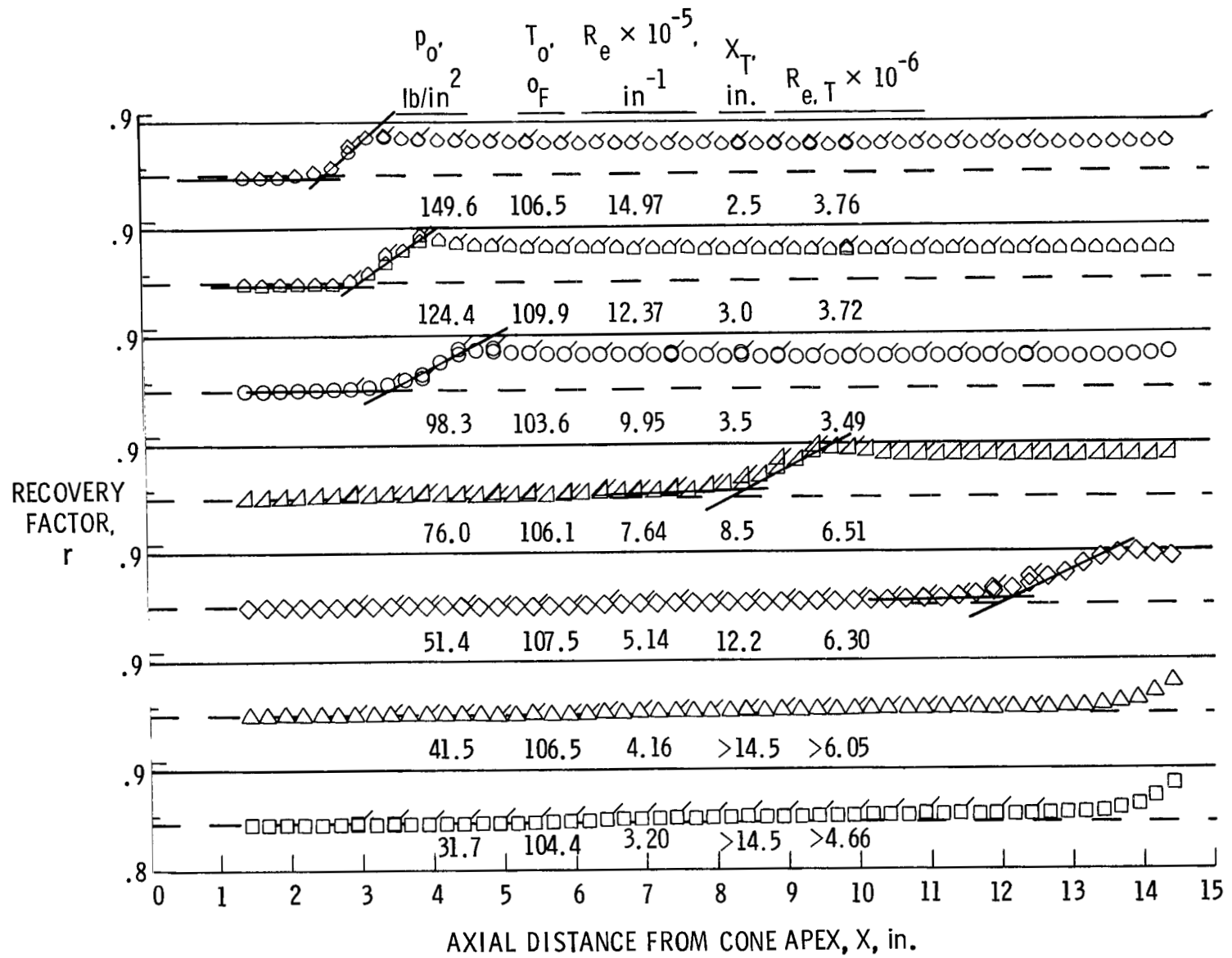
(b) Run 41; bleed valve open; main thermocouple row 1 at $\phi = 270^\circ$.

Figure 17.- Continued.



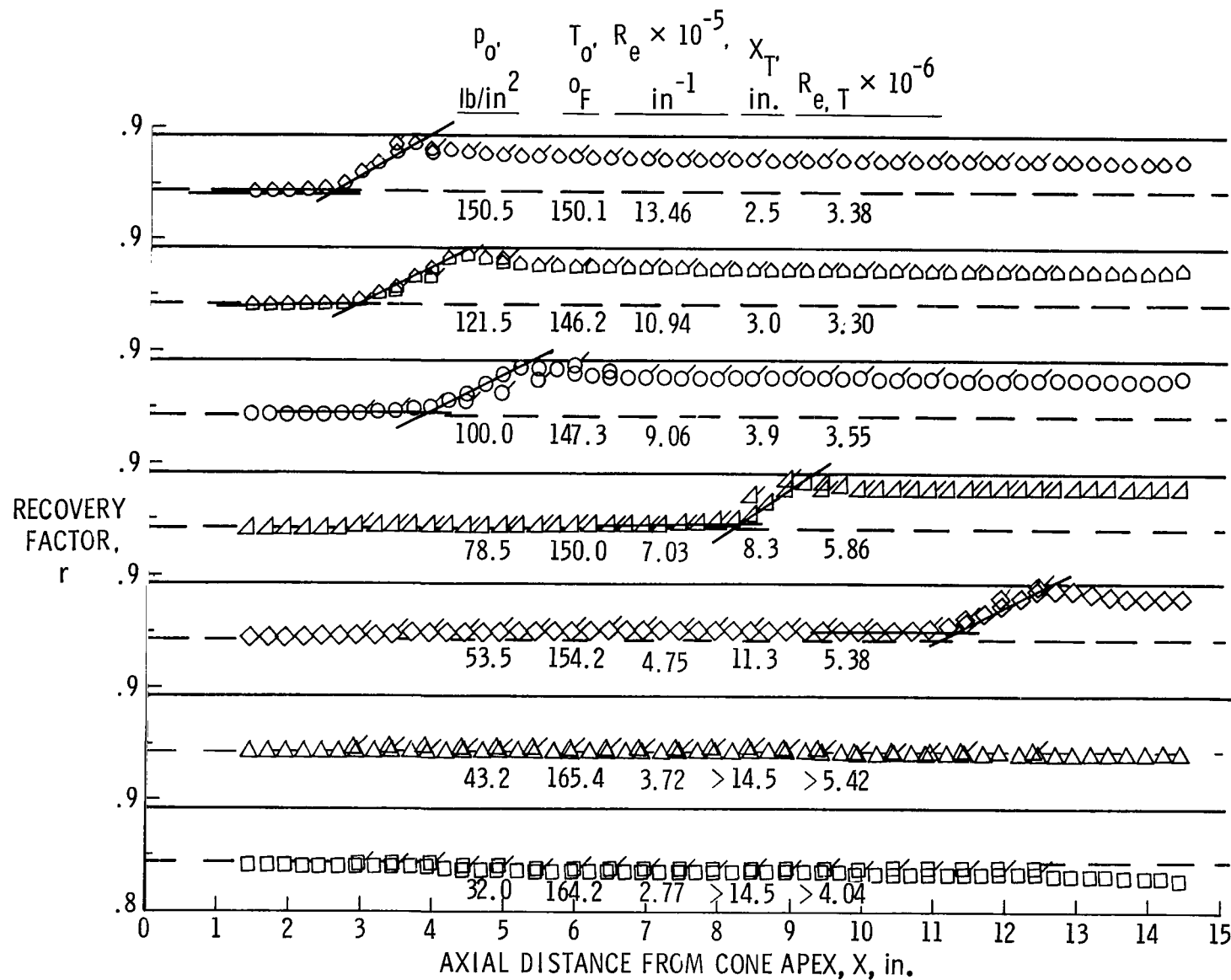
(c) Run 53; bleed valve closed; main thermocouple row 1 at $\phi = 180^\circ$.

Figure 17.- Concluded.



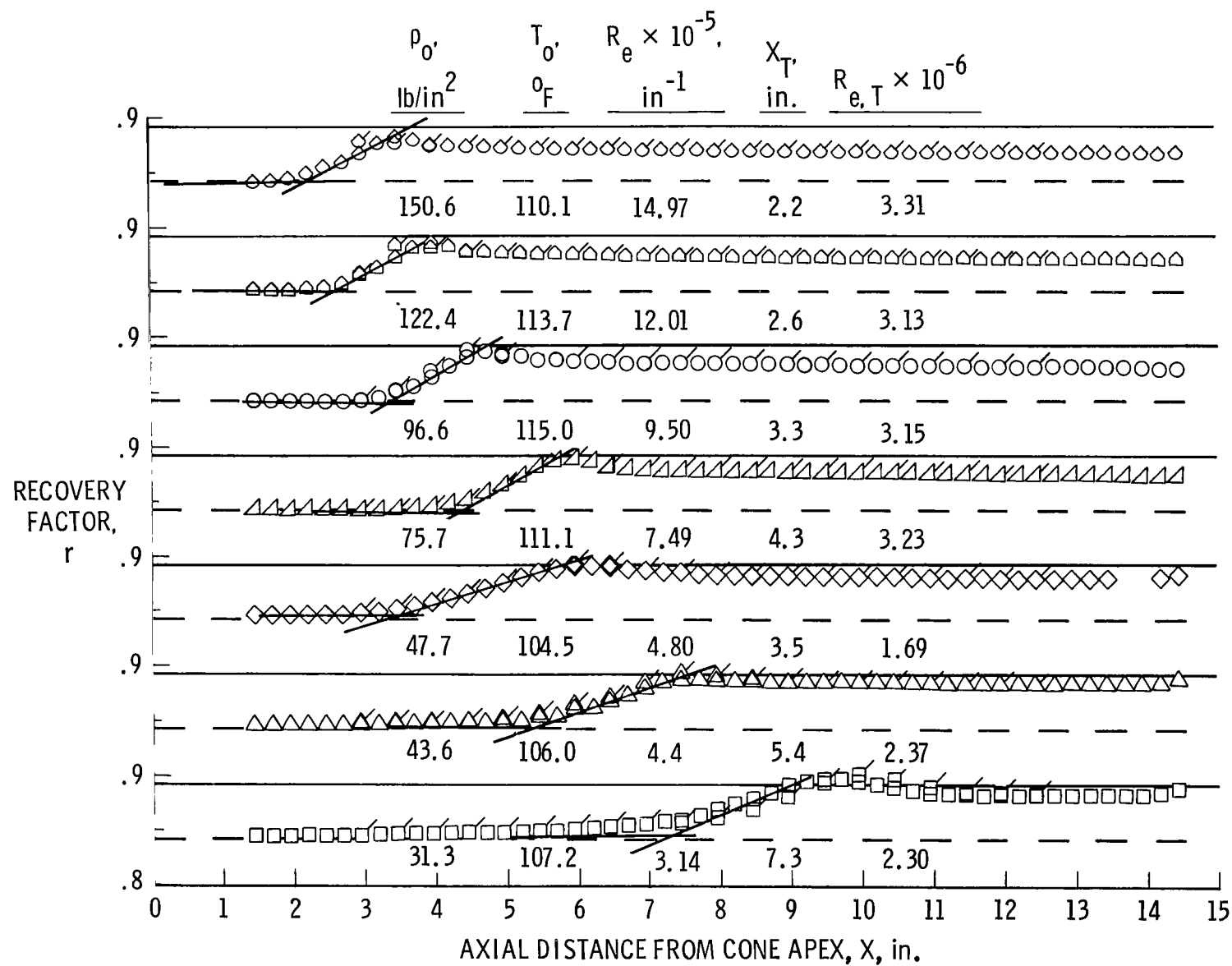
(a) Run 52; bleed valve open; main thermocouple row 1 at $\phi = 270^\circ$.

Figure 18.- Typical variations of measured recovery factor along cone with apex at 8 in. from throat. Flagged symbols are for data on opposite side of cone from main row.



(b) Run 50; bleed valve open; main thermocouple row 1 at $\phi = 180^\circ$.

Figure 18.- Continued.



(c) Run 49; bleed valve closed; main thermocouple row 1 at $\phi = 180^\circ$.

Figure 18.- Concluded.

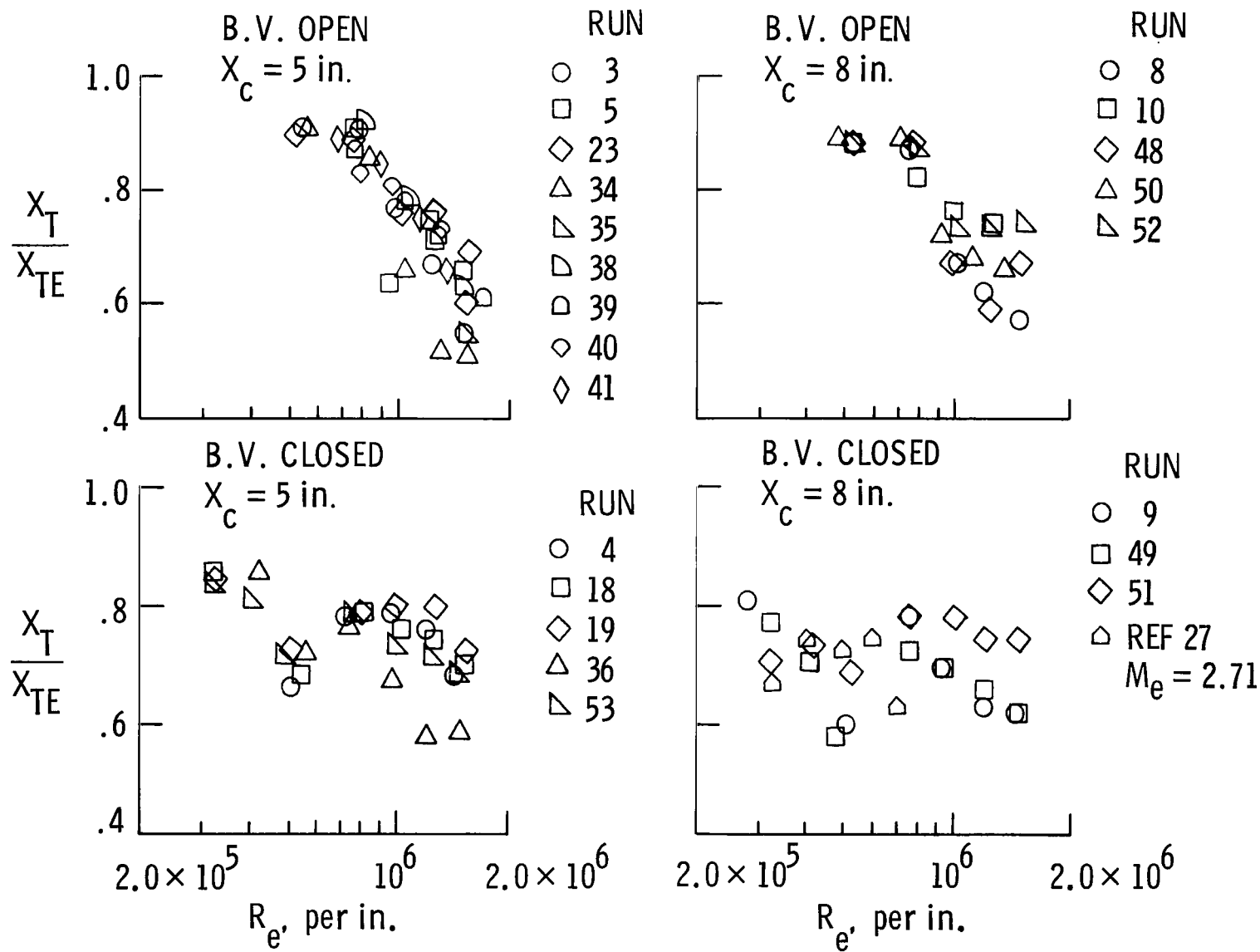


Figure 19.- Variation with local unit Reynolds number of X_T / X_{TE} for bleed valve (B.V.) open and closed and with the cone in two test locations.

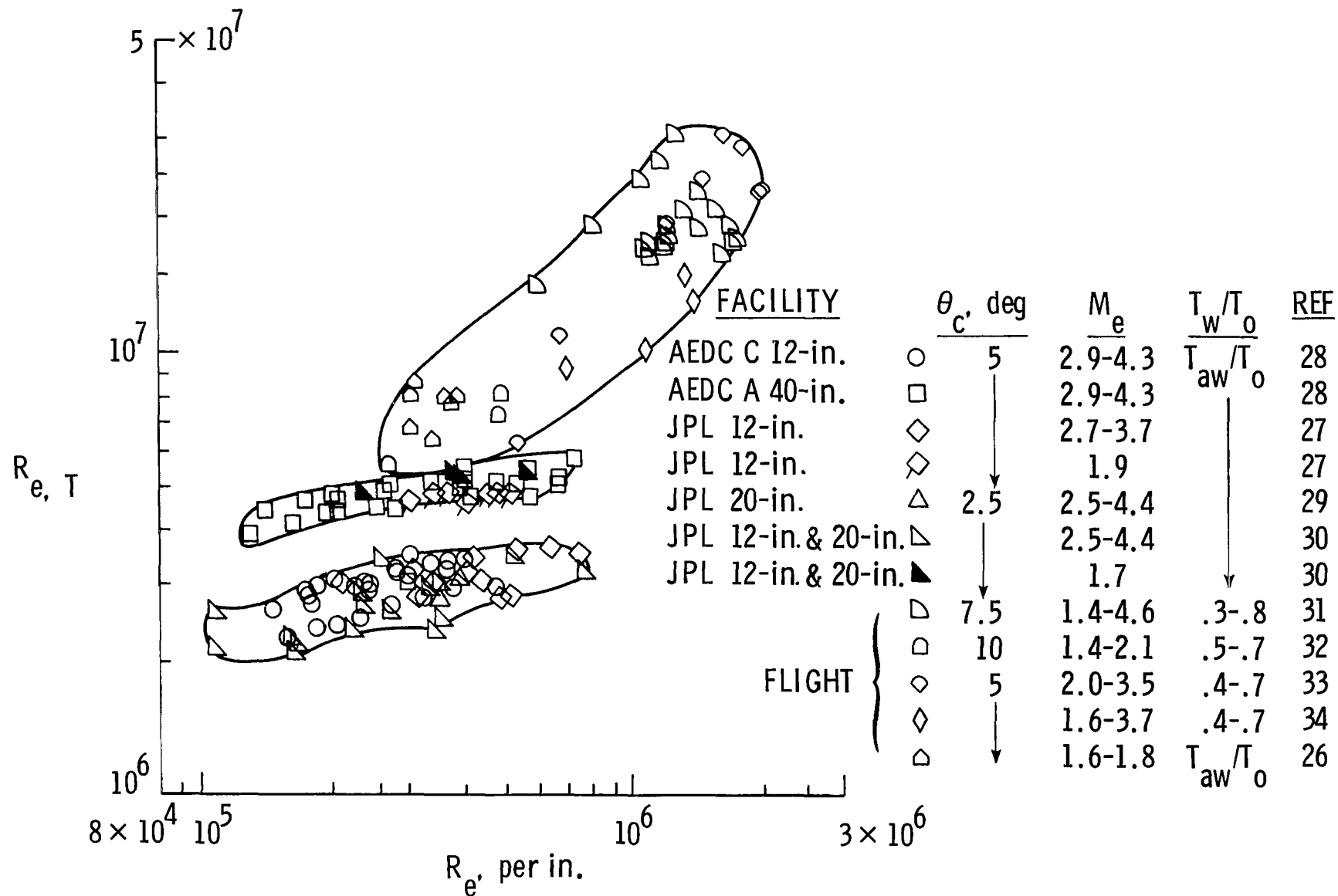
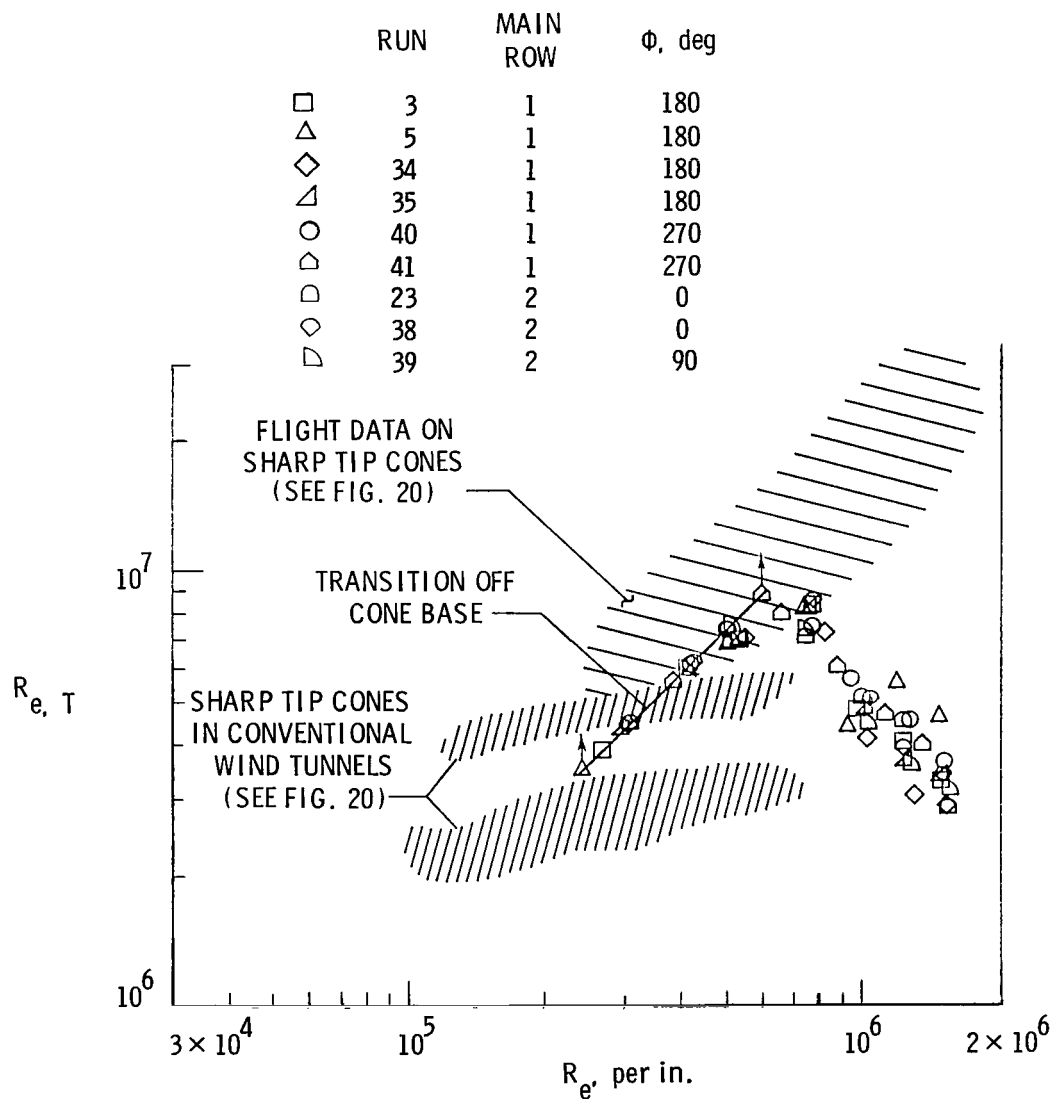
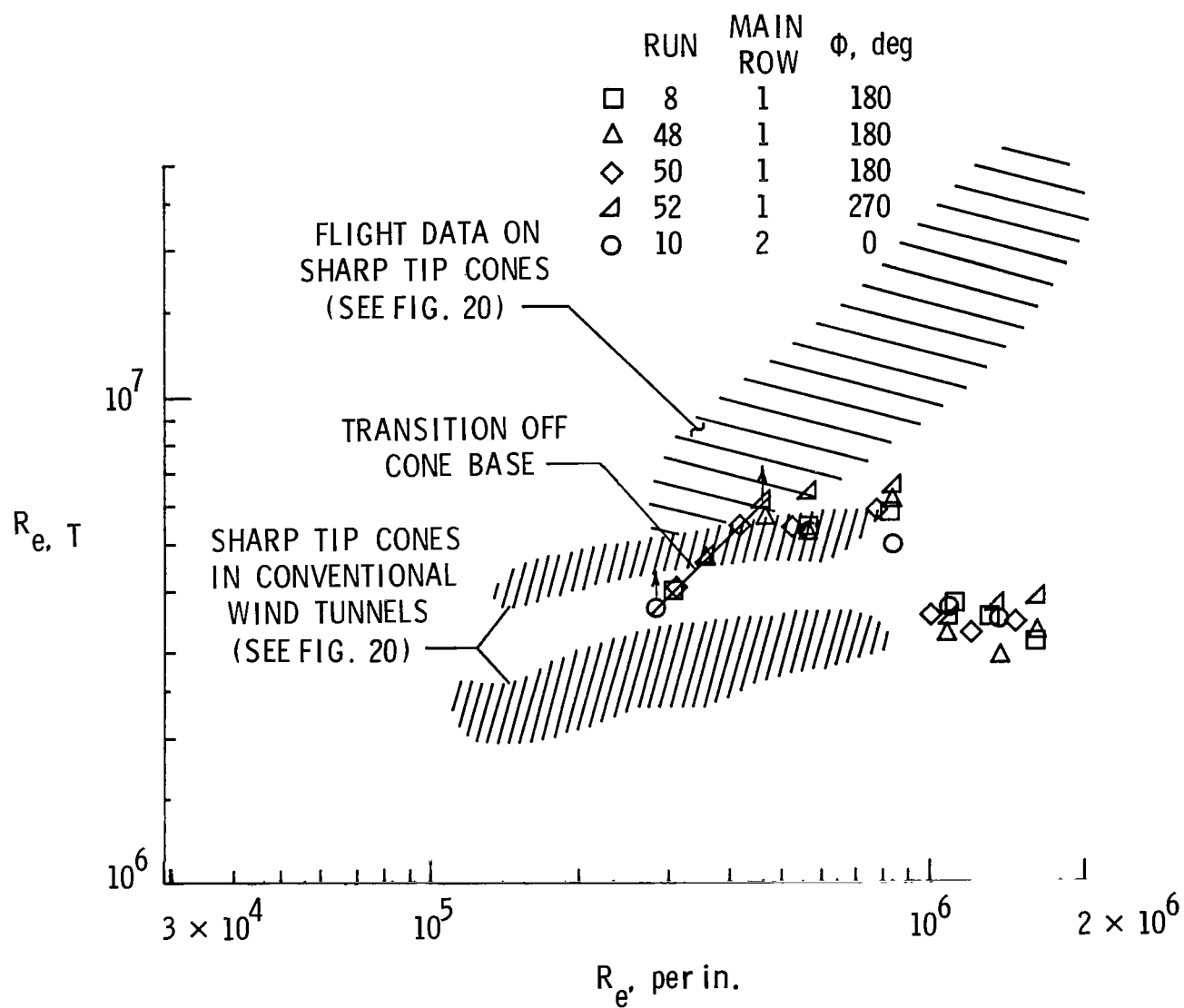


Figure 20.- Variation of local transition Reynolds number with local unit Reynolds number on sharp tip cones at $\alpha = 0$ in conventional wind tunnels and in flight.



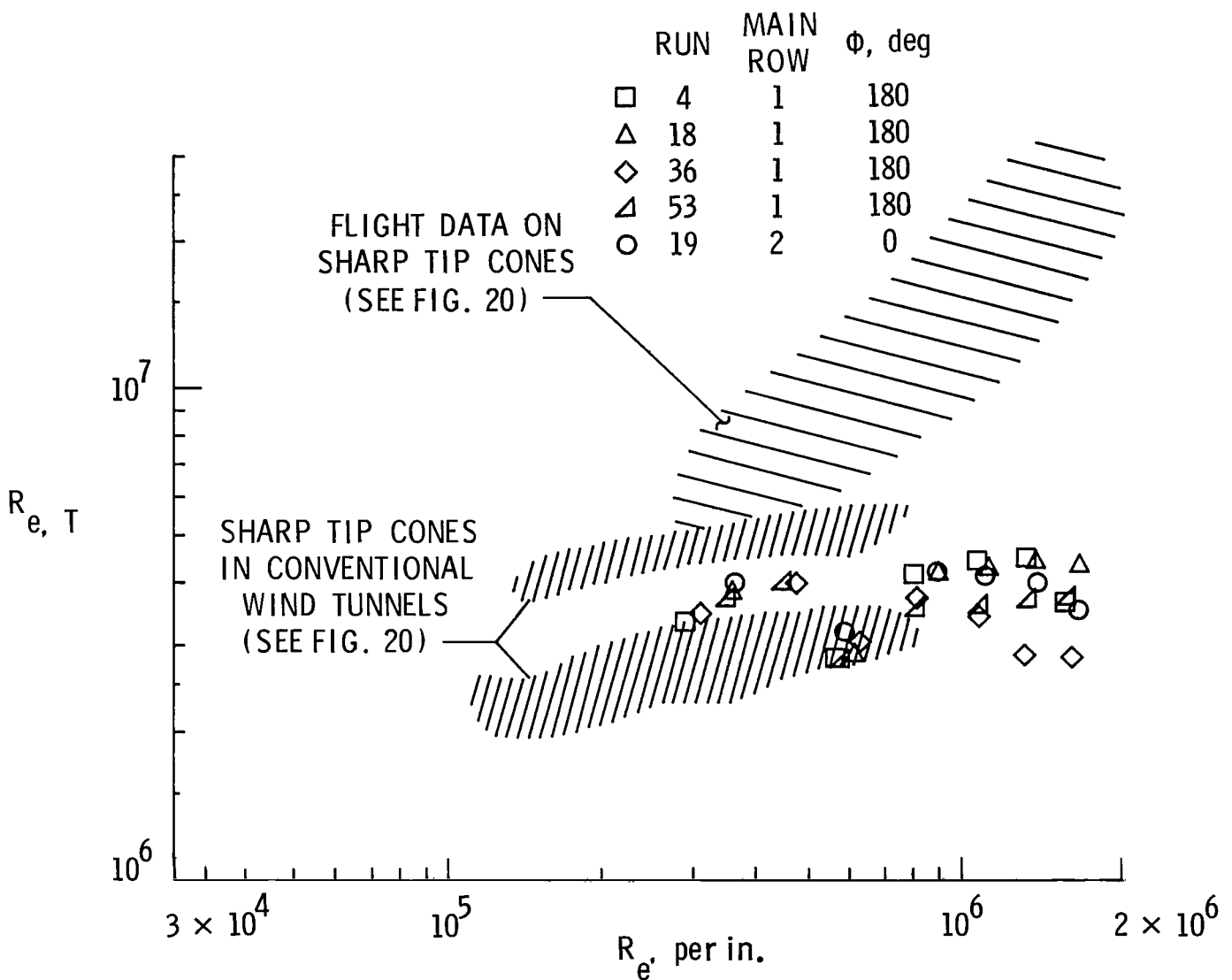
(a) Cone apex at $x = 5$ in. from throat; bleed valve open.

Figure 21.- Comparison of present transition Reynolds numbers with wind tunnel and flight data.



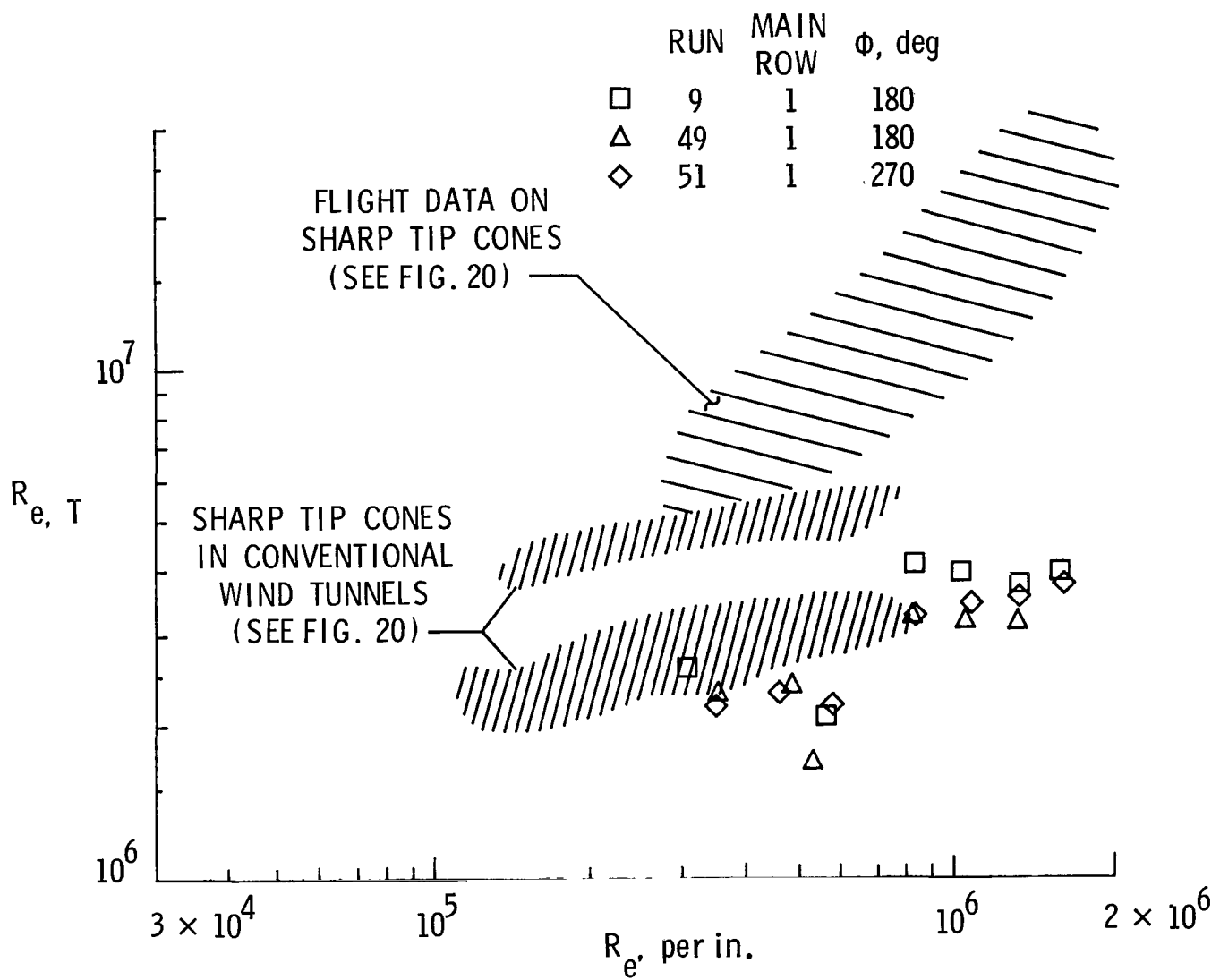
(b) Cone apex at $x = 8$ in. from throat; bleed valve open.

Figure 21.- Continued.



(c) Cone apex at $x = 5$ in. from throat; bleed valve closed.

Figure 21.- Continued.



(d) Cone apex at $x = 8$ in. from throat; bleed valve closed.

Figure 21.- Concluded.

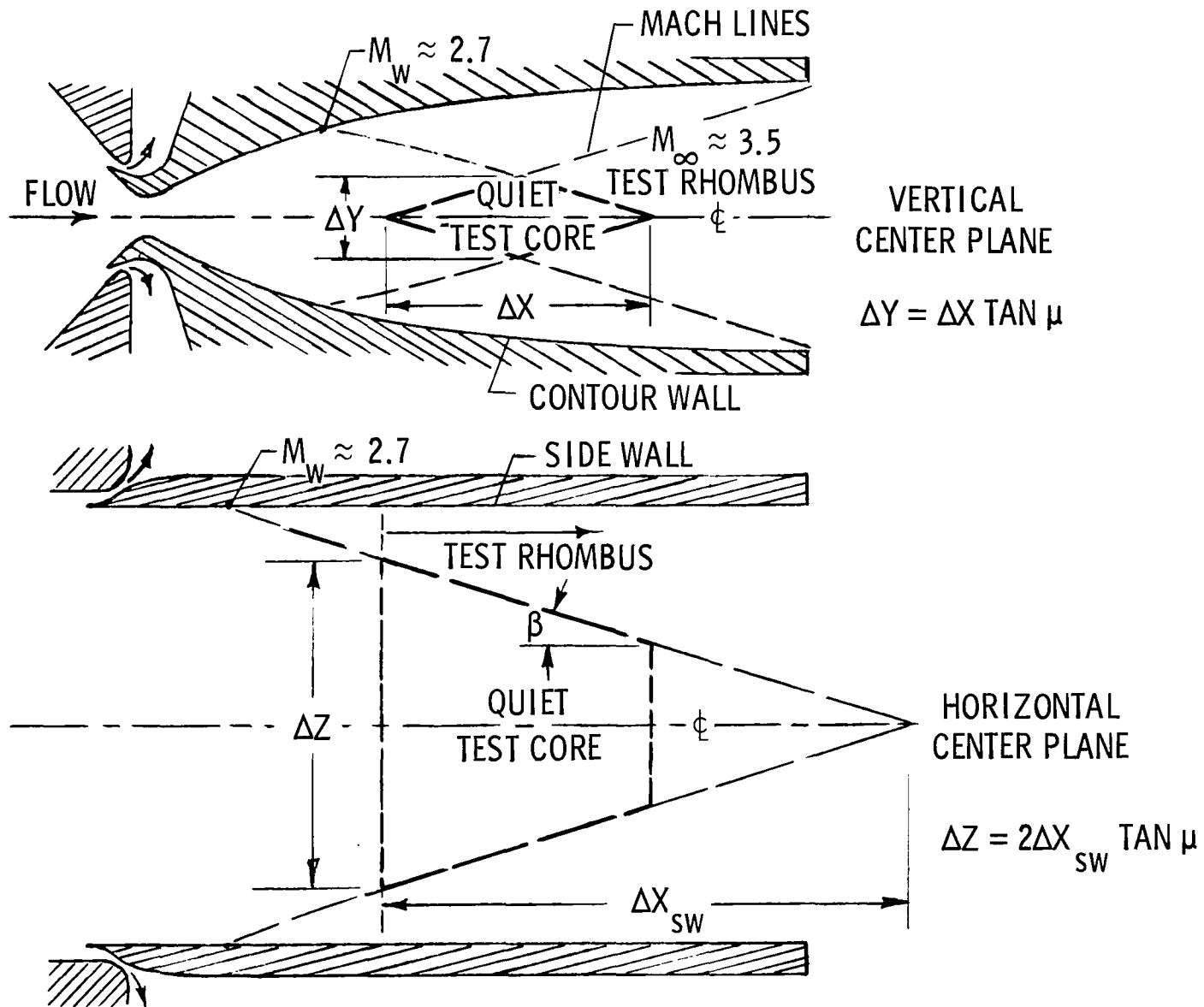


Figure 22.- Shape and location of quiet test core.

1. Report No. NASA TP-2180	2. Government Accession No.	3. Recipient's Catalog No.	
4. Title and Subtitle FREE-STREAM NOISE AND TRANSITION MEASUREMENTS ON A CONE IN A MACH 3.5 PILOT LOW-DISTURBANCE TUNNEL			
7. Author(s) Ivan E. Beckwith, Theodore R. Creel, Jr., Fang-Jeng Chen, and James M. Kendall	5. Report Date September 1983		
9. Performing Organization Name and Address NASA Langley Research Center Hampton, VA 23665	6. Performing Organization Code 505-31-13-06		
12. Sponsoring Agency Name and Address National Aeronautics and Space Administration Washington, DC 20546	8. Performing Organization Report No. L-15610		
15. Supplementary Notes Ivan E. Beckwith and Theodore R. Creel, Jr.: Langley Research Center, Hampton, Virginia. Fang-Jeng Chen: Systems and Applied Sciences Corporation, Hampton, Virginia. James M. Kendall: Jet Propulsion Laboratory, Pasadena, California.	10. Work Unit No.		
16. Abstract A small-scale Mach 3.5 wind tunnel incorporating certain novel design features and intended for boundary-layer-transition research has been tested. The free-stream noise intensities and spectral distributions were determined throughout the test section for several values of unit Reynolds number and for nozzle boundary-layer bleed on and off. The boundary-layer-transition location on a slender cone and the response of this to changes in the noise environment have been determined. Root-mean-square free-stream noise levels ranged from less than one-tenth up to values approaching those for conventional nozzles, with the lowest values prevailing at upstream locations within the nozzle. For low noise conditions, cone transition Reynolds numbers were in the range of those for free flight; whereas for high noise conditions, they were in the range of those in conventional tunnels.	11. Contract or Grant No.		
17. Key Words (Suggested by Author(s)) Supersonic wind tunnel Free-stream noise Transition Boundary layer	18. Distribution Statement Unclassified - Unlimited		
19. Security Classif. (of this report) Unclassified	20. Security Classif. (of this page) Unclassified	21. No. of Pages 68	22. Price A04
Subject Category 34			

National Aeronautics and
Space Administration

Washington, D.C.
20546

Official Business

Penalty for Private Use, \$300

THIRD-CLASS BULK RATE

Postage and Fees Paid
National Aeronautics and
Space Administration
NASA-451



4 110, 830909 S00903DS
DEPT OF THE AIR FORCE
AF WEAPONS LABORATORY
ATTN: TECHNICAL LIBRARY (SUL)
KIRTLAND AFB NM 87117

NASA

POSTMASTER: If Undeliverable (Section 158
Postal Manual) Do Not Return
